LEWIS ACIDIC BEHAVIOR OF ANTIMONY: APPLICATIONS IN CATALYSIS AND ANION BINDING

A Dissertation

by

DI YOU

Submitted to the Office of Graduate and Professional Studies of
Texas A&M University
in partial fulfillment of the requirements for the degree of

DOCTOR OF PHILOSOPHY

Chair of Committee,	François P. Gabbaï
Committee Members,	Michael B. Hall
	Hong-Cai Joe Zhou
	Xiaofeng Qian
Head of Department,	Simon W. North

December 2019

Major Subject: Chemistry

ABSTRACT

Over the past decade, the chemistry of σ-accepting or Z-type ligands based on main group elements has drawn renewed attention because of the realization that their interaction with a transition metal (M) could be used to control the reactivity of the metal center. In this dissertation, I will describe my efforts to modulate the reactivity of platinum complexes in which the Z-type ligand is an antimony unit and more specifically a halostiborane unit. The work described here shows that these complexes are prone to antimony-centered anion abstraction making the coordinated platinum center more oxidized and thus more electrophilic. Another strategy involves the use of weakly coordinating anion which, in the presence of a basic substrate, readily dissociate from the dinuclear core, resulting once again in an increased electrophilic character at the platinum center. These changes favorably impact the activity of the complexes as catalysts for enyne cycloisomerization reactions and hydroarylation reactions. The results obtained in these studies underscore the favorable role of these anion abstraction reactions which notably increase the carbophilic reactivity of the platinum center.

The strong Lewis acidity of antimony can also become an asset in the area of anion binding. Distiboranes designed to chelate small anions have shown advantageous anion chelating properties, including in protic media. To further improve these properties, this dissertation has explored the synthesis and properties of distiboranes based on the electron deficient perfluoro-*ortho*-phenylene backbone. Experimental and computational results indicate that perfluorination of the *ortho*-phenylene backbone affords fluoride anion chelators whose fluoride ion affinity exceeds that of its non-fluorinated analogues.

DEDICATION

This dissertation work is dedicated to my husband, Congzhi Zhu, who has been a constant source of support and encouragement during the challenges of graduate school and life. I am truly thankful for having you in my life. This work is also dedicated to my parents, Baoxian You and Shuying Deng, who have always loved me unconditionally and whose good examples have taught me to work hard for the things that I aspire to achieve.

ACKNOWLEDGEMENTS

First and foremost, I thank my advisor Professor François Gabbaï for guiding, encouraging, and supporting me through my entire graduate study. He taught me the way to be a professional researcher.

I would also like to thank Professors Michael B. Hall, Hong-Cai Zhou and Xiaofeng Qian who served on my committees, for providing important feedbacks and constructive criticism on my research projects. I am also grateful to all the staff in the Department of Chemistry and Material Characterization Facility at Texas A&M University for their kind support. Particularly, I am most grateful to Dr. Nattamai Bhuvanesh. His excellency in single crystal analysis is essential to my graduate research. I would also like to thank Dr. Lisa Perez in the Laboratory for Molecular Simulation at Texas A&M University for her help in the computational works.

I also thank and acknowledge the past and present group members in the Gabbaï group for being a constant source of encouragement. They are Dr. Kewei Huang, Dr. Boris Vabre, Dr. Daniel Tofan, Dr. Guillaume Bélanger-Chabot, Dr. Sumit Sahu, Dr. Rosmita Borthakur, Dr. Rajendra Kumar George, Dr. Lewis Wilkins, Dr. Kantapat Chansaenpak, Dr. Masato Hirai, Dr. Haifeng Yang, Dr. James (Stuart) Jones, Dr. Anna Marie Christianson, Ahmed Ali, Dr. Srobona Sen, Dr. Mengxi (Moncy) Yang, Dr. Chang-Hong(Eric) Chen, Elham Tabei, Dr. Ying-Hao (Russell) Lo, Mohammadjavad Karimi, Elishua Litle, Gyeong-Jin Park, Jesse Smith, and Benyu Zhou. These people always provide generous help and support when I am in need. Thanks also go to undergraduate students and visiting scholars. They

are Dr. Sikun Cheng, Dr. Min-Hyung Lee, Minji Kim, Dr. Mohamed R. Saber and You Jiang.

I would like to thank my parents Baoxian You and Shuying Deng, who supported my decisions no matter what. Last but not the least, my heartfelt thanks go to my husband Dr. Congzhi Zhu, who has been by my side for most of my PhD life. His unconditional love and support have been with me through ups and downs. His love and company are never to forgotten by me, and I look forward to spending the rest of my life with him.

NOMENCLATURE

AIM	Atom in Molecules
MeCN	Acetonitrile
DFT	Density Functional Theory
DMSO	Dimethylsulfoxide
FIA	Fluoride Ion Affinity
LUMO	Lowest Occupied Molecular Orbital
NBO	Natural Bond Analysis
NLMO	Natural Localized Molecular Orbital
NMR	Nuclear Magnetic Resonance
Ph	Phenyl
TBA	Tetrabutylammonium
TBAF	Tetrabutylammonium Fluoride
TBAT	Tetrabutylammonium Difluorotriphenylsilicate
THF	Tetrahydrofuran

TABLE OF CONTENTS

Page

LIST OF FIGURES

Page

LIST OF TABLES

Page

CHAPTER I

INTRODUCTION TO ANTIMONY: APPLICATIONS IN FLUORIDE BINDING AND CATALYSIS*

1.1 Lewis acidity of antimony compounds

1.1.1 Lewis acidity of antimony (III) compounds

A Lewis acid is defined as a chemical species that contains an empty orbital, which is capable of accepting an electron pair from a Lewis base. Prototypical Lewis acids are group 13 elements which contain an empty p orbital. For example, BF_3 forms Lewis adducts with a number of species. It is also known as an important reagent in organic synthesis where it can be used to catalyze Friedel-Crafts alkylation reactions[1,2], acylation reactions[2,3] and Diels-Alder reactions.[4] Its heavier congener, $AlCl_3$, is often used as a Lewis acid catalyst for Friedel-Crafts type reactions.[5] Moreover, by replacing the group 13-bound halides, the hydrolytic stability of the Lewis acids can be significantly increased as in the case of $B(C_6F_5)_3$ which has been used in the field of organic catalysis,[6-11] anion-sensing,[12-17] polymerizations,[18-21] and small molecule activations.[22-29]

While group 13 elements dominate the field of Lewis acid chemistry, heavier main-group elements such as those from the group 15 may also display elevated Lewis

*Reprinted with permission from "Tunable σ -Accepting, Z-Type Ligands for Organometallic Catalysis" You, D.; Gabbaï, F. P. *Trends. Chem.* **2019**, *1*, 485. Copyright 2019 Elsevier Inc.

acidity. This group, also known as the pnictogen group, comprises nitrogen, phosphorous, arsenic, antimony and bismuth. These elements carry five s/p valence electrons and are typically found in their III and V oxidation states. Among this group, nitrogen and phosphorus are nonmetals that are widely used as nucleophiles or Lewis bases in their III oxidation state because of the presence of lone pair electrons.[30] Going down the group the emergence of Lewis acidic properties reveal, even in the III oxidation state, at least when electron-withdrawing substituents are present. This is for example the case of the antimony derivatives **1** and **2** shown in Figure 1. In these compounds, the antimony (III) centers act as a Lewis acid and accept an electron pair from the nitrogen lone pair.[31,32] A more detailed study on the coordination chemistry of antimony (III) complexes has been conducted by the Reid group who studied complexes of type **3**.[33] This group found that the bonding between complexes of $SbMe_nBr_{3-n}$ and transition metal carbonyls varies significantly with different number of bromide substituents on the antimony. As the number of bromide group increases, the σ-donating ability of the Sb fragment decreases. This is accompanied by an increase in its π-accepting ability, indicating an increase in the Lewis acidity of the antimony fragment. These results demonstrate that when properly designed, antimony (III) centers can display Lewis acidic properties, the magnitude of which can be increased by installing electron withdrawing ligands. Based on these findings, recent efforts have explored the design of organoantimony (III) derivatives that are sufficiently Lewis acidic to bind halide anions. Examples of such compounds include **4** and **5**, both of which readily interact with chloride anions.[34,35]

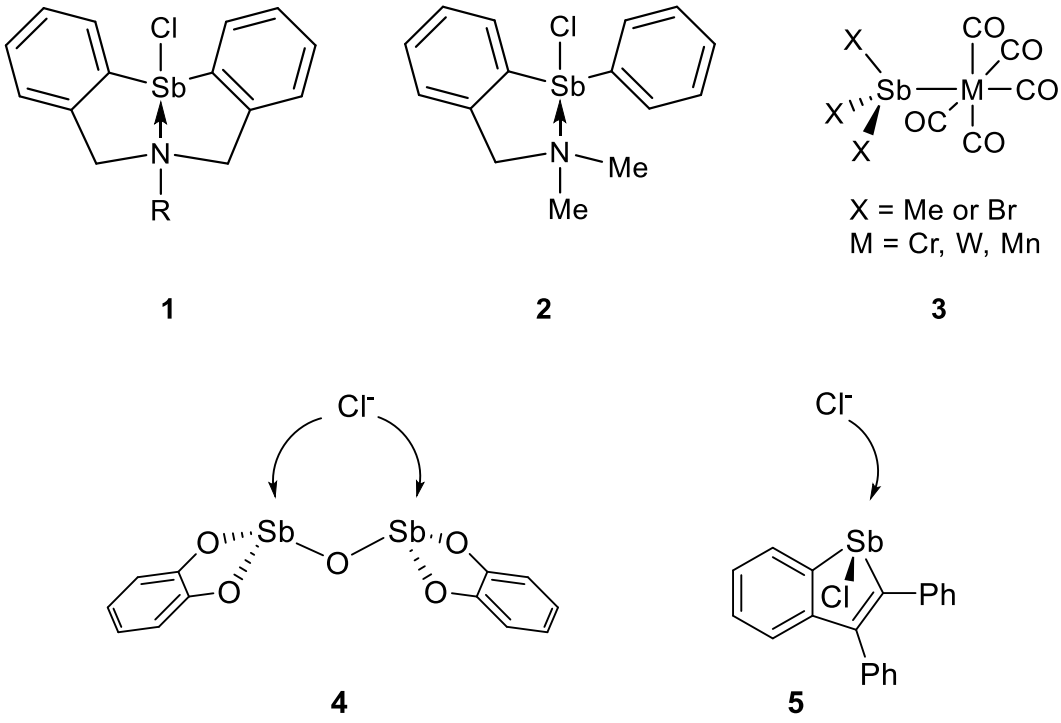

Figure 1. Lewis acidic antimony (III) containing species

1.1.2 Lewis acidity of antimony(V) compounds

Unlike antimony(III) which only displays Lewis acidity when substituted with electron withdrawing groups, antimony(V) compounds have long been known as some of the strongest Lewis acids.[36-39] SbF_5 is the major component of magic acid, FSO_3H-SbF_5, which was developed in the 1960's.[40] Sb(V) halides possess a higher Lewis acidity that the more commonly employed group 13 Lewis acid. This is supported by the computational work done by Krossing, who showed that the gas phase fluoride ion affinity (FIA) of SbF_5 exceeds that of BF_3 by around 150 kJ/mol.[41] The high Lewis acidity of Sb(V) has also been confirmed experimentally by Gutmann, who measured the binding

constant of a number of acids including $SnCl_4$, $AlCl_3$, BCl_3, PCl_5, $SbCl_5$ and $SbCl_3$ using tris(4–(dimethylamino)phenyl)methylium chloride.[42-44] He confirmed that, among these acids, $SbCl_5$ possesses the highest Lewis acidity.

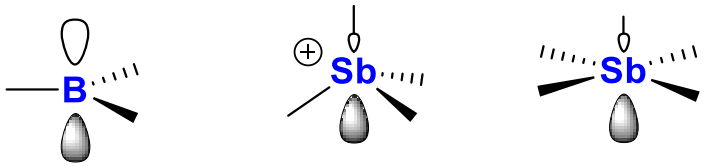

Figure 2. p orbital of B (left) and σ* orbitals of the Sb–X bond (right).

Unlike the more widely studied group 13 Lewis acids, whose Lewis acidity is known to derive from the presence of a vacant p orbital, the acidity of group 15 compounds is attributed to low-lying σ* orbitals of the central atom-ligand bonds as shown in Figure 2. Compared with group 13 elements, group 15 Lewis acids are intrinsically interesting to study due to their high Lewis acidity,[45-47] redox active properties,[48-52] and larger atomic size that can display rich coordination chemistry.[53-63] This atypical properties have stimulated a number of studies which are detailed in the next section and in which antimony (V) Lewis acids are used for anion complexation[64-68] and for organic reaction catalysis.[69-72]

1.1.3 Applications of antimony(V) in fluoride sensing and catalysis

In the past, our group has synthesized the stibonium derivative [**6**]$^+$, which incorporates a fluorescence reporter. This cation complexes fluoride ions in organic

solvents as well as in water to afford the corresponding fluorostiborane complex. This process is accompanied by a drastic fluorescence turn-on response, which can be used to report the fluoride binding event.[73] Similarly, the Gabbaï group has synthesized the neutral stiborane complex **7** that also complexes fluoride in the presence of water.[66] Both complexes [**6**]$^+$ and **7** can be used for fluoride sensing purposes as they show high fluoride binding affinities. More importantly, they exhibit a distinct increase in fluorescence intensity upon fluoride complexation.

To further increase the fluoride affinity of antimony-based Lewis acids, the Gabbaï group have developed bifunctional stiboranes **8** and **9** (Figure 3). Both of these complexes possess high fluoride anion affinities. For example, complex **8** readily binds fluoride between the two antimony centers via chelation in aqueous solution containing 95% of water.[65] Complex **9** shows an even higher fluoride affinity which was correlated to the structure of the 1,8–triptycenediyl backbone and the formation of a C–H···F hydrogen bond involving the triptycene bridgehead methine unit.[74] In addition, comparison of both bifunctional stiboranes with their monofunctional analogue $Ph_3Sb(O_2C_6Cl_4)$ shows that the bidentate distiborane is more acidic, indicating the importance of the bifunctionality. Altogether, these results document the high fluoridophilic properties of neutral Sb(V) species; they also show that the fluoride ion affinity can be effectively increased via chelation.

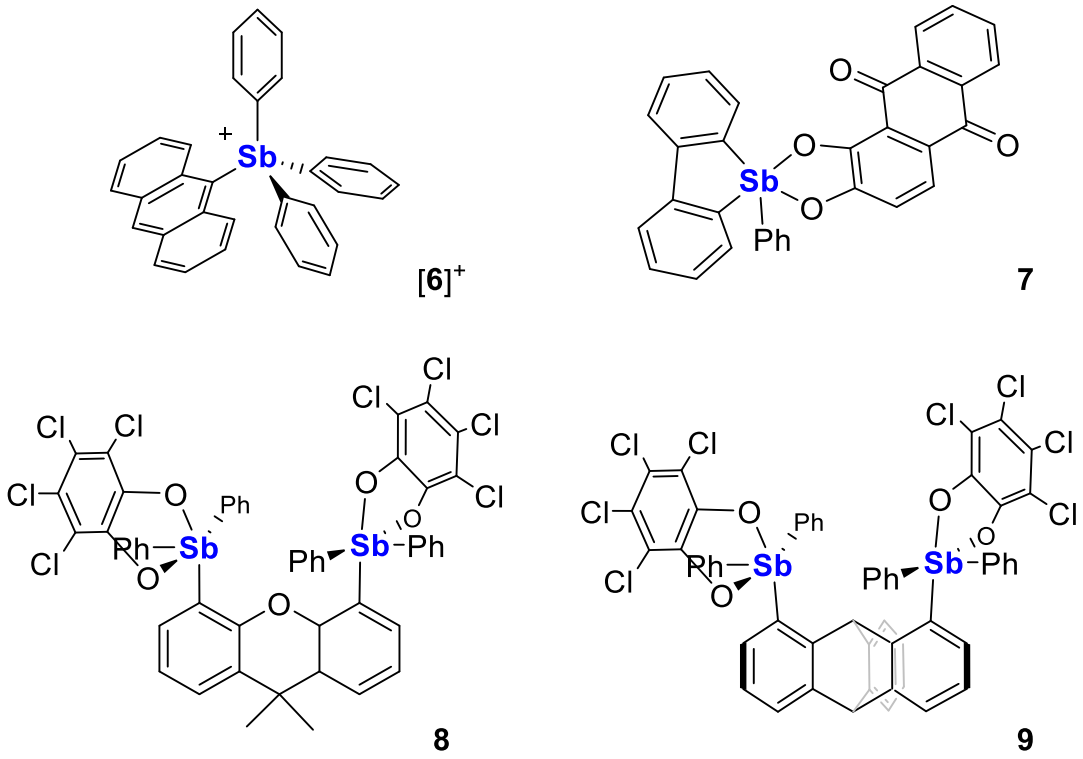

Figure 3. Monofunctional (top) and bifunctional (bottom) Sb(V) containing species.

Apart from exploring the fluoride binding properties of antimony Lewis acids, the Gabbaï group has also studied their role in the field of Lewis acidic catalysts.[69-71] The simple cationic complex $[Ph_3SbCl][SbCl_6]$ (**10**) can be synthesized by reaction of Ph_3SbCl_2 with $SbCl_5$ in CH_2Cl_2.[75] The high electrophilic character of the antimony center is reflected by the tendency of the stibonium cations to interact with the $[SbCl_6]^-$ anion via a long Sb–Cl bond of 3.231(6) Å. This complex is very active as a catalyst in the Friedel-Crafts dimerization of 1,1–diphenylethylene leading to conversion into 1–methyl–1, 3, 3–triphenyl–2, 3–dihydro–1H–indene in a 99% yield after 20 min (Figure 4). This reaction

is also catalyzed by electrophilic phosphoniums[76] and fluorosulfoxonium cations.[77] Yet, the use of a stibonium catalyst for this reaction has not been previously documented.

In addition, the Gabbaï group has also studied a number of stibonium cations of the general formula $[ArSbPh_3]^+$ with Ar = Ph (**11a**), naphthalene (**11b**), anthracene (**11c**), Mes (**11d**), *o*–(dimethylamino)phenyl (**11e**), and *o*–((dimethylamino)methyl)phenyl (**11f**) and compared their catalytic activity in the cycloaddition reaction of isocyanates and oxiranes (Figure 5). It was found that all stibonium cations catalyze the formation of 3,4–oxazolidinone products, although the reactivities of **11e** and **11f** are less pronounced due to the presence of ancillary amino donors which quench the Lewis acidity of the antimony centers.

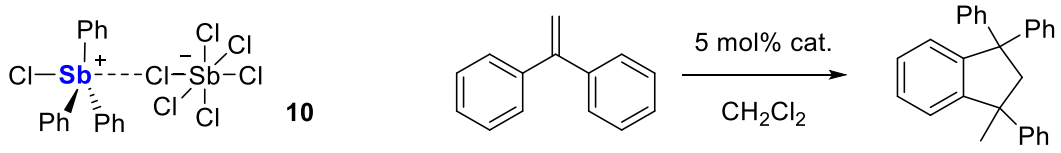

Figure 4. Dimerization of 1,1–diphenlyethylene catalyzed by $[Ph_3SbCl][SbCl_6]$.

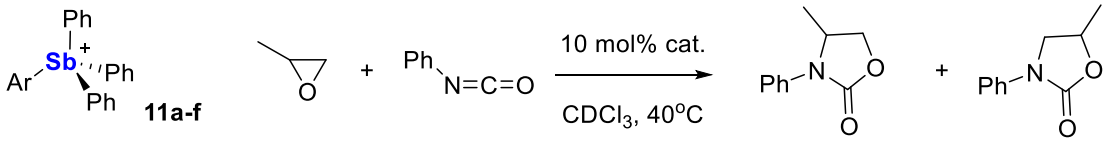

Figure 5. Cycloaddition of isocyanates and oxiranes catalyzed by $[ArSbPh_3]^+$.

.

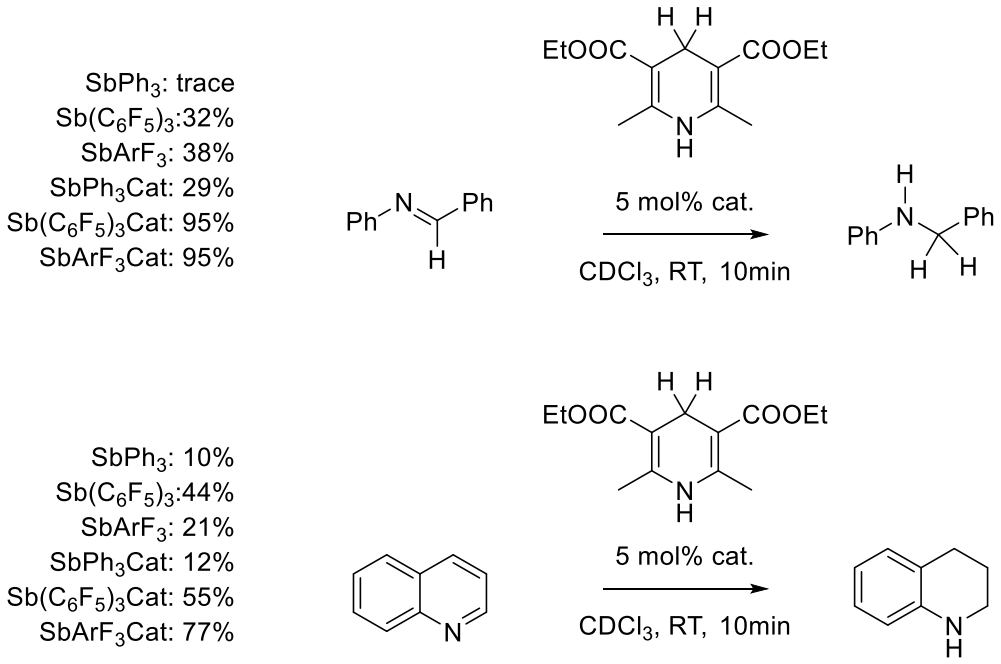

Figure 6. Transfer hydrogenation of N–benzylideneaniline and quinoline reactions.

A recent study by our group focused on comparing the Lewis acidic properties of $SbPh_3$ (**12a**), $Sb(C_6F_5)_3$ (**12b**), and $SbArF_3$ (ArF = 3,5–$(CF_3)_2C_6H_3$) (**12c**) with those in their oxidized forms $SbPh_3Cat$ (**12d**), $Sb(C_6F_5)_3Cat$ (**12e**), and $SbArF_3Cat$ (Cat = *o*–$O_2C_6Cl_4$) (**12f**).[70] While $SbPh_3$, $Sb(C_6F_5)_3$, and $SbArF_3$ do not interact with $Ph_3P{=}O$ in $CDCl_3$ to any measurable extent, their stiborane analogues $SbPh_3Cat$, $Sb(C_6F_5)_3Cat$, and $SbArF_3Cat$ readily interact with $Ph_3P{=}O$ in solution. Computational results show that the σ* orbital of $Sb(C_6F_5)_3Cat$ (-2.65 eV) is significantly lower in energy than that of $Sb(C_6F_5)_3$ (-1.76 eV), in line with the higher Lewis acidity of $Sb(C_6F_5)_3Cat$. The higher Lewis acidity of $Sb(C_6F_5)_3Cat$ and $SbArF_3Cat$ also comes to light when these compounds are used as catalysts for organic transformations. For transfer hydrogenation reactions of *N*–benzylideneaniline and quinoline, $Sb(C_6F_5)_3Cat$ and $SbArF_3Cat$ performed as the

best catalysts (Figure 6). The results show that the catalytic reactivity of organoantimony is notably enhanced when increasing the Lewis acidity of the antimony center.

1.2 Antimony as non-innocent Z-type ligands

1.2.1 Orbital diagram of the linearly coordinated metal complex and Z-type ligand

Controlling the reactivity of transition metal catalysts by secondary coordination sphere effects is an active area of investigation which has drawn considerable interest owing to the benefits it presents in the area of molecular catalysis.[78-84] Advancing this general area necessitates the elucidation of cooperative effects that may occur between the catalytic center, the reactants, and the surrounding environment. Such cooperative mechanisms, which usually involve non-covalent interactions, may serve to not only guide reacting molecules but also lower activation barriers which impede the catalytic reaction. Tailoring these cooperative effects necessitates the incorporation of specific functionalities positioned beyond the reactive metal center. Such functionalities can be Lewis basic, in which case it will serve to engage electrophilic reaction substrates.[85] They may also consist of hydrogen-bond donor groups which can help with the stabilization of anionic intermediates, such as those generated during a reduction reaction.[86-89] A less explored area of research concerns the use of Lewis acidic functionalities which, in principle, could serve in a capacity similar to those of hydrogen-bond donor groups.[90-92]

Lewis acidic functionalities, when positioned sufficiently close to the metal center, can sometimes enter its primary coordination sphere leading to a direct metal–Lewis acid interaction. In such instances, the Lewis acid behaves as a Z-type or σ-accepting ligand

and draws on the electron density of the metal center.[93-102] The formation of this interaction provides a handle whereby Z-type ligands can be used to effectively perturb and also control the electronic characteristics of the metal.[97,100,102] Such effects, which are becoming increasingly important in the context of catalysis[103-110], can be explained by considering the interaction between a σ-accepting orbital on the Z-type ligand and the metal centered orbitals. Through this interaction, the Z-type ligand draws electron density from a filled d-orbital while also stabilizing a metal-centered vacant p orbital (Figure 7). As a result of this stabilization, the Lewis acidity displayed by the late transition metal is notably increased.[111]

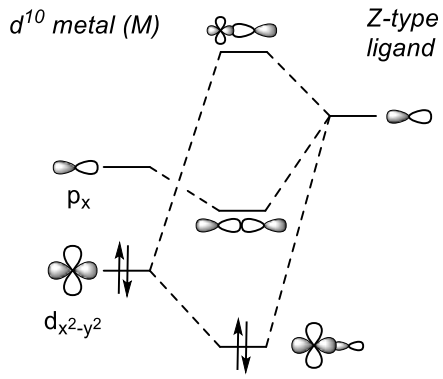

Figure 7. Molecular orbital diagram for the interaction of d^{10} metal with Z-type ligand.

It is shown in the recent work of Figueroa[111] that the d^{10} metal complexes stabilized by two isocyanide ligands $Pt(CNAr^{Dipp2})_2$ (**13**) could form unsupported metal–metal linkages with Ag(I), which is described as dative σ-interactions from Pt to Ag(I) (Figure 8). Such an interaction readily activates the group 10 metals towards the binding of Lewis

bases trans to the Ag acceptor; thus, illustration the ability of Z-type ligands to tune the electronic profiles of d^{10} transition metals from electron-rich and Lewis basic to electron-poor and Lewis acidic. A similar set of observations in the case of mercury–antimony complexes such as **14** featuring a Hg→Sb bond has been reported.[112] The more important lesson one can derive from these observations is that varying the strength of the M→Z interaction could in principle be used to precisely adjust the electrophilicity and thus the reactivity of the late transition metal center present in such complexes. This idea is an emerging paradigm in late transition metal chemistry and one that is gaining increasing validation. In the next sections, I will describe the possibility of precise control of the M→Z interaction by modification on the Z-type ligand. More importantly, I will focus on the unique opportunities offered by Z-type ligands for controlling the reactivity of the adjoining metal especially in the realm of organometallic catalysis.

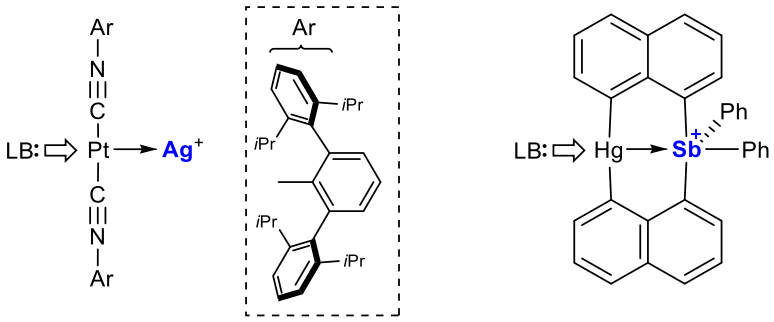

Figure 8. Example molecules containing M→Z interaction interaction.

1.2.2 Approaches to tune the M→Z interaction

Varying the nature of the main group element acting as the Z-type ligand

The study of periodic trends teaches us that the Lewis acidity of p-block elements

varies as the group is descended. Within the group 13, the computed stability of the water–EX_3 (EX_3 = group 13 trihalide) adducts indicate an irregular trend, with the aluminum and indium as the most Lewis acidic elements, followed by gallium and then boron.[113] When the accepting orbital of the Lewis acid is a σ* orbital, as in the case of tetravalent group 14 elements, a more progressive increase in Lewis acidity is observed.[114] It follows that the magnitude of an M→Z interaction could in principle be varied by simply changing the nature of the atom fulfilling the role of the Z-type ligand. Although conceptually straightforward, implementation of this idea can be complicated by anion migration induced by the high Lewis acidity of the main group element. Such a behavior is, for example, observed upon coordination of the trisphosphino-group 13 ligands[115-118] (B for **15**, Al for , Ga for , In for **18**) to gold(I) chloride (Figure 9). Indeed, rather than inducing a strengthening of the Au–E interaction (E = group 13 element), the more Lewis acidic group 13 elements in **16**AuCl–**18**AuCl engage with the chloride anion thus interfering with the projected intensification of the Au→E interaction.[119] Related group 14-based ligands of general formula $((Ph_2P)C_6H_4)_3EF$ (E = Si for **19**, Ge for **20**, Sn for **21**) provide a more reliable platform that resists anion migration as indicated by the structure of the corresponding gold chloride complexes **19**AuCl–**21**AuCl. Despite the larger size of tin, the Au–E bond is shorter in **21**AuCl (Au–Sn = 2.9686(3) Å) than in **20**AuCl (Au–Ge = 3.148(1) Å) and **19**AuCl (Au–Si = 3.223(2) Å). Expressing these metrical parameter as covalent ratios[120,121] (Si–Au:1.30; Ge–Au:1.23; Sn–Au:1.08) indicates that the more acidic tin atom exerts a stronger attractive force on the gold atom and its electron density

(Figure 9). These effects are supported by Natural Bond Orbital (NBO) calculations which also predict a strengthening of the Au→E interaction as the group is descended.

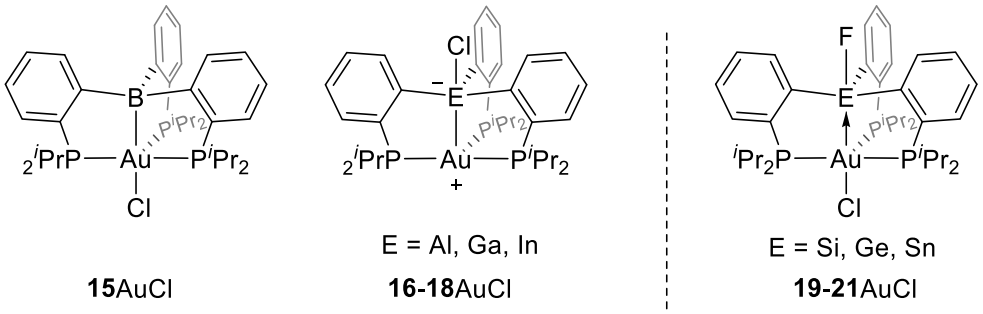

Figure 9. Group 13 and 14 elements as Z-type ligands.

The results obtained from ligands **15**-**18** show that identifying a platform in which the strength of the M→Z interaction can be adjusted predictably is non-trivial. Complexes based on 'double-decker' ligands (**22**$^{M/E}$ and **23**^{E}, E = group 13 element) provide a more recent and possibly more practical incarnation of this possibility whereby a group 13 element can be pre-introduced at the lower deck, followed by coordination of a transition metal ion (M) at the upper deck (Figure 10).[104,105,122] This approach is characterized by a high level of structural fidelity, with the only change being that of the group 13 element. The study of the Ni(0) (**22**$^{Ni/E}$) and Co(-1) (**22**$^{Co/E}$) complexes show that the M→E interaction increases in the order Al < Ga < In (Figure 10). For both families of complexes, this conclusion is corroborated by the stability of the corresponding H_2 complexes which indicates that H_2→M and M→E interactions mutually enhance each other. For the nickel complexes, additional evidence for the strengthening of the M→E interaction can be

derived from the Ni (0/1) redox couple which undergoes a significant anodic shift as the group 13 element becomes heavier, with structural analyses cementing this conclusion. The covalent ratio calculated for complexes **22**$^{Ni/E}$ and **22**$^{Co/E}$ markedly decreases as the size of the group 13 element increases. A related trend can be established for complexes of type **23**^{E} based on an examination of the covalent ratios which also decrease in the order Al < Ga < In (Figure). Interestingly, the Pd–Cl bond length is the shortest in **23**^{In}. In the extreme of the dative formalism, this shortening speaks to the strength of the Pd→In bond in **23**^{In} and its stabilizing impact on the Cl^{-}→Pd bond.

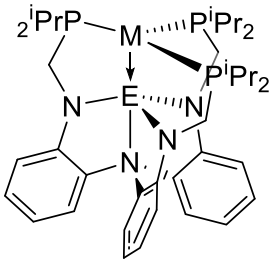

E = Al, Ga, In

22$^{M/E}$: M = Ni, Co^{-}

covalent ratios

	Co^{-}	Ni
Al	1.00	1.00
Ga	0.96	0.97
In	0.92	0.92

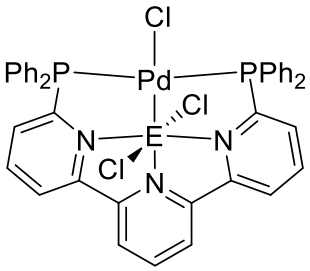

E = Al, Ga, In

23^{E}

covalent ratios

	Pd	Pd-Cl (Å)
Al	0.96	2.55
Ga	0.93	2.46
In	0.89	2.43

Figure 10. Modulation of the M→Z interaction by changing the group 13 Lewis acid.

It is interesting to note that the trend observed in the strength of the M→E bonds in **22**$^{M/E}$ and **23**$^{M/E}$ does not follow that suggested by the stability of classical Lewis adducts.[113] Indeed, calculations carried out for the conversion of EX_3 into adducts of general formula LB→EX_3 (LB = Lewis base) indicate that Lewis acidity increases in the following order Ga < In < Al for hard Lewis bases and Ga<Al < In for soft Lewis bases.[123] The fact that the M→E bond strength decreases in the order Al < Ga < In in compounds of type **22**$^{M/E}$ indicates that other factors must be at play.

Varying the nature of the substituents bound the main group element acting as the Z-type ligand

The magnitude of an M→Z interaction could, in principle, be adjusted by simple variation of the substituent bound to the atom acting as the Z-type ligand. This approach needs to be applied with some nuance for main group elements which become hypervalent upon formation of the M→Z interaction. Indeed, since the formation of the M→Z interaction involves donation of a metal-based lone pair into a σ* orbital centered on the main group element, the nature of the ligand positioned trans from the metal atom will play a defining influence as illustrated in Figure 11.

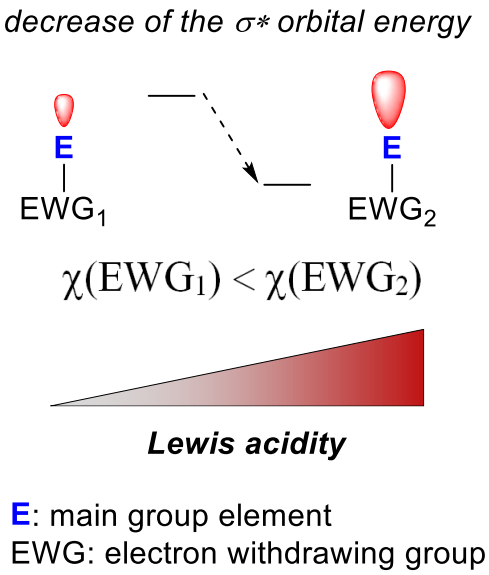

Figure 11. Diagram showing how the Lewis acidity of a main group element is affected by the electron-withdrawing properties of the substituent trans from the coordination site.

The above-mentioned effects are manifested in the chemistry of complex **24**, which is proposed to isomerize into **24'** when in solution.[124] In **24**, the silicon-bound unit trans from the metal is an electron withdrawing fluorine ligand, a situation predicted to lower the energy of the accepting σ* orbital while also increasing the contribution from the silicon atom. In **24'**, the phenyl group occupies the trans position. Given the lower electronegativity of phenyl *vs.* fluorine, the accepting σ* orbital raises in energy while also becoming less developed on the silicon atom. The anticipated consequence is a weakening of the Au→Si interatcion in **24'**. Accordingly, DFT calculations of these two isomers show a significant lengthening of the Au–Si distance from 3.13 Å in **24** to 3.45 Å in **24'**.

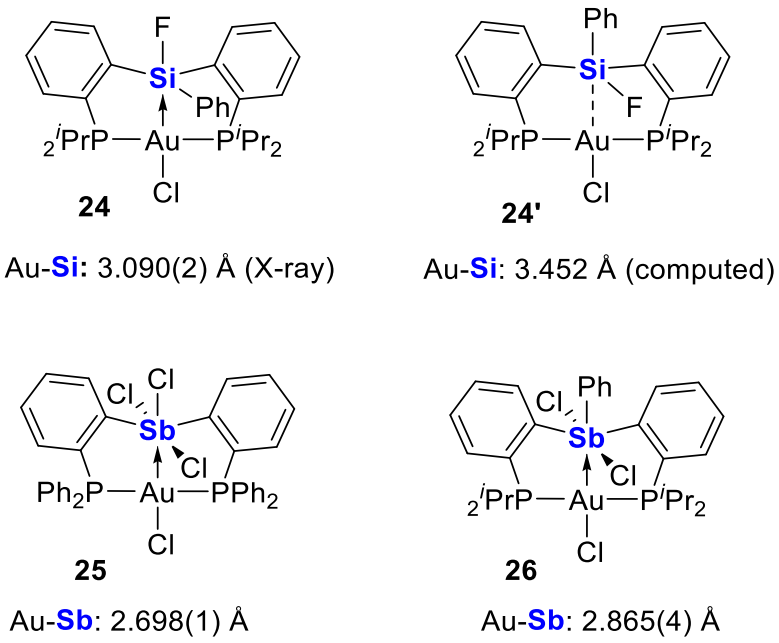

Figure 12. Modulation of the M→Z interaction by varying the substituents**.**

Definitive structural evidence for these substituent effects have been obtained for the antimony complexes **25** and **26**.[125,126] The Au–Sb separation increases from 2.698(1) Å in **25** to 2.865(1) Å in **26**, as a consequence of the lower electron-withdrawing properties of the phenyl group when compared to chlorine (Figure 12). Conceptually, these changes can also be assigned to the perturbation in the energy and spatial distribution of the σ* orbital resulting from this Ph/Cl ligand permutation.

The substituent effects described above can also be manifested in complexes featuring M→Pn interaction (Pn = pnictogen or group 15 element) in which the Pn element is in the trivalent state. Such effects have been established not only for antimony[125,127] but also bismuth-based complexes,[128,129] such as **27**^{X} (Figure 13).[130] In this family of

bismuth–platinum compounds, the nature of the X substituent has a marked influence on the length of the Pt→Bi interaction. Consistent with the prediction that an electron-withdrawing substituent will enhance the Lewis acidity of the bismuth center trans from the Bi–X bond, the Pt→Bi bond length increases in the order of **27**^{Me} < **27**^{C6F5} < **27**^{Cl} < **27**^{OTf}. These results also serve as a reminder that Pn elements in the +3 state can display notable Lewis acidity, especially in the presence of electron withdrawing substituents.[71,131]

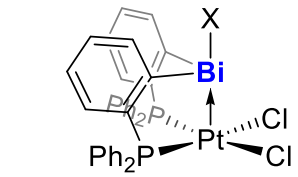

27^{X}, X = Me, C_6F_5, Cl, OTf

X	Bi-Pt
Me	3.062
C_6F_5	3.053
Cl	2.901
OTf	2.781

Figure 13. Modulation of the M→Z interaction by changing the substituents on the Lewis acid.

A last situation that illustrates substituent effects without involving hypervalence is provided by a comparison of complexes **28** and **29** which both feature an Au→B interaction (Figure 14).[132] Swapping the bis(*cyclo*-hexyl)boryl moiety of **28** with a borafluorenyl moiety in **29** leads to an enhanced Au→B interaction, reflected by a significant shortening from 2.90 Å in **28** in to 2.66 Å in **29**. This change is accompanied by a notable decrease of the natural charge for the boryl unit from 0.29 to 0.14, which supports the transfer of electron density to the boron center. NBO calculations reveal that the second-order perturbation energy for the Au→B interaction is also higher in **29** (16.8 kcal/mol) than in **28** (12.8 kcal/mol). The differences existing between **28** and **29** provide

another illustration of the role played by the main group substituent and in which the boron center Lewis acidity is enhanced by antiaromatic and ring-strain effects.[133]

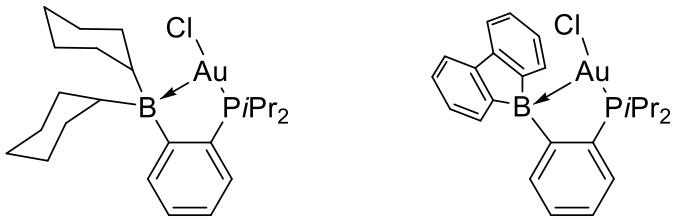

Figure 14. Modulation of the M→Z interaction by changing the substituents on the Lewis acid.

Varying the redox state of the main group elements acting as the Z-type ligand

The Lewis acidity of main group elements shows an important correlation with their redox state. Taking the pnictogen elements as an example, the pentahalides are notably more Lewis acidic than the corresponding trihalides.[64] This increase can be correlated to an oxidation-induced lowering of the energy of the σ* orbital as illustrated in Figure 15.[71]

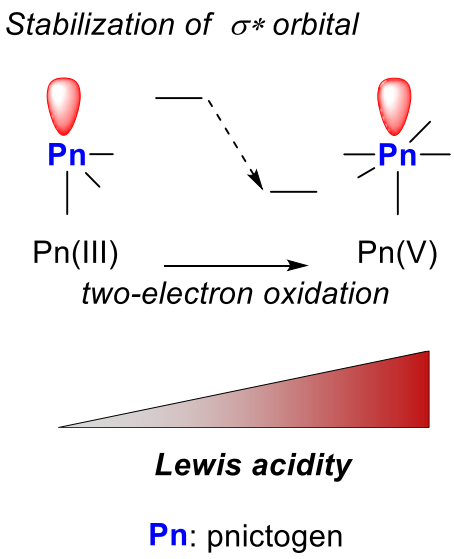

Figure 15. Diagram showing how the Lewis acidity of a main group element is affected by oxidation.

These σ* orbital energy changes can also be used to convert Lewis basic stibines into Lewis acidic stiboranes as illustrated by the response of complex **30** to oxidation.[134] Indeed, oxidation of this complex at antimony using $PhICl_2$ triggers an umpolung of the Sb–Au bond from Sb→Au in **30** to Au→Sb in **31** (Figure 16). The dinuclear core of the structure shows a clear response to oxidation of the antimony center. In particular, the Au–Sb distance of 2.709(1) Å in **31** is shorter than that measured for the reduced complexes (2.837(1) Å in **30**). Changes are also observed in the coordination geometry of the gold center, which shifts from distorted trigonal pyramidal in **30** to square planar in **31**. These changes, in particular the square planar geometry of the gold atom, indicate that the latter is affected by oxidation as it transitions from a monovalent form in **30** to a trivalent form in **31**. NBO analysis of **31** confirms this view and shows that the gold d_{x2-y2} orbital acts as a donor toward a σ*(Sb–Cl) orbital (Figure 16).

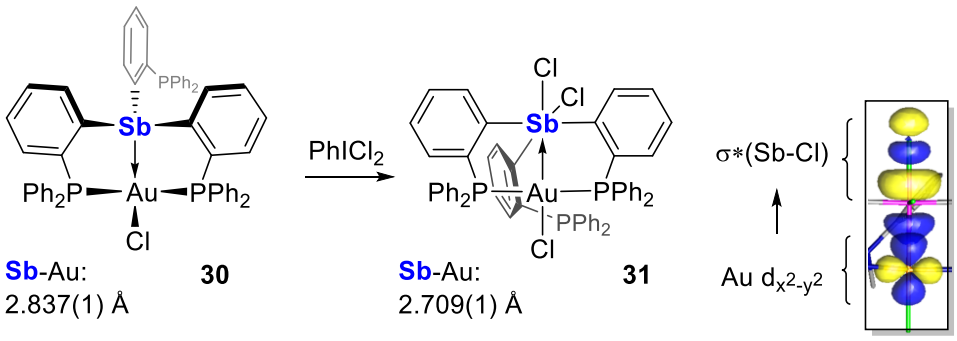

Figure 16. Oxidation impacts the magnitude of the M→Z interaction.

The chemistry of the chlorostibine–gold complex **32** provides another noteworthy manifestation of this effect (Figure 17). The Au→Sb donor-acceptor bond in **32** shortens by ~0.15 Å in **25**. NBO analysis offers a supporting picture, with the strength of the Au→Sb donor-acceptor interaction increasing from 70.8 kcal/mol in **32** to 148.5 kcal/mol in **25**. We will note in passing that examples exist where the reduction of group 13-based Z-type ligands can interfere and weaken the M→group 13 interaction,[135] provided that the group 13 element is the primary site of reduction.[136,137]

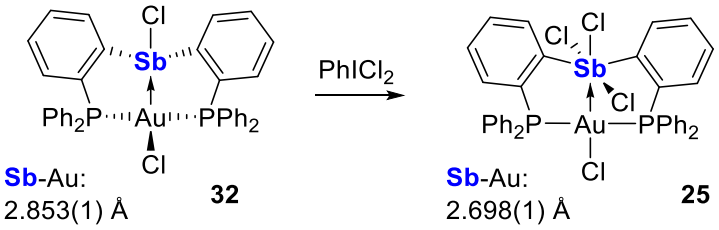

Figure 17. Modulation of the e M→Z interaction via redox chemisty.

Varying the coordination environment of the main group element acting as the Z-type ligand

We[138-142] and others[33,143-146] have demonstrated that stibine ligands are susceptible to the addition of anions when bound to a metal. This process, which can occur without dissociation of the antimony ligand from the metal center, reflects the coordination non-innocence of antimony ligands and their ability to adopt hypervalent electronic configurations.[100] Furthermore, the variable coordination environment of the antimony center directly impacts the electron deficiency of the metal, thus providing another strategy for modulating the properties of such Z-type ligands. As illustrated in Figure 18, conversion of a dihalostiborane into the corresponding mono and dication by halide anion abstraction is expected to greatly stabilize the antimony-based LUMO, leading to an increase in Lewis acidity. This effect is illustrated by a comparison of **33**, [**34**]$^{+}$ and [**35**]$^{2+}$, with [**35**]$^{2+}$ possessing the strongest and shortest Pt–Sb bond (Figure 18).

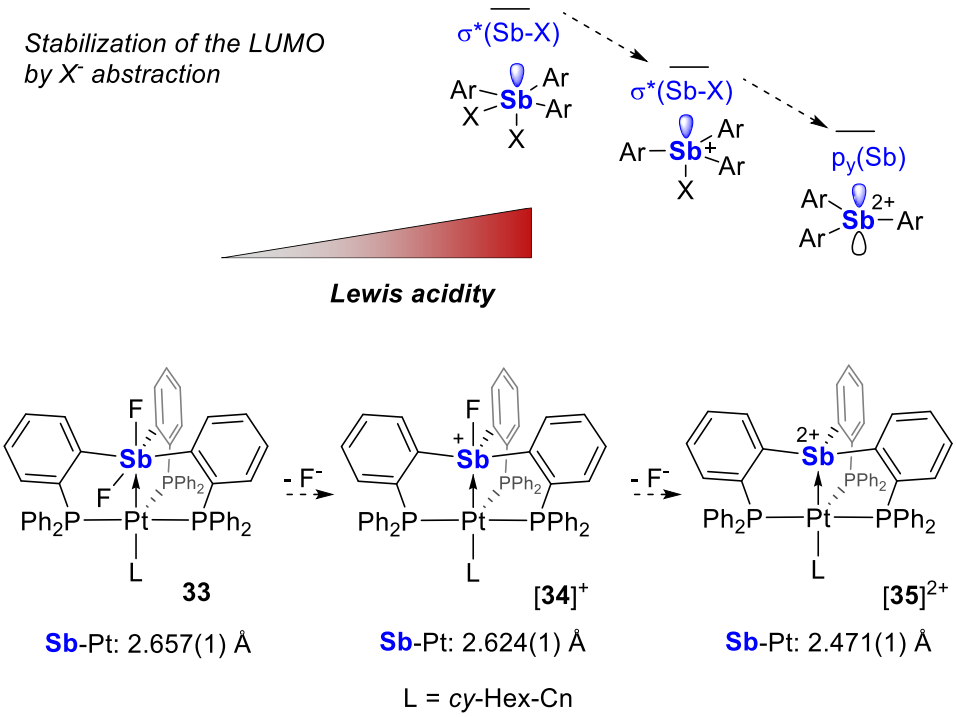

Figure 18. (Top) Illustration showing how anion abstraction from a main group element can be used to enhance its Lewis acidity. (Bottom) Structure of complexes and relevant metrical parameters showing how anion removal from the main group element impacts the magnitude of the M→Z interaction.

1.2.3 Using the M→Z interaction as a handle for controlling catalysis

As detailed above, several strategies have been developed for adjusting the strength of M→Z interactions. Given the donor-acceptor nature of this interaction, these strategies should provide control over the electrophilicity and thus the reactivity of the transition metal center present in these complexes. The series of recent results discussed in the following paragraphs validates this emerging paradigm. While a growing list of catalysts incorporating Z-type ligands exist,[102,108,109,147,148] I will limit the discussion to cases that speak to the importance of the M→Z interaction and its tunable nature.

Lewis acid-controlled catalysis

The double decker architecture present in complexes of type **22**$^{M/E}$ (Figure 10) provides control over the transition metal environment and its electron richness via variation of the group 13 element installed at the lower deck. Along this line, the Lu group has correlated the magnitude of the M→E interaction with the catalytic activity of the complexes. A systematic survey of compounds **22**$^{Ni/Al}$, **22**$^{Ni/Ga}$, and **22**$^{Ni/In}$ reveals some distinctive features.[104] Out of these three, only **22**$^{Ni/Ga}$ and **22**$^{Ni/In}$ are catalytically active in the hydrogenation of olefins leading to the proposal that a strong M→E interaction is needed for catalysis (Figure 19). They also observed a direct correlation between the strength of the Ni→E interactions and the ability of the nickel center to bind H_2 and N_2, with the strongest binding occurring with the indium complex. A more contrasted picture emerges from a comparison of the catalytic properties, with **22**$^{Ni/Ga}$ displaying a higher activity in the hydrogenation of styrene than **22**$^{Ni/In}$. Complex **22**$^{Ni/In}$ also promotes the hydrogenation of 1–octene, 1–hexene and cis–cylco–octene but again the reaction rate is significantly lower than that of **22**$^{Ni/Ga}$. The activity of the former is likely affected by the fact that the electron richness of the Ni(0) is depleted by the strong Ni→In interaction impeding the oxidative cleavage of the H_2 molecule prior to migratory insertion of the alkene.[149] Another factor to consider is the need of phosphine dissociation followed by alkene coordination. While dissociation may be more facile in **22**$^{Ni/In}$, the affinity for the olefin may be accordingly decreased.

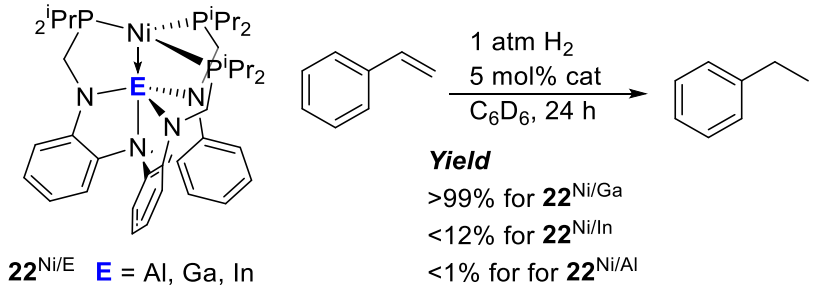

Figure 19. Styrene hydrogenation catalyzed by $\mathbf{22}^{Ni/E}$.

The notion that a strong M→E interaction does not correlate proportionally with catalytic activity also emerges in the work of Takaya and Iwasawa[122] who investigated complexes $\mathbf{23}^{E}$ as catalyst for the hydrosilylation of CO_2 (Figure 20). Indeed, the aluminum complex $\mathbf{23}^{Al}$, which appears to possess a weaker Pd→E interaction than $\mathbf{23}^{Ga}$ and $\mathbf{23}^{In}$, is by far the most active with a turnover frequency (TOF) of 19300 h^{-1}. Related results by Tauchert and co-workers on complexes of type $[\mathbf{36}^{E}]^{n+}$ (E = Li, n = 1; Cu, n = 2; Zn, n = 2) as CO_2 hydrosilylation catalysts further illustrate this point. In this case, the highest activity is observed for $[\mathbf{36}^{Zn}]^{2+}$ which is proposed to possess the strongest Pd→E based on crystallographic and computational data.[150] The greater accepting properties of the zinc metalloligand in this system is corroborated by a study of related rhodium(I) carbonyl complexes which also display an intense Rh→Zn interaction.[151] These fascinating results underscore the benefits that a precisely adjustable M→Z interaction presents in the context of catalysis although the activities of complexes $\mathbf{23}^{E}$ and $[\mathbf{36}^{E}]^{n+}$ do show a consistent picture regarding the role played by the magnitude of the M→E interaction.

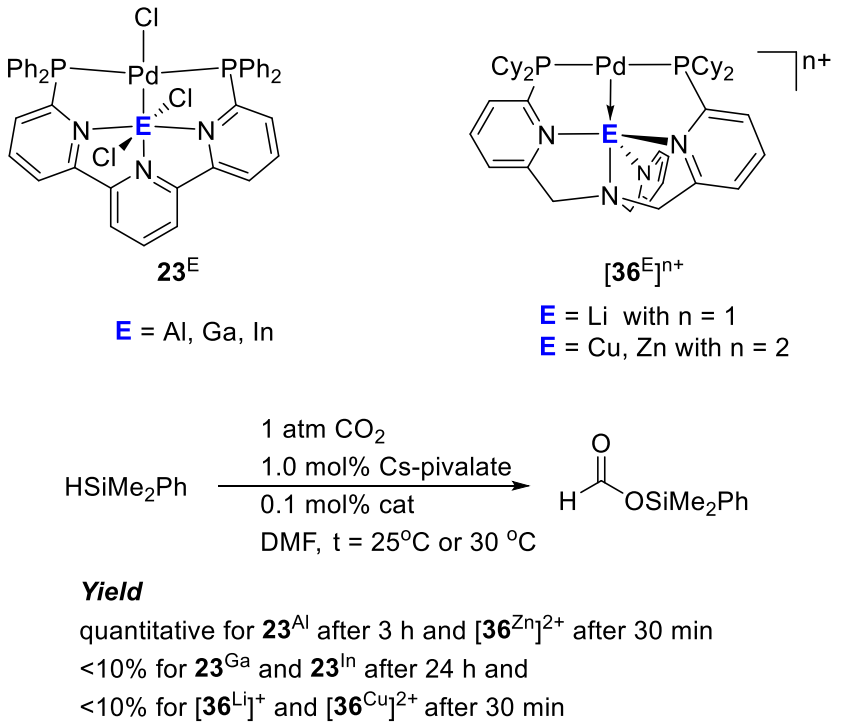

Figure 20. CO_2 hydrosilylation reactions catalyzed by $\mathbf{23}^{E}$ and $[\mathbf{36}^{E}]^{n+}$.

This strategy has also achieved some success with the use of bis(phosphino)phenylborane ligand in complex $\mathbf{37}^{H}$ to increase the reactivity of cationic gold by σ-inductive effects (Figure 21).[152] A continuum study to tune the electrophilic character of the neighboring gold center was carried out further by substitution of the phenyl ring on the boron center to more electron-withdrawing groups such as *p*-fluorophenyl in $\mathbf{37}^{F}$ or *p*-chlorophenyl in $\mathbf{37}^{Cl}$.[153] The Au–B distances in these complexes show very little differences. However, as the electron-withdrawing properties of the boron phenyl substituent increase (σ_p: H[0] < F[0.06] < Cl[0.22]), a decrease in the C1–Au distance is observed ($\mathbf{37}^{H}$: 3.041(3) Å; $\mathbf{37}^{F}$: 3.016(4) Å; $\mathbf{37}^{Cl}$: 2.983(3) Å). This contraction is accompanied with a decrease in the C1–Au–B angle ($\mathbf{37}^{H}$: 99.31(3)°; $\mathbf{37}^{F}$: 98.39(3)°;

37^{Cl}: 97.14(14)°), which indicated a direct interaction between the gold atom and the C1 carbon atom. **37**^{F} shows significant increase in reactivity than **37**^{H} towards the cyclization of yne–diols. On the other hand, **37**^{Cl} exhibits only a slight increase in reactivity compared with **37**^{H}.

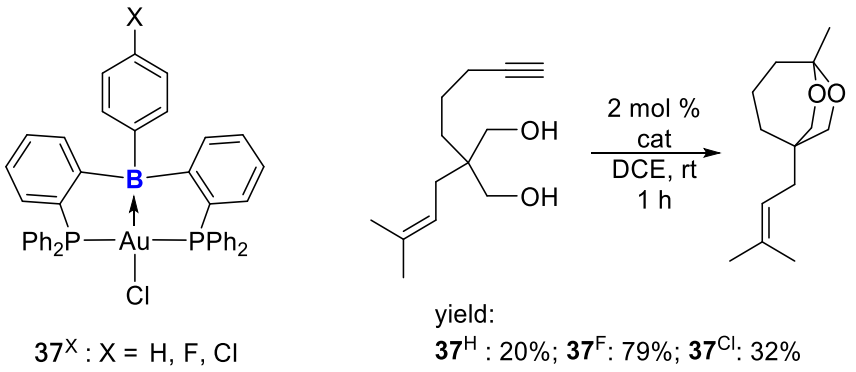

Figure 21. Substituent effects in the M–Z interaction in the cyclization of yne–diols.

Redox-controlled catalysis

Inagaki and coworkers have recently investigated cationic complexes of type [**38**]$^{+}$ for the carbophilic activation of alkynes (Figure 22).[152-154] This team found that these complexes are much more efficient catalysts for enyne cyclizations than simple model cations such as $[Ph_3PAuPPh_3]^{+}$, supporting the notion the enhanced catalytic activity of [**38**]$^{+}$ results from the strong σ-accepting properties of the Lewis acidic boron atom trans from the catalytically active site.

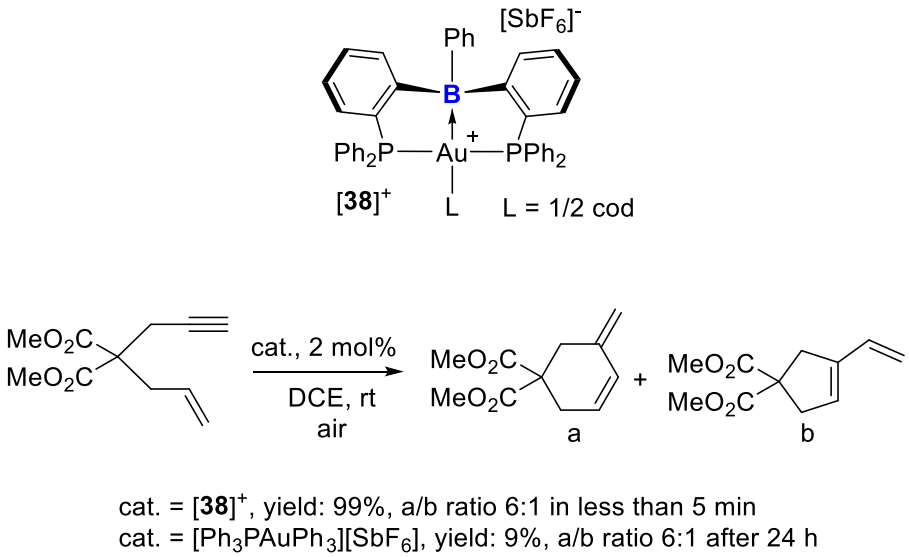

Figure 22. Catalytic activity of [**38**]$^{+}$ in an enyne cyclization reaction underscoring the role of the Au→B interaction

It occurred to us that substitution of boron by antimony in such species may afford complexes whose catalytic properties are controlled by the redox state of the antimony Z-ligand. This possibility has been tested by first investigating the properties of [**39**]$^{+}$, a cationic complex derived from **32** (Figure 23).[74,125] When used as a catalyst for the hydroamination of phenylacetylene with *p*–toluidine, [**39**]$^{+}$ showed sluggish activity. Based on the realization that the σ-accepting properties of the antimony center could be enhanced by oxidation as illustrated in Figure 15, we targeted the pentavalent antimony complex [**40**]$^{+}$, which could also be derived from **32**. Both structural and computational results suggest that [**40**]$^{+}$ possesses a stronger Au→Sb interaction than [**39**]$^{+}$. This stronger interaction translates into a more electrophilic gold center, as evidenced by its ability to readily bind Lewis bases such as water at the coordination site trans from antimony. More importantly, the increased Lewis acidity of the gold center in [**40**]$^{+}$ is also reflected in its

enhanced catalytic activity. Under the same conditions as those used for [**39**]$^{+}$, [**40**]$^{+}$ catalyzes the hydroamination of phenylacetylene with *p*–toluidine, achieving greater than 95% conversion after one hour. This reactivity enhancement validates the concept that the redox state of non-innocent Z-ligands may be used to control the catalytic activity of the adjoining metal center. While we showed that various amines and alkynes can be used in these reactions, no hydroamination product was observed when aliphatic amines where employed. In fact, the use of such amines appeared to induce reduction of the antimony center.

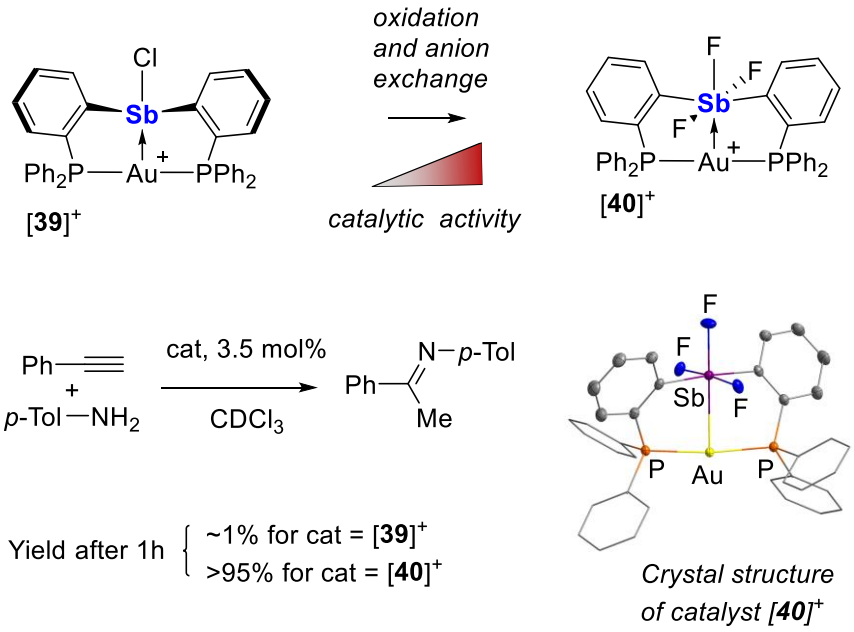

Figure 23. Example showing how oxidation of the main group element acting as a Z-ligand enhances the catalytic activity of the adjacent transition metal center.

1.3 Objectives

As explained in the preceding sections, Z-type, Lewis acidic ligands can be used to precisely tune the electron density of a metal by establishing an the M→Z interaction. Tuning can be achieved by changing the nature of the Lewis acid, by switching the substituents on the Lewis acids, or by taking advantage of the redox active properties of heavier main group Lewis acids. In most cases, the M→Z interaction is associated with the Lewis acidity of the Z-type ligand. With increasing Lewis acidity at the Z-type ligand, an enhanced M→Z interaction is observed. This provides a handle on the electron density of the transition metal center and thus over its catalytic properties. To further advance this research field, we have become interested in exploiting the coordination non-innocence properties of antimony in order to tune the reactivity of as coordinated transition metal. The objective of this dissertation is to test this idea by investigating the formation of cationic platinum-antimony species by abstraction of anionic ligands bound to antimony. A second objective is to access related complexes by incorporation of weakly coordinating anions at antimony, with the expectation that these anions would dissociate to generate reactive cationic complexes. Finally, a last aspect of this work has been the development of bidentate antimony based Lewis acids for anion chelation.

CHAPTER II

MODULATING THE σ-ACCEPTING PROPERTIES OF AN ANTIMONY Z-TYPE LIGAND VIA ANION ABSTRACTION: REMOTE-CONTROLLED REACTIVITY OF THE COORDINATED PLATINUM ATOM*

2.1 Introduction

The interaction of Z-type ligands with late transition metal complexes is emerging as a new paradigm for controlling the electronic characteristics, and thus reactivity of transition metals.[93-102] This approach, which is meeting increasing validation in the realm of catalysis,[103-110] can be traced back to the σ-accepting properties of Z-type ligands which can effectively stabilize a vacant p-orbital of the late transition metal center while also drawing density from the filled d-orbitals (Figure 24). These effects, first formulated by Alvarez for d^8 metal complexes,[155] have been recently invoked in the case of d^{10} metal complexes to explain the enhanced Lewis acidity of the coordination site directly *trans* from the Z-type ligand.[111,112,156] The same effects are manifested in the chemistry of linearly coordinated bis-phosphine gold(I) complexes which can be rendered catalytically

*Reprinted with permission from "Modulating the σ-Accepting Properties of an Antimony Z-type Ligand via Anion Abstraction: Remote-Controlled Reactivity of the Coordinated Platinum Atom" You, D.; Yang, H.; Sen, S.; Gabbaï, F. P. *J. Am. Chem. Soc.* **2018**, *140*, 9644. Copyright 2018 American Chemical Society

active via coordination of a Z-type ligand along a direction perpendicular to the P–Au–P vector.[152,153]

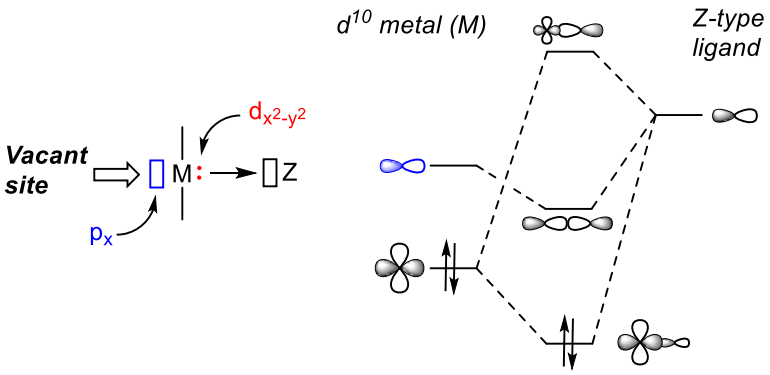

Figure 24. Idealized orbital interaction diagram for a linearly coordinated d^{10} metal complex and a Z-type ligand.

The orbital interaction diagram shown in Figure 24 suggests that the reactivity of the transition metal could be precisely adjusted by varying the strength of the M→Z interaction. Such a possibility is illustrated by the contributions of Lu,[104,105] Takaya and Iwasawa[122] who showed that the nature of the group 13 element installed at the lower deck of heterobimetallic complexes of **22**$^{M/E}$ and **23**^{E} modulates the electron richness of the neighboring transition metal center and controls its reactivity including during catalysis[104,105,122] (Figure 19, Figure 20). As part of our contribution to this research topic, we have shown that the magnitude of the M→Z interaction can also be adjusted by changing the oxidation state of the Lewis acidic element. For example, oxidation of the antimony center in complexes of type [**39**]$^{+}$ to the pentavalent state in type for [**40**]$^{+}$ strengthens the magnitude of the Au–Sb interaction, making the gold center competent for the activation of alkynyl substrates (Figure 23).[125,157] These results highlight the unique

opportunities offered by redox non-innocent Z-ligands for controlling the reactivity of an adjacent metal.

We, and others, have also showcased how antimony-based Z-type ligands display coordination non-innocence and can readily engage in the coordination of anionic ligands, without dissociation from the metal center.[33,100,138,139,142,143,158] Our work on this topic has also explored how these anion coordination events at antimony affect the electronic properties of the adjacent metal center. In the case of [**41**]$^{2+}$ and **42**, we showed that coordination of anionic fluoride ligands to antimony reduces the Lewis acidity of antimony while also inducing a shift of the Sb–Pt bonding electron pair toward platinum (Figure 25, left).[144] It occurred to us that such effects could be exploited to tune the magnitude of M→Z interaction, thus offering precise control over the accumulation of electron density of the platinum center (Figure 25, right). In this chapter I will provide a series of results which show that such processes, taken in reverse, form the basis of a new strategy to increase the electrophilic character of the platinum center and render it catalytically active.

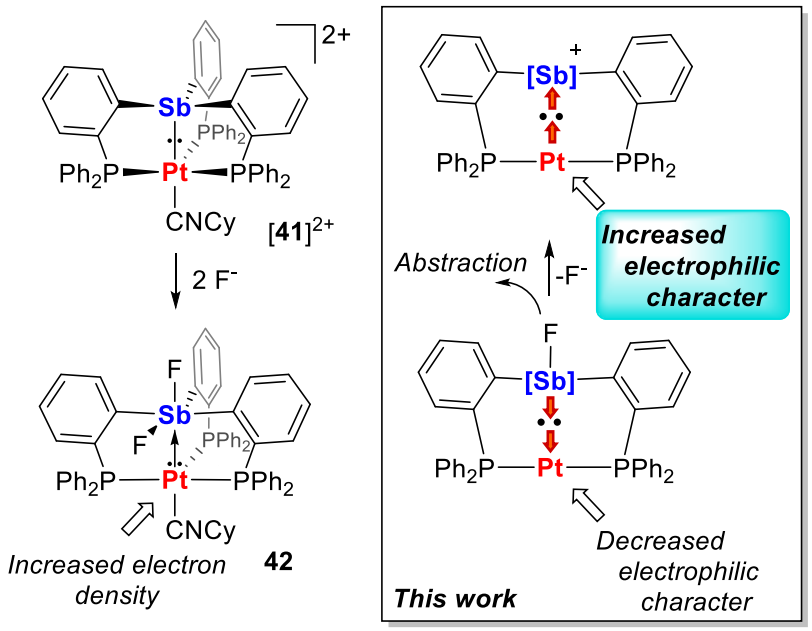

Figure 25. Modulation of the electrophilic character of platinum in dinuclear Sb–Pt complexes by an anion coordination /decoordination events at antimony.

2.2 Previous results

A former student in the Gabbaï group, Haifeng Yang, treated the dichlorostiboranyl platinum complex **43**[159] with three equiv of thallium fluoride (TlF) in the presence of a donor ligand L (L = acetonitrile or cyclohexyl isocyanide) and obtained **44** and **45** (Figure 26). This student found that the ^{31}P NMR spectra of complexes **44** and **45** feature a resonance at 71.8 and 75.9 ppm, respectively, coupled to the ^{195}Pt nuclei by J_{Pt-P} = 3462 Hz and 3131 Hz, respectively. The magnitude of the J_{Pt-P} coupling constant indicates that the electron density at the platinum center is elevated. In fact, these high J_{Pt-P} coupling constants are comparable to those reported for a series of $(Cy_3P)_2Pt\rightarrow MX_n$ adducts which have been described as containing a Pt(0) center.[160-164] Moreover, these

coupling constants are significantly higher than those in **43** ($\delta(^{31}P)$ 50.9, J_{Pt-P} = 2566 Hz) indicating a drastic electronic property change at the platinum center.

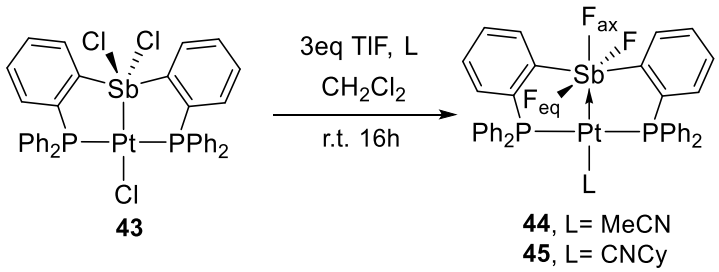

Figure 26. Synthesis of **44** and **45.**

2.3 Neutral trifluorostiborane platinum complex

Even though **44** was obtained, isolating reliable yields of the acetonitrile complex **44** has proved to be challenging, making an exploration of the chemistry of this complex complicated. For this reason, I decided to explore an alternative synthetic approach. Based on the assumption that chloride anion removal may be a problematic step, I decided to first proceed by replacing the three chloride ligands of **43** with three triflate anions (Figure 27). To this end, **43** was treated with MeCN and a slight excess of AgOTf in CH_2Cl_2.

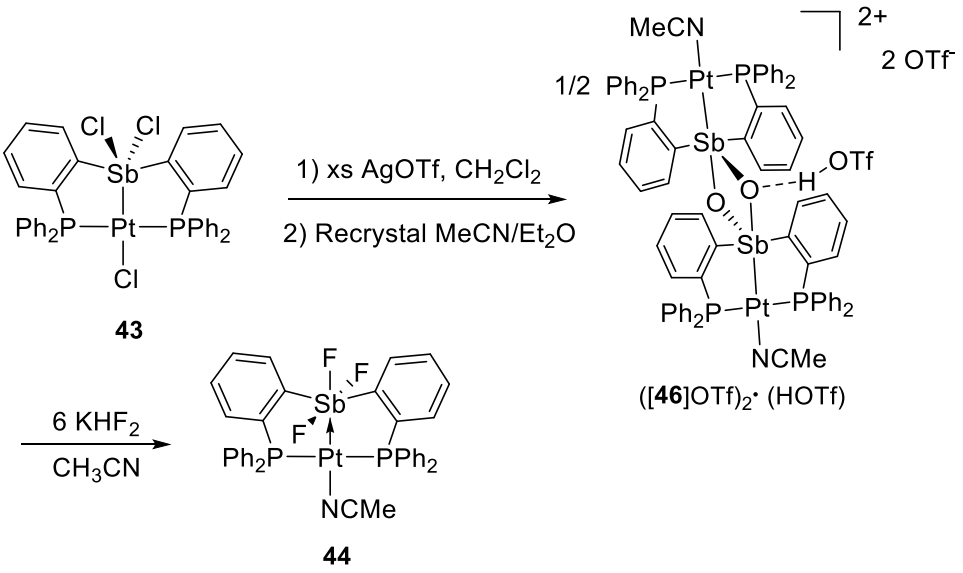

Figure 27. Alternative synthesis of **44**.

Recrystallization from MeCN/Et_2O did not afford the anticipated tris–triflate complex but rather [**46**]OTf, a complex which crystallizes with half an equiv. of HOTf (Figure 28). This cation forms a centrosymmetrical dimer featuring a central Sb_2O_2 four-membered ring. A careful inspection of the asymmetric unit indicates that the oxygen atom is protonated by half an equivalent of HOTf. The platinum center of this complex is again in a square planar geometry with the acetonitrile ligand trans to the antimony atom. The Sb–Pt distance of 2.5312(7) Å is close to that in **43**, indicating a strengthening of the Pt–Sb bonding when compared to **44** and **45** which possess longer Pt–Sb linkages (2.5797(2) Å for **44** and 2.6215(11) Å for **45**). The asymmetric unit contains an additional triflate anion that does not form any short contacts with the antimony center. As a result, the antimony atom adopts a distorted trigonal bipyramidal geometry, with two of its ligands being the bridging oxygen atoms. The Sb–O bond involving the axial oxygen atom O1'

(Sb–O1' 2.253(5) Å) is distinctly longer than that involving the equatorial oxygen atom O1 (Sb–O1 1.942(4) Å). The ^{31}P NMR spectrum of [**46**]OTf features a resonance at 60.8 ppm coupled to the ^{195}Pt nuclei by $J_{Pt–P}$ = 2832 Hz. Gratifyingly, I found that [**46**]OTf reacted cleanly with excess potassium bifluoride (KHF_2) in MeCN to afford **44** quantitatively (Figure 27). This route proved to be much more reliable than that described in Figure 26.

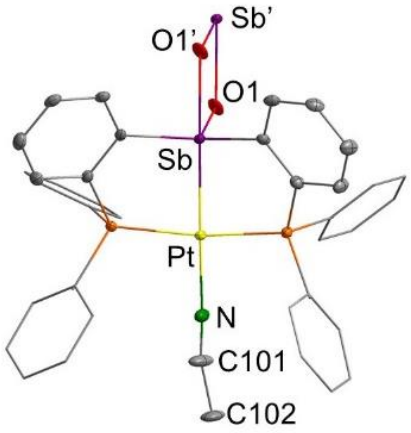

Figure 28. Solid-state structure of ([**46**]OTf)$_2$•(HOTf). Thermal ellipsoids are drawn at the 30% probability level. Phenyl groups are drawn in wireframe. Hydrogen atoms, triflate anions and triflic acid are omitted for clarity. Only the antimony and bridging oxygen atom of the second symmetry equivalent unit of [**46**]$^+$ are shown.

To gain a better understanding of the bonding in complexes **44** and **45**, I optimized their structures computationally using Density Functional Theory (DFT) methods (Gaussian program, functional: MPW1PW91; mixed basis set: Sb/Pt: cc-pVTZ-PP; P: 6-311++g**; N/F: 6–31+g(d'); C/H: 6–31g). Optimization of the geometry of these two complexes reproduced the trend in Sb–Pt distances observed experimentally, although

increased values were found for both complexes, with computed Sb–Pt distance being larger for **45** (**44**: 2.643 Å; **45**: 2.696 Å).

Table 1. Selected bond lengths (Å) and angles (°) for complexes **44** and **45** as determined crystallographically and optimized computationally.

Parameter	**44**		**45**	
	X–ray	DFT	X–ray	DFT
Sb–Pt	2.580 (2)	2.6431	2.621(1)	2.6964
Pt–N1 (C37)	2.125(2)	2.1378	2.005(5)	1.9889
Sb–F1	1.970(1)	1.9831	1.981(3)	1.9877
Sb–F2	1.992(1)	1.9960	1.991(3)	2.0077
Sb–F3	1.981(1)	1.9852	1.987(3)	1.9947
Pt–P1	2.292(6)	2.2986	2.288(1)	2.3007
Pt–P2	2.282(6)	2.2972	2.292(1)	2.3072
F(1)–Sb–F(2)	178.7(6)°	177.33°	172.7(9)°	176.22°
Sb–Pt–N1	176.4(6)°	175.47°	171.4(1)°	173.64°
P(1)–Pt–P(2)	170.5(2)°	171.20°	172.3(4)°	167.33°

Analyses of both structures using the natural bond orbital method (NBO) suggest that the Pt–Sb interactions are best described as donor–acceptor interactions, as the NBO analysis shows that **44** and **45** possesses a Pt→Sb interaction. This interaction involves donation from the filled platinum $4dx^2\text{-}y^2$ and $4dz^2$ orbitals into the vacant antimony 5px orbital. The same antimony orbital also accepts donation from a lone pair located on the fluorine atom trans to platinum. Further analysis of the NBO calculation results also indicate that second order perturbation energy $E^{(2)}$ corresponding to the strength of the Pt→Sb interaction is larger in **44** (89 kcal/mol) than in **45** (58 kcal/mol) (Figure 29). The

larger $E^{(2)}$ found for **44** is in agreement with its shorter Sb–Pt distance. It also suggests that the σ-acidic isocyanide ligand in **45** drains electron density from the platinum center and reduces its Lewis basicity. These NBO calculations also identify the other three filled d orbital on the platinum center. The emerging structure is one in which the platinum is in a d^{10} electronic configuration but engaged in dative interaction with the neighboring pentavalent antimony atom (Figure 30). This bonding situation can also be captured by considering the two resonance structures also shown in Figure 30.

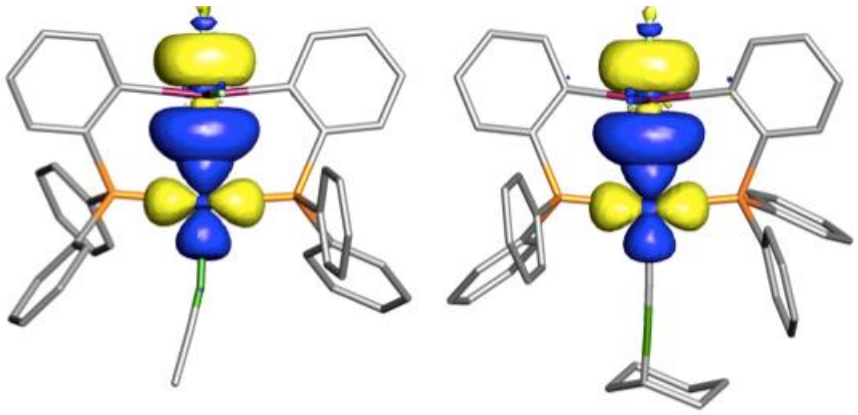

Figure 29. DFT-optimized structures of **44** (left) and **45** (right) with hydrogen atoms and anions omitted for clarity. NBO plots of the major Sb–Pt bonding interactions (isodensity value = 0.04).

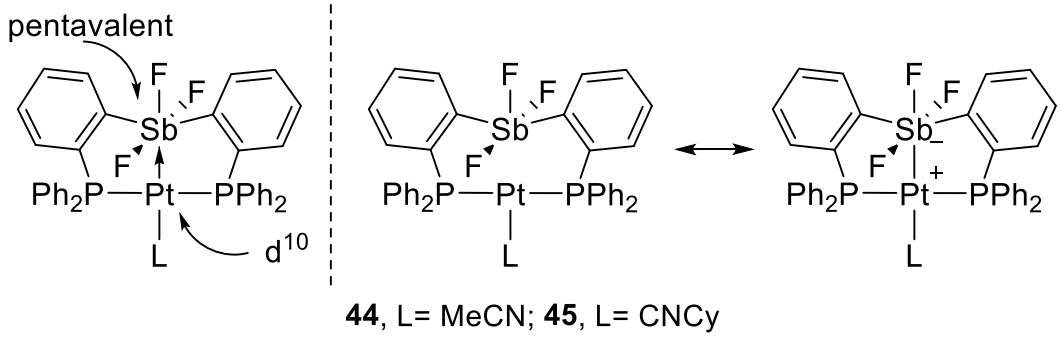

Figure 30. Structure of **44** and **45** represented using the dative formalism (left) and the Lewis formalism (right).

The bonding situation in **44** and **45** were also investigated by a quantum theory of atoms in molecules (QTAIM) analysis, which identifies a bond path between the antimony and platinum atoms in both structures (Figure 31). The value of the electron density at the Sb–Pt bond critical point (BCP) is higher for **44** (ρ (BCP) = 0.081 e bohr^{-3}) than for **45** (ρ(BCP) = 0.069 e bohr^{-3}). Similarly, the delocalization index (δ(A,B)), which corresponds to the number of electrons delocalized between two atoms, is higher in **44** (δ(Sb,Pt): 0.70 for **44** and 0.63 for **45**). These results agree with those obtained by NBO analysis. Finally, I note that the delocalization index calculated for complex **43** (δ(Sb,Pt): 0.97) is consistent for that expected for a covalent bond and is significantly higher than that in **44** and **45**. It follows that the antimony ligand switches from X-type in **43** to Z-type in **44** and **45**.[140]

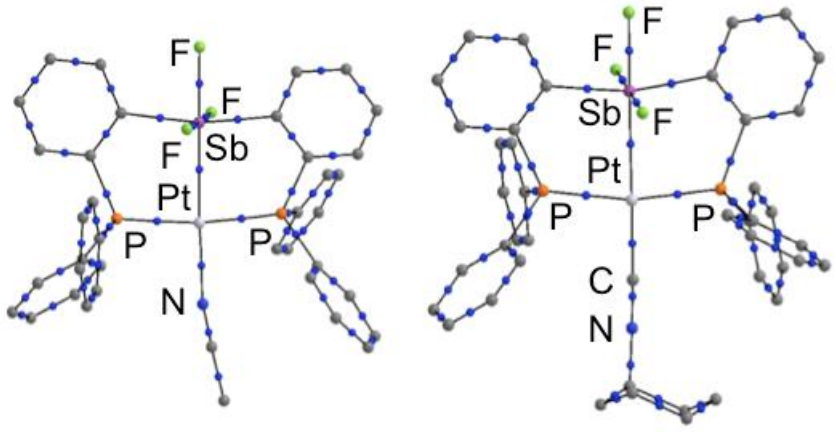

Figure 31. DFT-optimized structures of **44** (left) and **45** (right) with hydrogen atoms and anions omitted for clarity. Results of the QTAIM analysis showing selected bond paths and bond critical points with $\rho(BCP) > 0.02$ e bohr^{-3} (blue dots).

2.4 Cationic trifluorostiborane platinum complex

The platinum center in complexes **44** and **45** is isoelectronic with the gold centers of the recently reported gold catalysts [**38**]$^{+}$ and [**40**]$^{+}$ (

Figure 32).[125,152,153,157] Given this relationship, I questioned whether complexes **44** and **45** would mirror the carbophilic properties of [**40**]$^{+}$ and act as effective catalysts for the activation of alkynes.

To put this question to the test, I decided to benchmark the reactivity of these complexes against their ability to promote the cycloisomerization of dimethyl 2–allyl–2–(2–propynyl)malonate, a reaction that we have used to assess the reactivity of related antimony–platinum complexes (Figure 33).[165] Although such enyne cyclization reactions are known to be catalyzed by late transition metal complexes including those containing

platinum,[166,167] I found complexes **44** and **45** to be inactive when the reaction was carried out in $CDCl_3$ at room temperature.

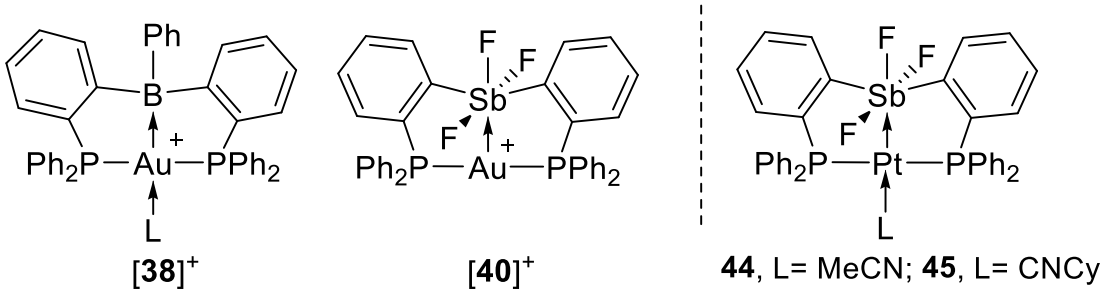

Figure 32. Similarity between the structures of **44** and **45** and those of the recently reported gold catalysts [**38**]$^+$ and [**40**]$^+$**.**

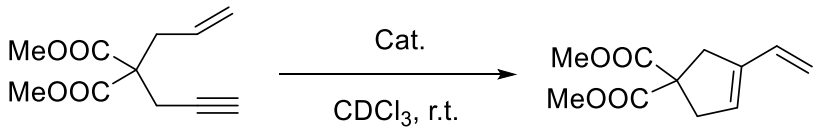

Figure 33. 1,6-Enyne cyclization catalysis.

I concluded from these experiments that the platinum center of these complexes may be too electron rich and not sufficiently electrophilic to efficiently activate alkynes. It occurred to us that this situation could be remediated by adopting the approach presented in Figure 25. Indeed, I speculated that fluoride anion abstraction from the antimony center would effectively increase the acidity of the latter, leading to a stronger Pt→Sb interaction, and consequently a more electrophilic platinum center.

To test this possibility, I treated complexes **44** and **45** in CH_2Cl_2 with 1 equiv. of $B(C_6F_5)_3$, a strong Lewis acid with a high affinity for fluoride anions (Figure 34). These

reactions proceeded cleanly to afford the cationic complexes [**47**]$^+$ and [**48**]$^+$, respectively. The ^{31}P NMR resonance recorded in situ for these new complexes appear as broad singlets at 51.8 ppm (J_{Pt-P} = 2404 Hz) for [**47**]$^+$ and 56.7 ppm (J_{Pt-P} = 2530 Hz) for [**48**]$^+$. The lower J_{Pt-P} coupling constants measured for [**47**]$^+$ and [**48**]$^+$ are consistent with a decrease in electron density at the platinum center. Although no signals could be observed corresponding to the antimony-bound fluoride, abstraction of a fluoride anion was confirmed by the appearance of new signals in the ^{19}F NMR spectrum at -134.7, -161.7, -166.1 ppm and a broad singlet -191.4 ppm corresponding to the $[BF(C_6F_5)_3]^-$ anion.[168]

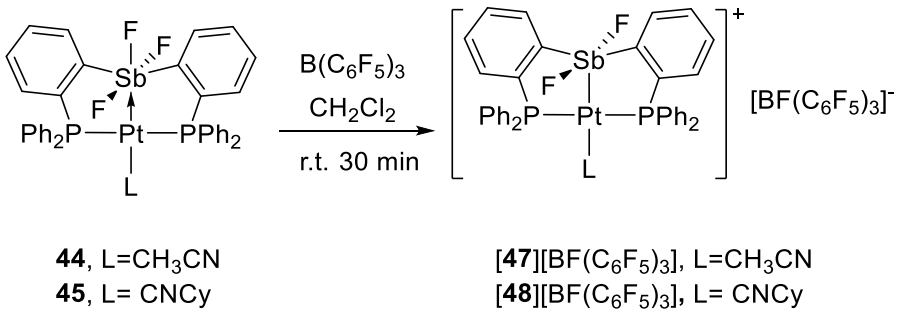

Figure 34. Synthesis of [**47**][$BF(C_6F_5)_3$] and [**48**][$BF(C_6F_5)_3$].

Crystals of complexes [**47**][$BF(C_6F_5)_3$] and [**48**][$BF(C_6F_5)_3$] were obtained and subjected to X–ray diffraction which indicated that both [**47**]$^+$ and [**48**]$^+$ form centrosymmetrical dimers connected by an Sb_2F_2 four-membered ring in the solid-state (Figure 35). This Sb_2F_2 is asymmetric; the fluorine atom trans from platinum forms a long Sb---F contact of 2.482(5) Å while the two fluorine atoms trans from each other form Sb–F1 and Sb–F2 bond distances of 1.977(6) Å and 2.08(6) Å. The coordination geometry of

the platinum centers in these two dimeric complexes remains square planar while that of antimony is distorted octahedral if one considers the bridging fluorine atom as occupying the coordination site trans to platinum. The Sb–Pt distances (2.5044(9) Å in [**47**]$^+$ and 2.5275(6) Å in [**48**]$^+$) are significantly shorter compared to those in complexes **44** (2.5797(2) Å) and **45** (2.6215(11) Å). This shortening of the Sb–Pt bond signals a more complete transfer of electron density from the platinum atom to the highly Lewis acidic difluorostibonium cation present in these complexes (*vide infra*). These structural changes validate the proposal that fluoride anion abstraction from antimony is an effective means for increasing the extent of electron density transfer from platinum to antimony.

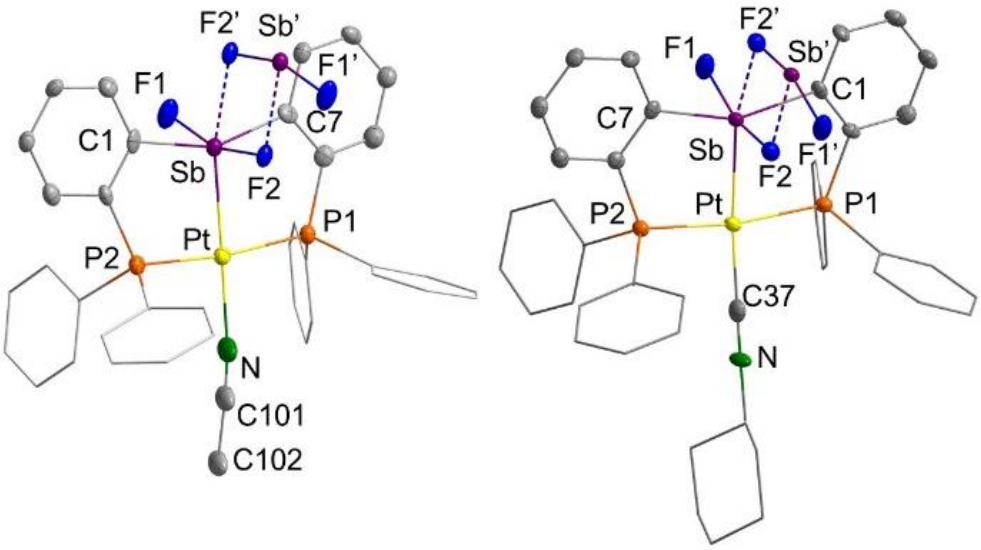

Figure 35. Solid-state structure of [**47**][$BF(C_6F_5)_3$]•(C_2H_6O) and [**48**][$BF(C_6F_5)_3$]•(CH_2Cl_2)$_2$. Thermal ellipsoids are drawn at the 50% probability level. Phenyl groups are drawn in wireframe. Only the cationic component of the salts is shown. Hydrogen atoms, solvent molecules and anions are omitted for clarity. Relevant metrical parameters can be found in the text or the SI. Only the antimony and fluorine atoms of the second, symmetry equivalent unit of [**47**]$^+$ and [**48**]$^+$, respectively are shown.

IR analysis of [**48**][$BF(C_6F_5)_3$] offers a consistent picture with the vibration energy of the isocyanide (ν_{CN} = 2214 cm^{-1}) being at higher energy than that in **45** (ν_{CN} = 2198 cm^{-1}). Dissolving these crystals in CH_2Cl_2 resulted in single ^{31}P NMR signals that correspond to those observed during the *in situ* reactions described above.

The computed Sb–Pt separations ([**47**]$^+$: 2.4860 Å; [**48**]$^+$: 2.5240 Å) are close to those measured by X-ray diffraction. It is interesting to note that an NBO analysis carried out on the optimized geometry describes the Sb–Pt bond as covalent and not as a donor-acceptor interaction as in **44** and **45** (Figure 36). The covalent nature of this bond is consistent with the existence of a more extensive transfer of electron density from platinum to antimony. The covalent Sb–Pt bonds in [**47**]$^+$ and [**48**]$^+$ give rise to natural localized molecular orbitals (NLMOs) that span the two heavy atoms. Inspection of these NLMOs show that the two heavy atoms contribute almost equally although the orbital contribution from platinum is slightly larger than that of antimony (Sb: 44.7%; Pt: 49.3% for [**47**]$^+$; Sb: 44.8%/Pt: 48.8% for [**48**]$^+$).

Table 2. Selected bond lengths (Å) and angles (°) for complexes [**47**][$BF(C_6F_5)_3$] and [**48**][$BF(C_6F_5)_3$] as determined crystallographically and optimized computationally.

Parameter	[**47**][$BF(C_6F_5)_3$]		[**48**][$BF(C_6F_5)_3$]	
	X-ray	DFT	X-ray	DFT
Sb–Pt	2.504(9)	2.4860	2.527(6)	2.5240
Pt–N1 (C37)	2.149(1)	2.0634	2.005(6)	1.9875
Sb–F1	1.977(6)	1.9927	1.982(3)	1.9930
Sb–F2	2.086(5)	1.9945	2.084(2)	1.9954
Sb–F2'$_{axial}$	2.482(5)	n/a	2.475(3)	n/a
Pt–P1	2.304(3)	2.3356	2.288(1)	2.3369
Pt–P2	2.302(3)	2.3356	2.287(2)	2.3360
F(1)–Sb–F(2)	162.6(2)^o	159.20^o	162.9(1) ^{o}	157.14^o
Sb–Pt–N1(C37)	178.0(3)^o	174.40^o	169.9(2) ^{o}	173.65^o
P(1)–Pt–P(2)	172.8(9)^o	166.97^o	171.5(5) ^{o}	165.19^o

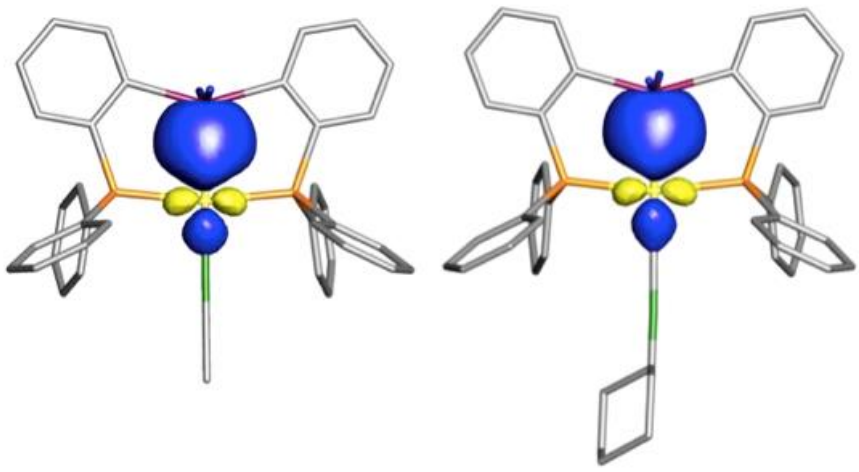

Figure 36. DFT-optimized structures of [**47**]$^+$ and of [**48**]$^+$ with hydrogen atoms and anions omitted for clarity. NLMO plots of the major Sb–Pt bonding interactions (isodensity value = 0.04).

These NBO results are supported by a AIM analysis of these two complexes which show that the density at the Sb–Pt bond critical points (ρ(BCP)) of [**47**]$^+$ (0.102 e bohr^{-3}) and [**48**]$^+$ (0.096 e bohr^{-3}) are significantly higher than those in **44** (0.081 e bohr^{-3}) and **45** (0.069 e bohr^{-3}) (Figure 37). The same is true about the delocalization indices σ(Sb,Pt) which are higher in [**47**]$^+$ (0.92) and [**48**]$^+$ (0.87) than in **44** (0.70) and **45** (0.63). The computational results reinforce the notion that fluoride anion abstraction from antimony promotes electron depletion at platinum.

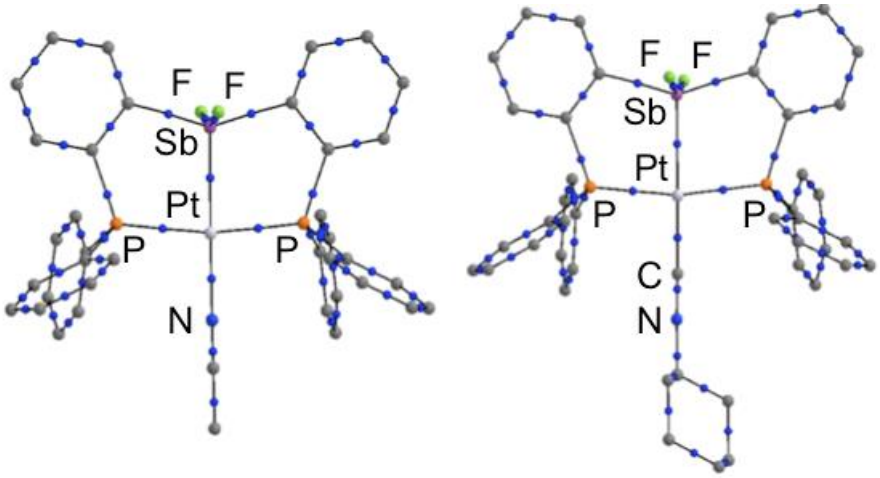

Figure 37. DFT-optimized structures of [**47**]$^+$ and of [**48**]$^+$ with hydrogen atoms and anions omitted for clarity. Results of the QTAIM analysis showing selected bond paths and bond critical points with ρ(BCP) > 0.02 e bohr^{-3} (blue dots).

With the view to assess the impact of these electronic structure changes on the reactivity of the platinum center, I decided to again benchmark the carbophilic character of the latter using the cycloisomerization of dimethyl 2–allyl–2–(2–propynyl)malonate. Like compounds **44** and **45**, I found that [**48**]$^+$, generated in situ by addition of $B(C_6F_5)_3$,

fails to promote the reaction. Bearing in mind that dissociation of the L ligand is a prerequisite for catalysis, I became eager to test [**47**]$^+$ which contains a more labile acetonitrile ligand. Gratifyingly, I found that [**47**]$^+$ promoted quantitative formation of vinylcyclopentene which was completed after 4 h when a 2% catalyst loading was employed.

2.5 Conclusion

The first important outcome of this work is the demonstration that simple chloride-for-fluoride anion exchange reactions at the $[Cl_2Sb–PtCl]^{2+}$ core of 1 can be used to induce a reorganization of the halide ligands about the dinuclear core leading to formation of a $[F_3Sb–PtL]^{2+}$ unit. These changes have a profound effect on the nature of the Pt–Sb bond which switches from being covalent and apolar in **43** to polar covalent in the case of **44** and **45**. In the extreme of the dative formalism, **44** and **45** can be described as possessing a Pt(0)→Sb(V) interaction. It follows that the platinum center of **44** and **45** is rather electron rich, leading to low electrophilic characteristics. A second outcome of this work is the observation that a fluoride anion can be readily abstracted from the newly formed diaryltrifluorostiborane moiety present **44** and **45**, leading to formation of [**47**]$^+$ and [**48**]$^+$ respectively. Formation of these new complexes is accompanied by conversion of the diaryltrifluorostiborane unit of **44** and **45** into a highly Lewis acidic diaryldifluorostibonium moiety. In turn, the antimony center of [**47**]$^+$ and [**48**]$^+$ displays increased σ-accepting properties leading to a strengthening of the Pt→Sb interaction. The stronger electron donation from platinum to antimony impacts the reactivity of the platinum center which becomes sufficiently electrophilic in the case of [**47**]$^+$ to catalyze

enyne cyclization reactions. As a whole, this work highlights a new strategy for controlling the catalytic reactivity of transition metals via ligand-centered anion abstraction reaction. This work complements existing approaches for the modulation of the Z-type ligand strength by substituent effects,[153] by replacement of the Lewis acidic atom[104,105,122] or by a change of its oxidation state.[125,157] It also reveals a functional facet of the coordination non-innocence of antimony ligand which can be manipulated to enhance catalysis at a nearby transition metal site.

2.6 Experimental

General considerations: Cis–$PtCl_2(Et_2S)_2$, [(*o*–$(Ph_2P)C_6H_4)_2SbCl$] and complex **43** were prepared according to the reported procedures.[159,169] Solvents were dried by passing through an alumina column (*n*–pentane and CH_2Cl_2) or by reflux under N_2 over Na/K (Et_2O). All other solvents were used as received. Commercially available chemicals were purchased and used as provided (Commercial sources: Acros Organics for thallium fluoride; Strem chemicals for cyclohexyl isocyanide). Ambient temperature NMR spectra were recorded on a Varian Unity Inova 500 FT NMR (499.42 MHz for ^1H, 125.58 MHz for ^{13}C, 469.89 MHz for ^{19}F, 202.16 MHz for ^{31}P), a Varian Unity Inova 400 FT NMR (161.74 MHz for ^{31}P) and an Inova 300 FT NMR (121.49 MHz for ^{31}P, 282.40 MHz for ^{19}F). ^1H and ^{13}C NMR chemical shifts are given in ppm and are referenced against $SiMe_4$ using residual solvent signals used as secondary standards. ^{19}F NMR chemical shifts are given in ppm and are referenced against $CFCl_3$ using BF_3–Et_2O as an external secondary standard with δ -153.0 ppm. ^{31}P NMR chemical shifts are given in ppm and are referenced

against H_3PO_4 as an external standard. Elemental analyses (EA) were performed at Atlantic Microlab (Norcross, GA).

Computational Details: Density functional theory (DFT) structural optimizations were performed on the solid-state structures using Gaussian 09 suite of programs with effectivecore potentials on all heavy atoms (functional: BP86; mixed basis set: Sb/Pt: cc-pVTZ-PP; P: 6-31g(d); H/C/O: 6-31g, F: 6-31+g(d'). Frequency calculations were used to confirm convergence of thecalculations. The optimized structures, which are in excellent agreement with the solid-state structures,were subjected to a NBO analysis and were visualized and plotted using the Jimp 2 program.[170]

Crystallographic Measurements: The crystallographic measurements were performed at 110(2) K using a Bruker APEX–II CCD area detector diffractometer (Mo-Kα radiation, κ = 0.71069 A). In each case, a specimen of suitable size and quality was selected and mounted onto a nylon loop. The structures were solved by direct methods, which successfully located most of the non-hydrogen atoms. Semi-empirical absorption corrections were applied. Subsequent refinement on F2 using the SHELXTL/PC package (version 6.1) allowed location of the remaining non-hydrogen atom.

Synthesis of 44: Method 1: This method was inspired from the work of Haifeng Yang but with reaction conditions and reagent amounts that are different from what she used.[171] A CH_2Cl_2 solution (8 mL) of complex **43** (80 mg, 0.085 mmol) was combined with CH_3CN (4 mL), stirred for 30 min, and treated with solid TlF (96 mg, 0.43 mmol). The resulting mixture was stirred for 16 h, filtered and brought to dryness to afford an oily residue. This residue was treated with Et_2O (10 mL) and sonicated, leading to the

formation of **44** as a pale-yellow solid. This method only afforded 15 mg of a solid, the NMR spectra of which showed the presence of **44**. However, elemental analysis indicated that this solid also contained inorganic impurities. For this reason, no reliable yield could be determined.

Method 2: A MeCN solution (6 mL) of [**46**]OTf (57.5 mg, 0.027 mmol) was treated with KHF_2 (12.9 mg, 0.17 mmol). The reaction mixture was stirred for 2 h, which afforded a colorless solution. After evaporation of the solvents under vacuum, the resulting white solid was extracted with $CHCl_3$ (20 mL) and filtered over a plug of Celite. The resulting solution was brought to dryness to afford a residue which was dissolved in a 1:1 CH_2Cl_2 (1 mL) / $CHCl_3$ (1 mL) solution. Slow evaporation of the solvents inside a nitrogen-filled glove box afforded **44**•0.6 ($CHCl_3$) (see EA results below) as a pale yellow solid (17.9 mg, 29 % yield). ^{1}H NMR (499.42 MHz; CD_2Cl_2): δ 8.59 (d, $^3J_{H–H}$ = 7.5 Hz, 2H, *o*–P(Sb)C_6H_4), 7.71-7.39 (m, 24H), 7.35 (t, $^3J_{H–H}$ = 7.6 Hz, 2H), 1.59 (s, 3H, CH_3CN). ^{13}C{^{1}H}NMR (125.58 MHz; CD_2Cl_2): δ 134.10 (s), 131.68 (s), 131.27 (brs), 129.60 (brs), 129.03 (t, $J_{C–P}$ = 5.1 Hz), 105.43 (s), 2.67 (s, CH_3CN). ^{31}P{^{1}H} NMR (202.16 MHz; CD_2Cl_2): δ 71.8 (d, $J_{Fax–P}$ = 11.7 Hz, $J_{Pt–P}$ = 3462 Hz). ^{19}F{^{1}H} NMR (469.89 MHz; CD_2Cl_2): δ -83.8 (d, 2Feq, $J_{Fa–Feq}$ = 40.1 Hz, $J_{Pt–Feq}$ = 171 Hz), -113.3 (m, 1Fa). Elemental analysis calcd (%) for $C_{38}H_{31}F_3NP_2PtSb$•0.6 ($CHCl_3$): C 45.94, H 3.16, N 1.39; found: C 45.98, H 3.16, N 1.23. These EA results are consistent with partial loss of the two interstitial $CHCl_3$ molecules observed in the crystal structure of this compound. Single crystals of **44**•$(CHCl_3)_2$ were obtained by slow evaporation of a $CDCl_3$ solution of **44** at ambient temperature.

Synthesis of [46]OTf: To a stirred solution of **43** (245 mg, 0.26 mmol) in CH_2Cl_2 (8 mL) was added solid AgOTf (266 mg, 1.04 mmol). The resulting mixture was stirred for 16 h, filtered and brought to dryness to afford a white solid. Recrystallization of this solid from a 1:1 MeCN (2 mL) / Et_2O (2 mL) solution afforded white solid of [**46**]OTf•0.6 (HOTf) (222 mg, 76% yield). ^{1}H NMR (499.42 MHz; CD_3CN): δ 7.79 (t, 2H, C_6H_5, $^3J_{H–H}$ = 6.5 Hz), 7.75-7.63 (m, 10H, *o*–P(Sb)C_6H_4+PC_6H_5), 7.62-7.57 (m, 2H, *o*–P(Sb)C_6H_4), 7.54 (t, 2H, $^3J_{H–H}$ = 7.3 Hz, PC_6H_5), 7.50 (t, 2H, $^3J_{H–H}$ = 7.1 Hz, *o*–P(Sb)C_6H_4), 7.45 (t, 4H, $^3J_{H–H}$ = 7.6 Hz, PC_6H_5), 7.23 (dt, 4H, $^3J_{H–H}$ = 6.9 Hz, $^3J_{H–H}$ = 6.2 Hz, PC_6H_5), 7.11 (t, 2H, $^3J_{H–H}$ = 7.7 Hz, *o*–P(Sb)C_6H_4), 1.96 (s, 3H). ^{13}C{^{1}H} NMR (125.58 MHz; CD_3CN): δ 128.60 (t, $J_{C–P}$ = 28.7 Hz), 129.64 (t, $J_{C–P}$ = 28.7 Hz), 129.64 (t, $J_{C–P}$ = 6.9 Hz), 131.00 (t, $J_{C–P}$ = 5.7 Hz), 133.13 (s), 133.72 (t, $J_{C–P}$ = 6.7 Hz), 134.08 (s), 134.24 (s), 135.28 (t, $J_{C–P}$ = 7.7 Hz), 135.48 (t, $J_{C–P}$ = 8.9 Hz). ^{31}P{^{1}H} NMR (202.16 MHz; CD_3CN): δ 60.8 ($^1J_{Pt–P}$ = 2832 Hz). Elemental analysis calcd (%) for $C_{39}H_{31}F_3NO_4P_2PtSSb$•0.6 ($HSO_3CF_3$): C, 41.88; H, 2.80; N, 1.23. Found: C, 41.52; H, 2.67; N, 1.17. These EA results are consistent, within error, with the crystal structure of [**46**]OTf which showed the presence 0.5 equiv. of HOTf. As further evidence for the presence of HOTf, the ^{1}H and ^{19}F NMR spectrum of [**46**]OTf was recorded in the presence of pentafluoroacetophenone as a combined ^{1}H/^{19}F integration standard. This NMR method suggested the presence of 0.67 equiv. of HOTf which is consistent, within error, with the X-ray and crystallographic results. Single crystals of [**46**]OTf•0.5 (HOTf) were obtained by slow diffusion of Et_2O into a MeCN solution at ambient temperature.

Generation of [47][BF(C_6H_5)$_3$]: B(C_6H_5)$_3$ (12.6 mg, 0.03 mmol) was added to a stirred CH_2Cl_2 (2 mL) solution of complex **44** (25 mg, 0.03 mmol). This solution turned from pale yellow to colorless over the course of 30 min. The reaction mixture was analyzed using NMR spectroscopy. $^{31}P\{^1H\}$ NMR (121.49 MHz; CH_2Cl_2): δ 51.8 (brs, J_{Pt-P} = 2404 Hz). $^{19}F\{^1H\}$ NMR (282.40 MHz; CH_2Cl_2): δ -134.1 (s, 6F), -160.9 (s, 3F), -165.4 (s, 6F), -186.4 (brs, 1F). A resonance for the Sb-bound fluorine atoms was not observed. A unique single crystal of [**47**][BF(C_6H_5)$_3$]•Et_2O was obtained by slow diffusion of Et_2O into a CH_2Cl_2 solution of [**47**][BF(C_6H_5)$_3$] at room temperature inside a glovebox.

Synthesis of [48][BF(C_6H_5)$_3$]: B(C_6H_5)$_3$ (27.0 mg, 0.05 mmol) was added to a stirred CH_2Cl_2 (2 mL) solution of complex **45** (53 mg, 0.05 mmol). The solution turned from pale yellow to colorless over the course of 30 min. The solution was treated with Et_2O (2 mL), leading to the precipitation of [**48**][BF(C_6H_5)$_3$] as an off-white solid. Compound [**48**][BF(C_6H_5)$_3$] was subsequently dried under vacuum (62 mg, 77% yield). 1H NMR (499.42 MHz; $CDCl_3$): δ 8.20 (brs, 2H, *o*–P(Sb)C_6H_4), 7.68-7.28 (m, 22H), 7.18 (brs, 3H), 1.53-1.37 (brs, 2H, Cy–CH), 1.35-1.22 (brs, 2H, Cy–CH), 1.22-0.99 (brs, 5H, Cy–CH), 0.98-0.77 (brs, 2H, Cy–CH). $^{13}C\{^1H\}$ NMR (125.58 MHz; $CDCl_3$): δ 21.83 (s), 22.32 (s), 24.06 (s, Cy–CH), 30.96 (s, Cy–CH), 55.57 (s, Cy–CH), 129.52 (s), 131.40 (s), 132.21 (s), 132.52 (s), 133.08 (brs), 134.08 (s), 135.37 (m), 137.50 (m), 139.52 (brs), 146.89 (brs), 148.80 (brs). $^{31}P\{^1H\}$ NMR (161.74 MHz; CD_2Cl_2): δ 56.7 (brs, J_{Pt-P} = 2530 Hz). $^{19}F\{^1H\}$ NMR (469.89 MHz; $CDCl_3$): δ -134.7 (s, 6F), -161.7 (s, 3F), -166.1 (s, 6F), -191.4 (brs, 1F). A resonance for the Sb-bound fluorine atoms was not observed. Elemental analysis calcd (%) for $C_{61}H_{39}NBF_{18}P_2PtSb$: C, 48.28; H, 2.59. Found: C, 48.49;

H, 2.79. Single crystals of [**48**][$BF(C_6F_5)_3$]•$(CH_2Cl_2)_2$ were obtained from a 1:1 hexane (2 mL) / CH_2Cl_2 (2 mL) solution, upon slow evaporation (2 days) of the solvents inside a nitrogen-filled glovebox.

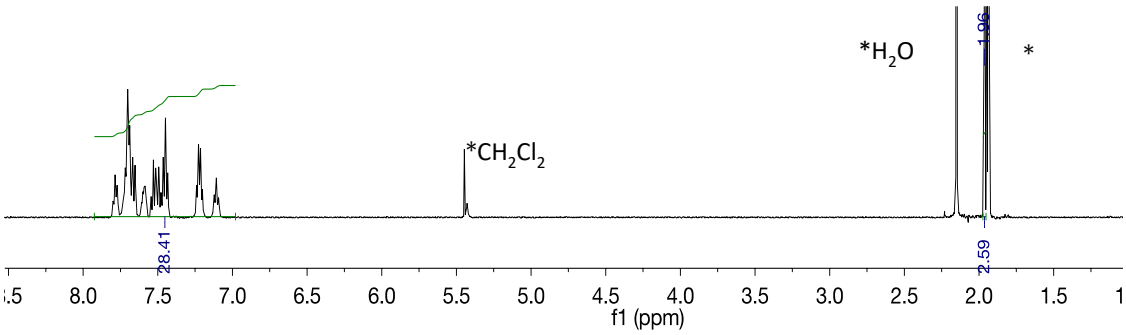

Figure 38. ^{1}H NMR spectrum of [**46**]OTf in CD_3CN. The CD_3CN solvent residue peak has been truncated and marked by an asterisk (*).

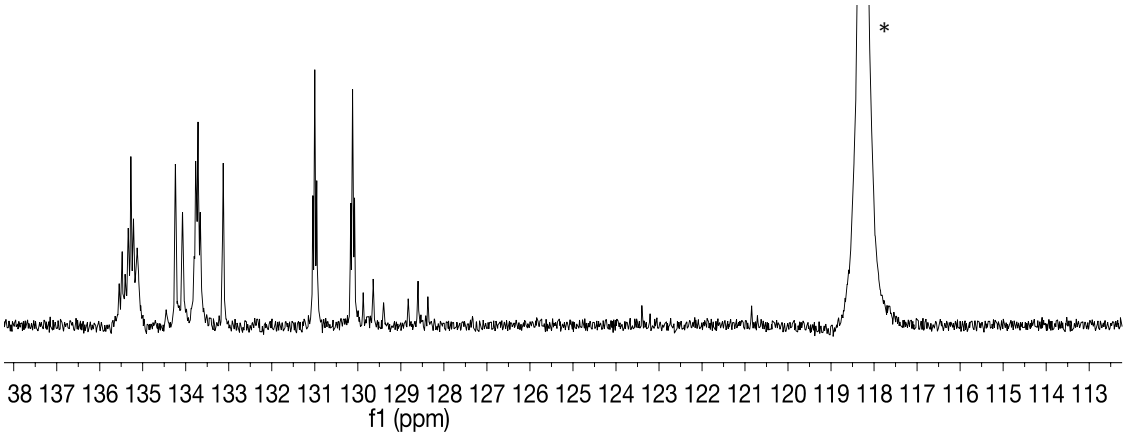

Figure 39. ^{13}C NMR spectrum of [**46**]OTf in CD_3CN. The CD_3CN solvent residue peak has been truncated and marked by an asterisk (*).

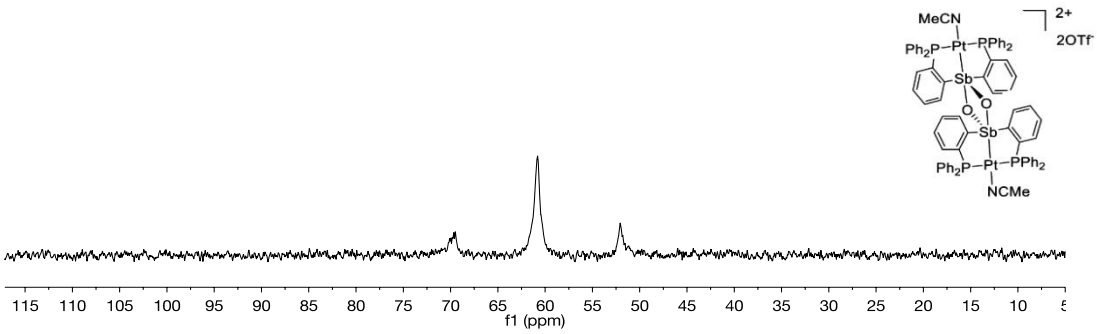

Figure 40. ^{31}P NMR spectrum of [**46**]OTf in CD_3CN.

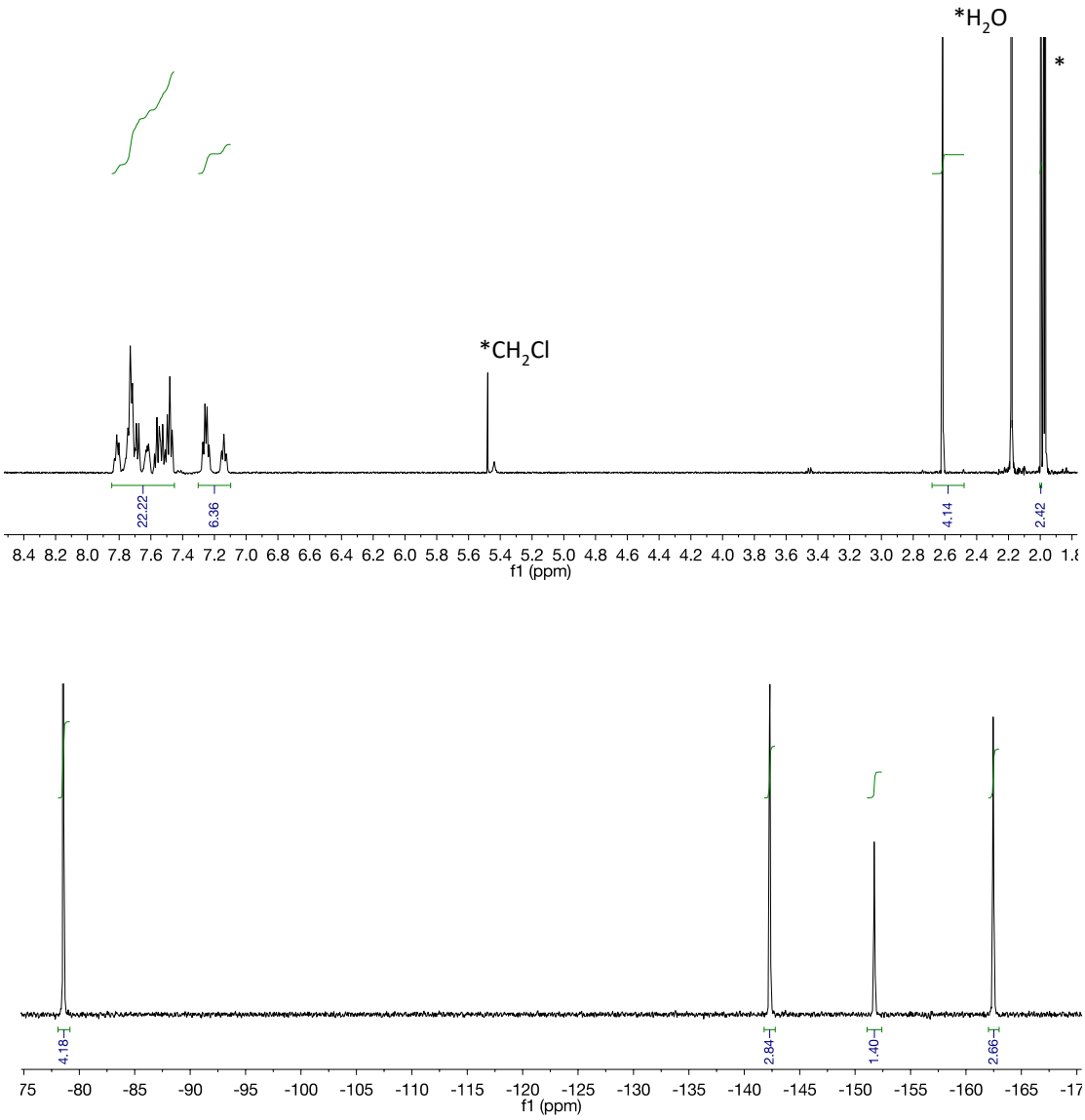

Figure 41. ^{1}H NMR (top) and ^{19}F NMR (bottom) spectrum of [**46**]OTf in CD_3CN with pentafluoroacetophenone as an internal standard for the determination of the HOTf content. The CD_3CN solvent residue peak has been truncated and marked by an asterisk (*).

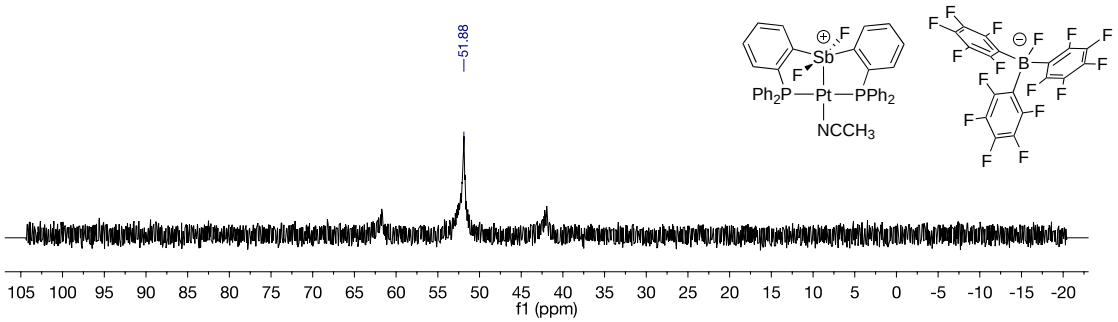

Figure 42. In situ ^{31}P NMR spectrum of [**47**][BF(C_6F_5)$_3$] in CH_2Cl_2.

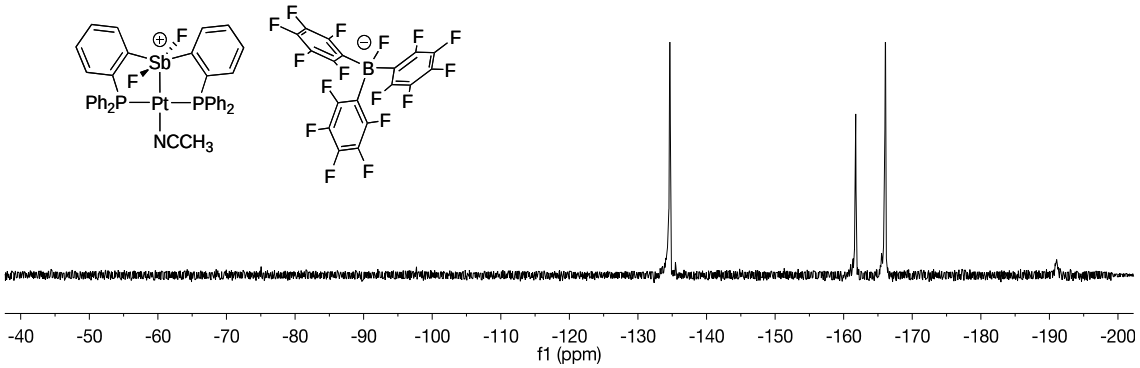

Figure 43. *In situ* ^{19}F NMR spectrum of [**47**][BF(C_6F_5)$_3$] in CH_2Cl_2.

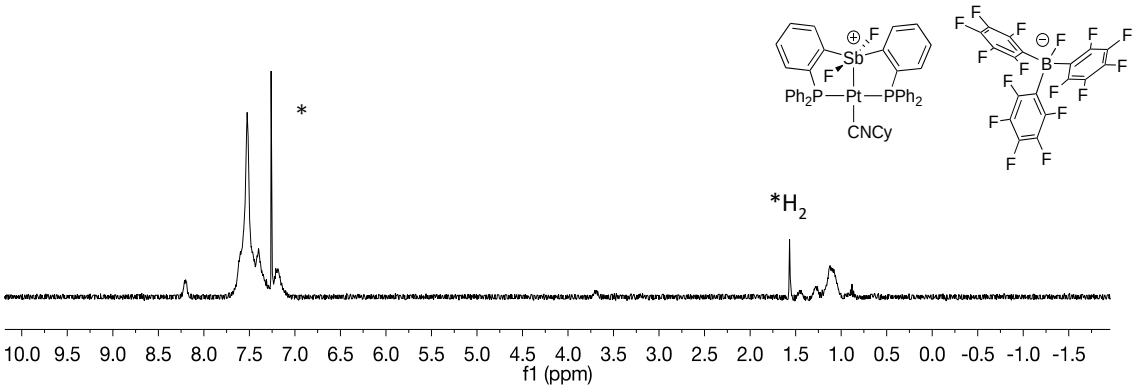

Figure 44. ^{1}H NMR spectrum [**48**][BF(C_6F_5)$_3$] in $CDCl_3$. The $CDCl_3$ solvent residue is marked by an asterisk (*).

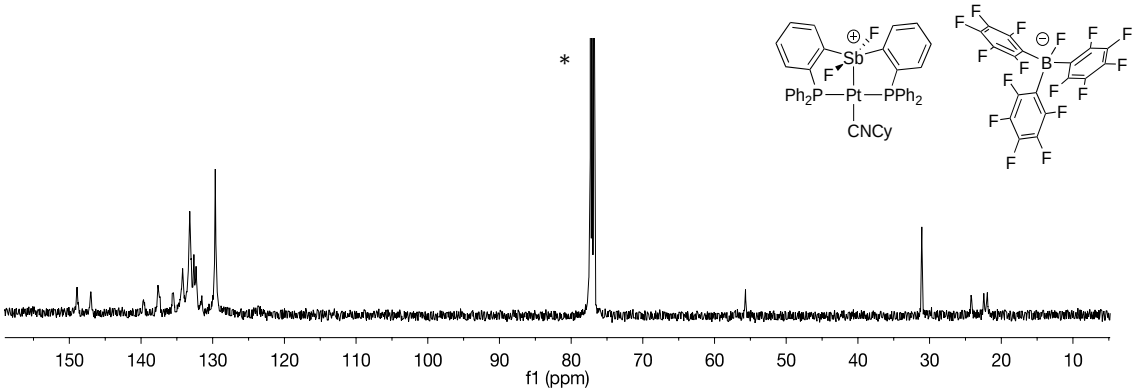

Figure 45. ^{13}C NMR spectrum of [**48**][BF(C_6F_5)$_3$] in $CDCl_3$. The $CDCl_3$ solvent residue peak has been truncated and marked by an asterisk (*)

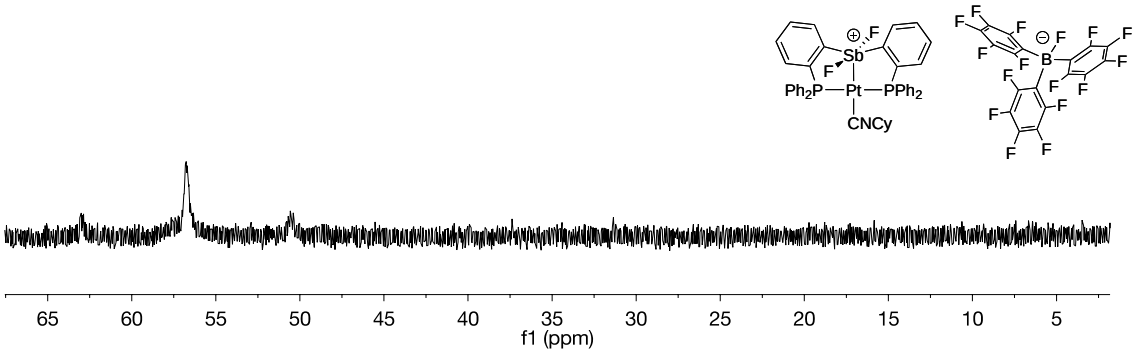

Figure 46. ^{31}P NMR spectrum of [**48**][BF(C_6F_5)$_3$] in $CDCl_3$.

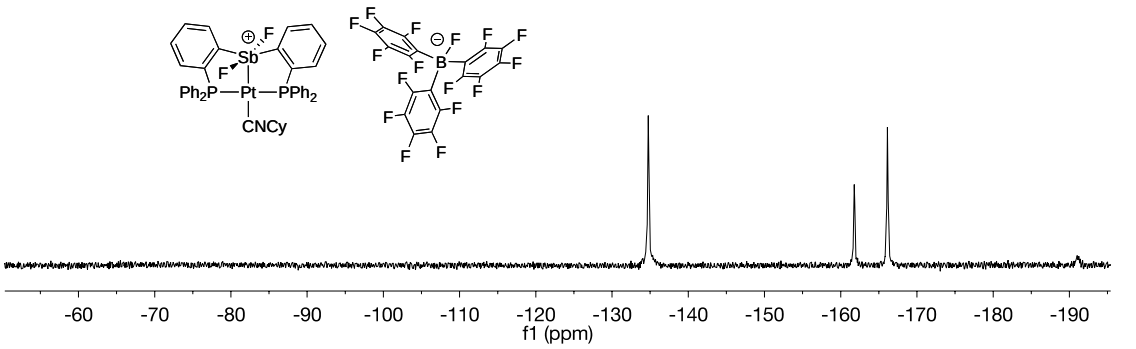

Figure 47.^{19}F NMR spectrum of [**48**][BF(C_6F_5)$_3$] in $CDCl_3$.

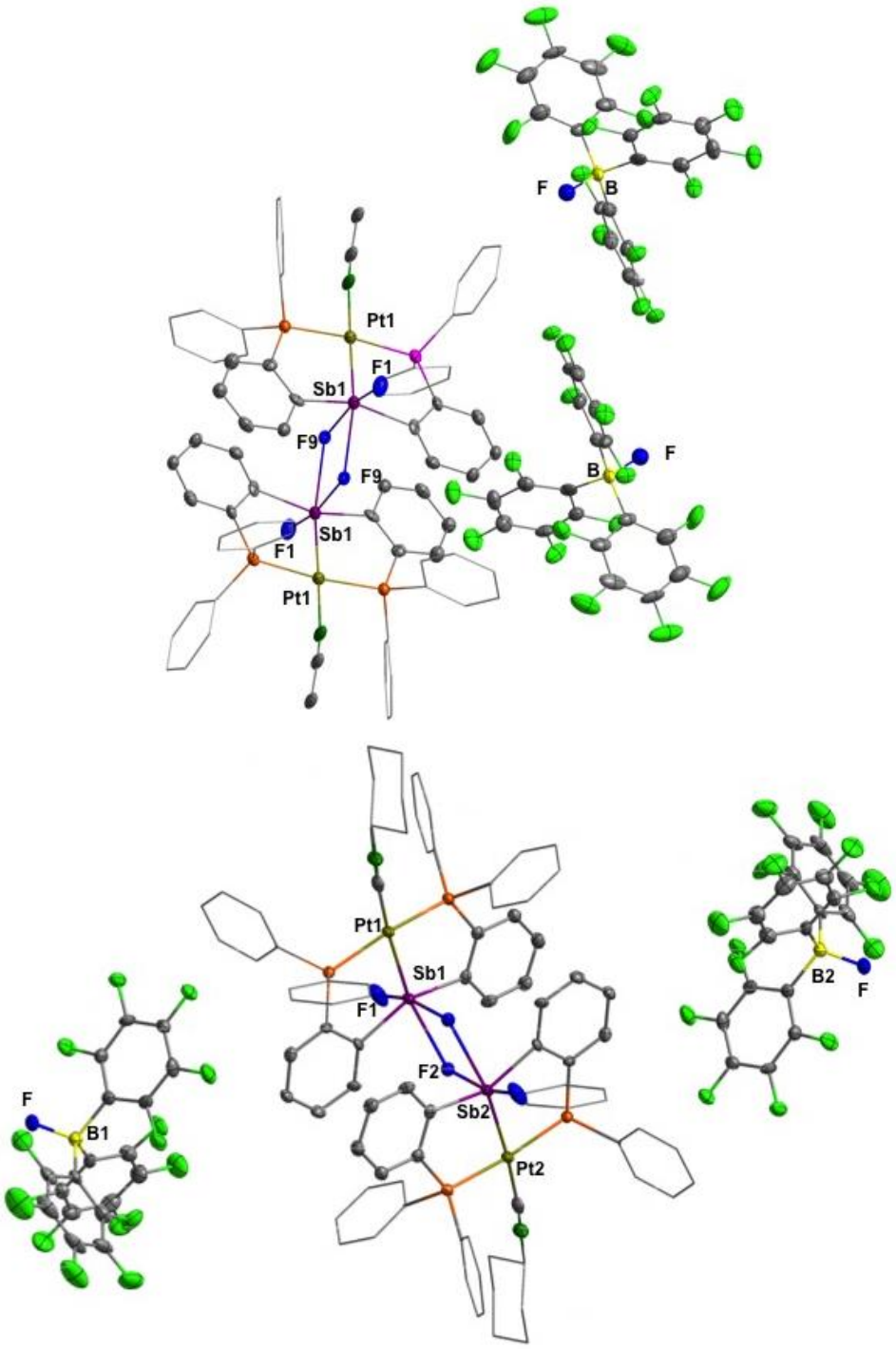

Figure 48. Solid-state structure of [**47**][$BF(C_6F_5)_3$] (top) and [**48**][$BF(C_6F_5)_3$] (bottom). Thermal ellipsoids are drawn at the 50% probability level. Phenyl groups are drawn in wireframe. Hydrogen atoms, solvent molecules are omitted for clarity.

CHAPTER III

UNMASKING THE CATALYTIC ACTIVITY OF A PLATINUM COMPLEX WITH A LEWIS ACIDIC, NON-INNOCENT ANTIMONY LIGAND*

3.1 Introduction

The activation of transition metal catalyst by anionic ligand abstraction is a strategy that has met considerable success in various areas of organometallic catalysis.[172,173] Such reactions typically necessitate the use of a Lewis acid activator which sequesters the anionic ligand. Over the past few years, efforts to introduce the Lewis acid within the ligand architecture have led to complexes that activate a variety of bonds[92,174-178] or catalyze hydrogenation[91,148] and alkyne activation reactions[179] among others.[102] In most cases, these systems employ boron or a heavier group 13 element as the Lewis acid.[102] Given the inherent water and oxygen sensitivity of organo-group 13 compounds, efforts to design catalysts in which the Lewis acid is a more chemically resistant moiety could become advantageous. Motivated by this possibility, we have decided to consider complexes in which the role of the Lewis acid is fulfilled by antimony.[142]

While it is often assumed that antimony ligands[180] display ligative properties related to those of their lighter congeners, these ligands possess a number of atypical features, including redox activity.[100,138,181] Another unusual trait of these ligands pertains

---

*Reprinted with permission from "Unmasking the Catalytic Activity of a Platinum Complex with a Lewis Acidic, Non-innocent Antimony Ligand" You, D.; Gabbaï, F. P. *J. Am. Chem. Soc.* **2017**, *139*, 6843. Copyright 2017 American Chemical Society

to the Lewis acidic behavior they sometime display when bound to metals and which allow them to adopt variable coordination numbers.[33,138,143,158] This property, which we refer to as coordination non-innocence, is illustrated by a series of recent accounts showing that stibines, even when bound to transition metals, are able to coordinate anions.[101,141,144] This behavior also comes to light in the chemistry of the platinum complex **A** whose stiboranyl moiety is readily converted into a fluorostiborane (**B**) upon reaction with fluoride.[139] This fluoride-induced reaction affects the platinum center, which switches from a tetravalent state in **A** to a divalent state in **B**.

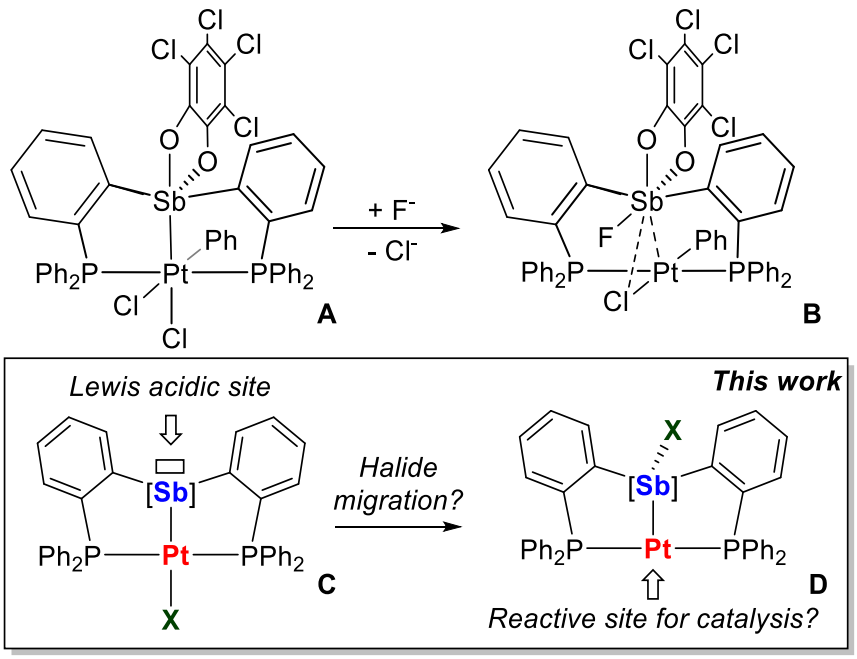

Figure 49. Lewis acidic behavior of antimony ligands.

It occurred to us that such an internal halide transfer reaction could be exploited as a means to increase the reactivity of the metal center with possible applications in the

domain electrophilic catalysis. Stimulated by this prospect, I have decided to focus on antimony platinum platforms of type **C**[159] and test whether a spontaneous halide migration reaction could lead to the unmasking of an exposed[111,160,182-184] and thus potentially reactive platinum center[176] as in **D** (Figure 49).

The activation of transition metal catalyst by anionic ligand abstraction is a strategy that has met considerable success in various areas of organometallic catalysis.[172,173] Such reactions typically necessitate the use of a Lewis acid activator which sequesters the anionic ligand. Over the past few years, efforts to introduce the Lewis acid within the ligand architecture have led to complexes that activate a variety of bonds[92,174-178] or catalyze hydrogenation[91,148] and alkyne activation reactions[179] among others.[102] In most cases, these systems employ boron or a heavier group 13 element as the Lewis acid.[102] Given the inherent water and oxygen sensitivity of organo-group 13 compounds, efforts to design catalysts in which the Lewis acid is a more chemically resistant moiety could become advantageous. Motivated by this possibility, I have decided to consider complexes in which the role of the Lewis acid is fulfilled by antimony.[141]

While it is often assumed that antimony ligands[180] display ligative properties related to those of their lighter congeners, these ligands possess a number of atypical features, including redox activity.[100,134,181] Another unusual trait of these ligands pertains to the Lewis acidic behavior they sometime display when bound to metals and which allow them to adopt variable coordination numbers.[33,138,143,158] This property, which we refer to as coordination non-innocence, is illustrated by a series of recent accounts showing that stibines, even when bound to transition metals, are able to coordinate anions.[100,141,144] This

behavior also comes to light in the chemistry of the platinum complex **A** whose stiboranyl moiety is readily converted into a fluorostiborane (**B**) upon reaction with fluoride.[139] This fluoride-induced reaction affects the platinum center, which switches from a tetravalent state in **A** to a divalent state in **B**. It occurred to us that such an internal halide transfer reaction could be exploited as a means to increase the reactivity of the metal center with possible applications in the domain electrophilic catalysis. Stimulated by this prospect, we have decided to focus on antimony platinum platforms of type **C**[159] and test whether a spontaneous halide migration reaction could lead to the unmasking of an exposed[111,160,182-184] and thus potentially reactive platinum center[176] as in **D** (Figure 49).

3.2 Investigating dichlorostiboranyl platinum complex

To test the hypothesis articulated in Figure 49, I decided to investigate whether the addition of a donor ligand could be used to promote the proposed bimetallic core rearrangement (Figure 50). While complex **43** has poor solubility in dichloromethane, I observed that addition of CyNC results in the formation of a clear solution from which crystals could be grown by simple evaporation of pentane to a dichloromethane solution. I found that these crystals correspond to **49**, a complex in which the three chloride ligands are now coordinated to the antimony atom. This complex has been characterized by X-ray diffraction and solid-state ^{31}P NMR spectroscopy. The higher ^{31}P NMR resonance of 67.82 ppm than that in **43** indicates more reduced platinum center in **49**. In solution, however, the complex assumes a different form whose structure is not yet known. This form is

characterized by a ^{31}P NMR resonance at 9.36 ppm in dichloromethane solution, while the magnitude of the $^{1}J_{Pt-P}$ is 1997Hz.

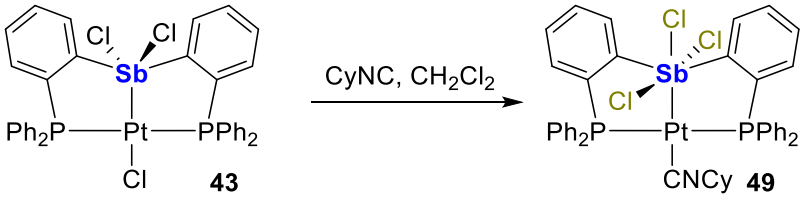

Figure 50. Synthesis of **49**

The structure of **49** confirms migration of a chloride ligand from platinum to antimony, leading to formation of a trichlorodiarylstiborane unit (Figure 51). This unit acts as a Z-ligand which becomes engaged in a Pt→Sb interaction of 2.6006(5) Å. The Pt–Sb bond is significantly longer than that in **43** (2.4407(5) Å), in agreement with a change from a covalent Pt–Sb linkage in **43** to a Pt→Sb dative interaction in **49**. The isocyanides ligand is coordinated trans from the antimony center as indicated by the C(14)–Pt–Sb angle of 179.73(11)°. This angle along with P1–Pt–P2 angle of 171.73(3) indicate that the platinum atom adopts a square planar structure. The antimony center adopts a distorted octahedral geometry, as shown by Cl3–Sb–Pt, Cl1–Sb–Cl2 and C10–Sb1–C1 angles close to linearity. It is interesting to note that the bond distance of 2.6464(10) Å separating the antimony atom and the chlorine atom (Cl(3)) trans from the platinum atom is longer than the Sb–Cl bond distances involving the chlorine atoms trans from each other (Sb–Cl(2) = 2.4673(10) Å, Sb–Cl(4) = 2.4868(10) Å). These features document the high metallobasicity of the platinum atom and the trans–influence it exerts on the antimony center.

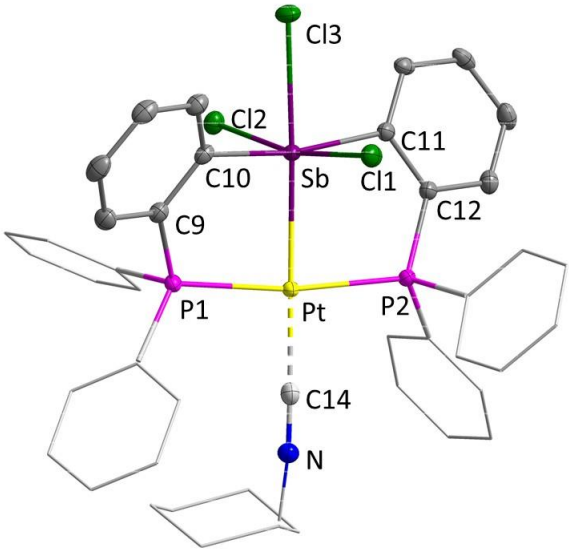

Figure 51. Solid-state structure of **49.** Thermal ellipsoids are drawn at the 50% probability level. Phenyl groups are drawn in wireframe. Hydrogen atoms and solvent molecules are omitted for clarity.

3.3 Synthesis of bis(triflate)stiboranyl platinum complex

Realizing that the halide migration reaction in Figure 49 connecting **C** to **D** would be facilitated by a highly electrophilic antimony center, I decided to investigate a complex of type **C** in which the Lewis acidity of the antimony atom is enhanced through the use of labile anionic substituents. Based on the knowledge that species such as $Ph_3Sb(OTf)_2$ possess unique Lewis acidic properties, the bis(triflate)antimony complex **50** was targeted (Figure 52). [61,63,72,185] This complex could be easily obtained by reaction of the known complex **43** with 2 equivalents of AgOTf in CH_2Cl_2. Complex **50** was characterized by ^{31}P NMR spectroscopy, which showed a resonance at 48.1 ppm with ^{195}Pt satellites ($^1J_{Pt-P}$ =2396 Hz). When compared to **43** which features a ^{31}P NMR resonance at 50.9 ppm

coupled to the ^{195}Pt nucleus by 2566 Hz, the $^{1}J_{Pt-P}$ coupling constant of **50** is notably reduced which is consistent with a depletion of electron density at the platinum center.[141]

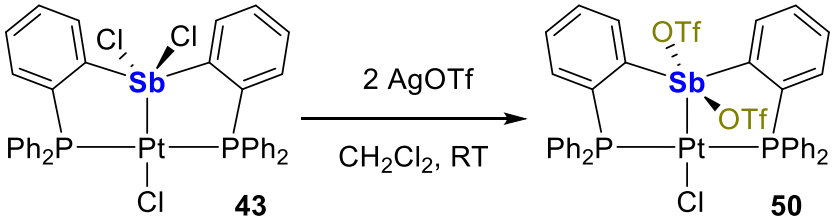

Figure 52. Synthesis of complex **50.**

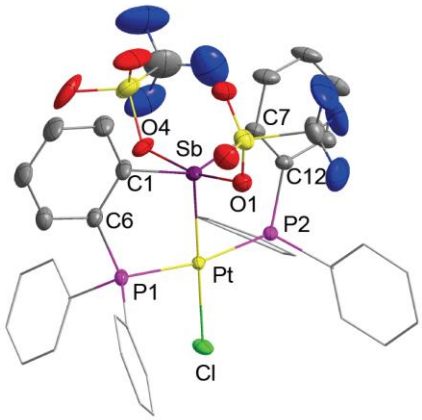

Figure 53. Structure of **50** in the crystal. Thermal ellipsoids are drawn at the 50% probability level. Phenyl groups are drawn in wireframe. Hydrogen atoms and solvent molecules are omitted for clarity. Relevant metrical parameters can be found in the text.

Single crystals suitable for X-ray diffraction analysis were obtained by pentane diffusion into a CH_2Cl_2 solution of complex **50**. The crystal structure confirms the coordination of two triflate anions to the antimony center. The Sb–Pt distance is shorter (2.4204(4) Å) than that in complex **43** (2.4407 (5) Å) indicating a contraction of the Pt–

Sb core triggered by electron depletion. The platinum atom displays a square-planar geometry as indicated by the value of P1–Pt–P2 (170.15(4)^{o}) and Cl–Pt–Sb (176.62(3)^{o}) angles. As for the antimony atom, it adopts a distorted trigonal bipyramidal geometry in which the two triflate anions sit at the axial positions, as indicated by the O1–Sb–O4 angle of 168.42(11)^{o}. The equatorial positions are occupied by the platinum center and the two phenylene groups whose antimony-bound carbon atoms form an angle (146.53(16)^{o}) notably larger than the ideal value of 120^{o}. It remains that the two antimony-bound carbon atoms and the platinum atom lie in the same plane as indicated by the sum of the C1–Sb–Pt, C7–Sb–Pt and C1–Sb–C7 angles of 359.14^{o}. The Sb1–O1 (2.189(3) Å) and Sb1–O4 (2.219(3) Å) distances involving the triflate anions are, on average, very close to those in $Ph_3Sb(OTf)_2$ (2.172 Å).[61] In turn, complex **50** can be viewed as an analog of $Ph_3Sb(OTf)_2$ where one of the phenyl group has been replaced by a divalent platinum moiety (Figure 53).

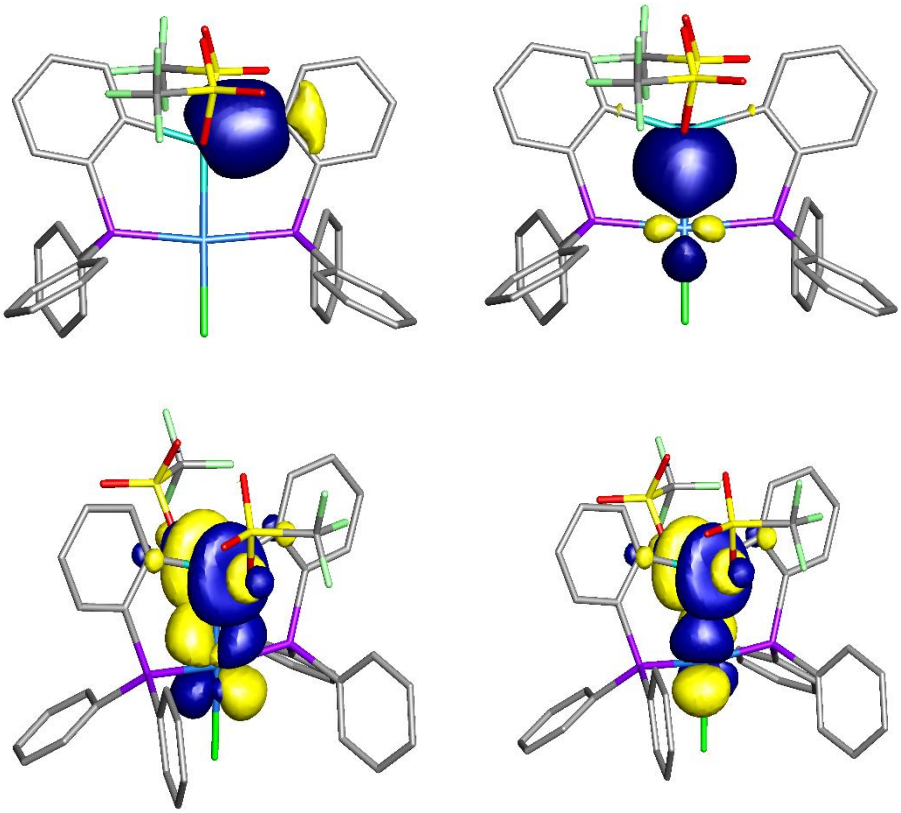

Figure 54. NLMO (top) and NBO (bottom) plots (isovalue = 0.05) of the C–Sb and Sb−Pt bonds in **50**. Hydrogen atoms are omitted for clarity.

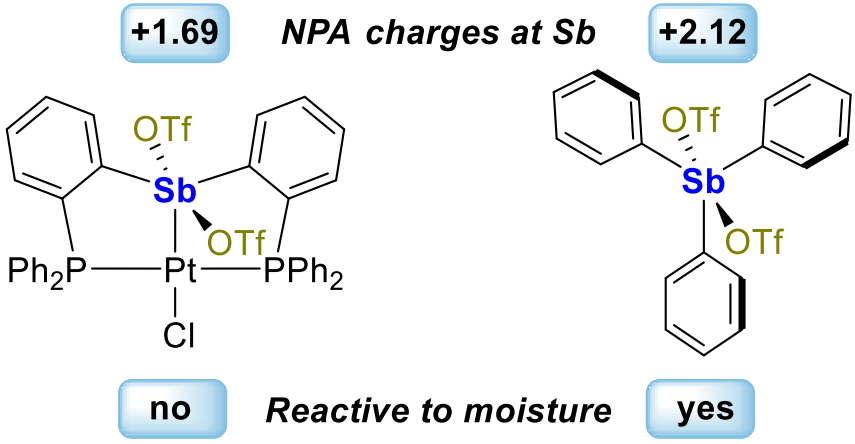

Figure 55. Illustration underscoring the structural similarity of **50** (left) and $Ph_3Sb(OTf)_2$ (right).

This analogy seems to be limited to a structural one, as the air stability of **50** greatly exceeds that of $Ph_3Sb(OTf)_2$. Indeed, while $Ph_3Sb(OTf)_2$ quickly hydrolyzes in air,[185] compound **50** can be handled and crystallized on the bench top, without specific precautions. It can also be stored in air for several days without decomposition. To identify the origin of this unusual stability, the structure of **50** and $Ph_3Sb(OTf)_2$ was optimized computationally using DFT methods (Gaussian program, functional BP86; mixed basis set Sb/Pt cc-pVTZ-pp; P/S/Cl 6-31g(d'); F 6-31+g(d'); C/O/H 6-31g) and subsequently analyzed using the Natural Bond Orbital (NBO) method (Figure 54). Examination of the Natural Localized Molecular Orbitals (NLMO) shows that the C_{Ar}–Sb σ-bonds in both compounds are polarized toward the phenyl ipso aryl carbon atom (av. orbital contribution: 60.8% C_{Ar}/36.7% Sb in **50**, 59.1% C_{Ar}/ 38.4% Sb in $Ph_3Sb(OTf)_2$). However, compound **50** possesses a Pt–Sb σ-bond that is polarized toward antimony (44.4% Pt/ 49.3% Sb) showing that the platinum metalloligand is more electron-releasing than a phenyl ligand. As a result, when compared to $Ph_3Sb(OTf)_2$, the antimony center of **50** is more electron rich. π-back-bonding interactions involving donation from Pt(5d) orbitals into the Sb(5p) orbital oriented toward the triflate anions may also be viewed as a possible contributor to this increase in electron density as suggested by an inspection of the relevant NBOs (Figure 54). I propose that these electronic effects attenuate the electron deficiency of the antimony(V) center and contribute to its unexpected stability. This conclusion is supported by the fact that the Natural Population Analysis (NPA) charge at the antimony center of **50** (1.69) is lower than that of $Ph_3Sb(OTf)_2$ (2.12) (Figure 55).

3.4 Chloride migration mechanism

Given the above, I became eager to verify if the halide migration process pictured in Chart 1 would be possible. To this end, complex **50** was treated with CyNC, which I chose as a surrogate for a possible reaction substrate (Figure 56). This reaction proceeded swiftly in CH_2Cl_2 to produce a new species characterized by a ^{31}P NMR resonance at 46.1 ppm with ^{195}Pt satellites ($^1J_{Pt-P}$ =2273 Hz).

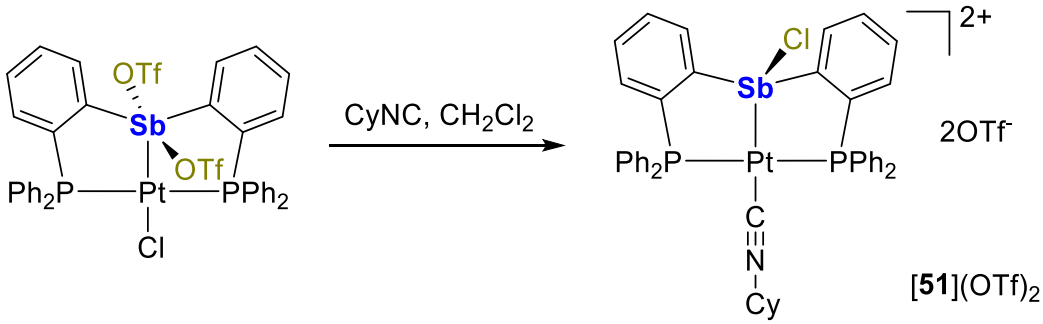

Figure 56. Synthesis of complex [**51**](OTf)$_2$.

This new compound was obtained in a crystalline form through pentane diffusion into a dichloromethane solution. Determination of the structure of this complex revealed the surprising formation of the dicationic complex [**51**]$^{2+}$ (Figure 57). Formation of this cation can be viewed as resulting from coordination of the isocyanide ligand to the platinum center concomitant with migration of the chloride anion to antimony and decoordination of the two triflate anions. The isocyanide ligand in [**51**]$^{2+}$ is positioned trans from the antimony center as indicated by the C19–Pt–Sb angle of 176.4(2)°. This chloride transfer process is accompanied by a lengthening of the Pt–Sb bond from 2.4204(4) Å in **50** to 2.4805(11) Å in [**51**]$^{2+}$. The Sb–Cl bond of 2.326(2) Å in [**51**]$^{2+}$ is noticeably shortened compared to those in **49** (2.494(3) Å (av.)), consistent with the

dicationic and thus more Lewis acidic nature of the bimetallic core. One of the two triflates counter anions approaches the antimony center trans from the chlorine atom (O1–Sb–Cl1 = 172.43(13)°), forming a long Sb–O1 interaction of 2.565(5) Å. The four primary ligands bound to antimony form a distorted tetrahedral geometry suggesting that the antimony ligand acts as an L-type stibine ligand toward the platinum center.

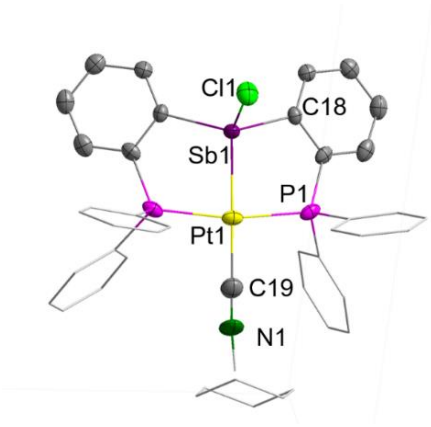

Figure 57. Structure of [**51**]OTf_2 in the crystal. Thermal ellipsoids are drawn at the 50% probability level. Phenyl groups are drawn in wireframe. The hydrogen atoms and the triflate anions are omitted for clarity. Relevant metrical parameters can be found in the text or the SI. Right: NLMO and NBO plots (isovalue = 0.05) of the C–Sb and Sb−Pt bonds in [**51**]$^{2+}$. Hydrogen atoms are omitted for clarity.

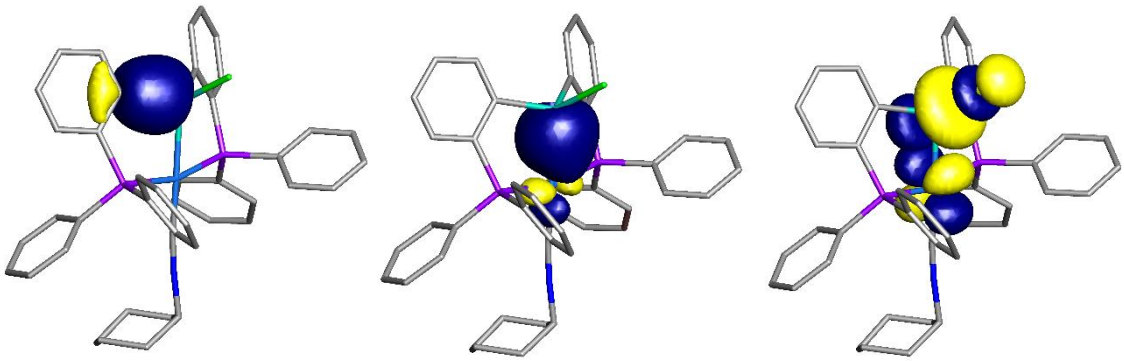

Figure 58. NLMO (left) and NBO (right) plots (isovalue = 0.05) of the C–Sb covalent and Sb−Pt dative bonds in [**51**]$^{2+}$. Hydrogen atoms are omitted for clarity.

However, the long contact formed by the triflate anion serves as a reminder that the antimony ligand is Lewis acidic. DFT calculations on [**51**]$^{2+}$ and NBO analysis support the acidic nature of the antimony atom which again acts as a π acceptor of d-electron density from the platinum center through Pt(5d)→Sb(5p) π interactions while the C–Sb and Pt–Sb σ-bond retain a polarization analogous to that in **50** (C–Sb: 61.2% C/ 36.4% Sb; Pt–Sb: 46.5% Pt/ 49.6% Sb) (Figure 58). The P–Sb π interaction in [**51**]$^{2+}$ evokes some of the unique features of cationic phosphine and arsine platinum complexes such as **E** and **F** (Figure 59)[186,187] in which the strong π-accepting character of the cationic ligands render the platinum uniquely active in reactions that proceed through the carbophilic activation of alkynes.[126]

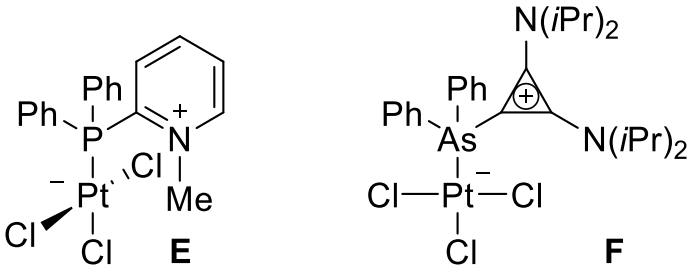

Figure 59. Examples of cationic phosphine and arsine complexes used as pre-catalysts in alkyne activation reactions.

The possibility of accessing a structure such as that of [**51**]$^{2+}$ by simple addition of a basic substrate to **50** prompted us to investigate the catalytic activity of the latter. In particular, I became eager to determine if the electron deficient platinum center would be sufficiently electrophilic to participate in the carbophilic activation of alkynes,[188,189] a reactivity that has been observed for related gold–boron and gold–antimony

complexes.[125,152] Gratifyingly, I observed that **50** serves as a self-activating catalyst for the cyclization of enyne **a**[167] as well as for the intramolecular hydroarylation reaction of the propargyl aryl ether **b**,[126] two model reactions that I chose for the purpose of this study (Figure 60). These reactions proceeded smoothly at room temperature over the course of 3-4 hours to complete conversion when catalyst **50** was used in 5 mol% ratio, without an external chloride anion abstracting agent. For the two reactions investigated, catalyst **50** operates under much milder conditions than $PtCl_2$ which requires heating in toluene.[167,190] It is also important to point out that catalyst **50** shows no sign of decomposition in the the enyne cyclisation of **a** and can be detected by ^{31}P NMR spectroscopy, even at the end of the reaction.

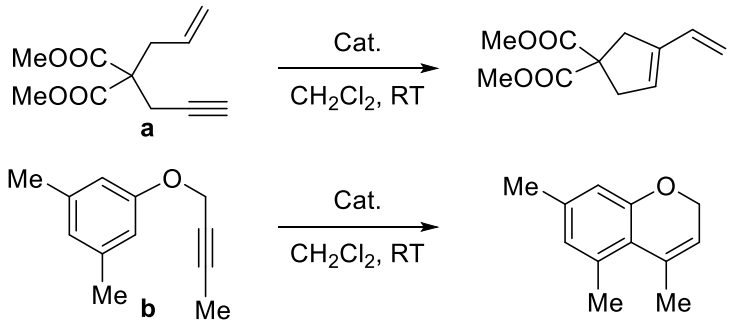

Figure 60. Reactions catalyzed by **50.**

I propose that the activity of **50** in these reactions originates from the intramolecular migration of the chloride ligand to antimony generating an unmasked and catalytically active platinum center (Figure 61). Complex **43**, [**51**]OTf_2 and $Ph_3Sb(OTf)_2$ show no activity in these reactions. The lack of activity observed for **43** and [**51**]OTf_2 indicate that the Lewis acidity of the antimony center in **43** is not sufficient to induce an

activation of the platinum center by halide migration while the presence of the isocyanide ligand in [**51**]$^{2+}$ effectively poison the active platinum center. The absence of activity observed for $Ph_3Sb(OTf)_2$ supports the notion that catalysis takes place at the platinum center rather than at the antimony center.

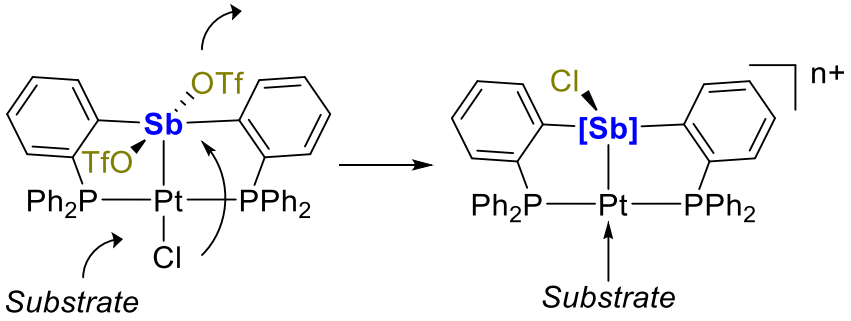

Figure 61. Proposed working model for substrate activation.

3.5 Conclusion

In conclusion, I describe an air stable platinum compound which converts into an active electrophilic catalyst in the presence of the substrate. While typical electrophilic platinum catalysts such as **E** and **F** necessitate activation using a silver salt, complex **50** spontaneously turns on, without addition of any activator. Activation is proposed to occur via the intramolecular migration of a platinum-bound chloride ligand to an adjacent Lewis acidic antimony center. This conclusion is supported by the observed activity of complex **50** in reactions involving the carbophilic activation of alkynes. It is also supported by the isolation of the dicationic complex [**51**]$^{2+}$ in which the isocyanide ligand plays the role of a substrate surrogate. These results demonstrate that the coordination non-innocence and

Lewis acidity of antimony ligands can be exploited for the purpose of electrophilic catalysis.

3.6 Experimental

General experimental considerations: [(*o*–$(Ph_2P)C_6H_4)_2SbCl$], *cis*–$PtCl_2(Et_2S)_2$ were prepared according to the reported procedures. All air and moisture sensitive experiments were carried out under an atmosphere of dry N_2 employing either a glove box or standard Schlenk techniques. Solvents were dried by passing through an alumina column (*n* ‑ pentane and CH_2Cl_2) or by reflux under N_2 over Na/K (Et_2O). All other solvents were used as received. Commercially available chemicals were purchased and used as provided (Commercial sources: Aldrich for $SbCl_3$; Matrix scientific for AgOTf. Ambient temperature NMR spectra were recorded on a Varian Unity Inova 500 FT NMR (499.42 MHz for ^1H,125.58 MHz for ^{13}C, 469.89 MHz for ^{19}F, 202.16 MHz for ^{31}P). ^1H and ^{13}C NMR chemical shifts are given in ppm and are referenced against $SiMe_4$ using residual solvent signals used as secondary standards. ^{19}F NMR chemical shifts are given in ppm and are referenced against $CFCl_3$ using BF_3–Et_2O as an external secondary standard with δ -153.0 ppm. ^{31}P NMR chemical shifts are given in ppm and are referenced against H_3PO_4 as an external standard. Elemental analyses (EA) were performed at Atlantic Microlab (Norcross, GA).

Computational Details: Density functional theory (DFT) structural optimizations were performed on the solid state structures of complexes **43**,**49**, **50**, [**51**]$^{2+}$ using Gaussian 09 suite of programs with effective core potentials on all heavy atoms (functional: BP86;

mixed basis set: Sb/Pt: cc-pVTZ-PP; P/S/Cl: 6-31g(d); H/C/O: 6-31g, F: 6-31+g(d'). Frequency calculations were used to confirm convergence of the calculations. The optimized structures, which are in excellent agreement with the solid-state structures, were subjected to a NBO analysis and were visualized and plotted using the Jimp 2 program.[170]

Crystallographic Measurements: The crystallographic measurements were performed at 110(2) K using a Bruker APEX – II CCD area detector diffractometer (Mo-Kα radiation, κ = 0.71069 A). In each case, a specimen of suitable size and quality was selected and mounted onto a nylon loop. The structures were solved by direct methods, which successfully located most of the non-hydrogen atoms. Semi-empirical absorption corrections were applied. Subsequent refinement on F_2 using the SHELXTL/PC package (version 6.1) allowed location of the remaining non-hydrogen atom. Disordered interstitial solvents in the structure of **50** and [**51**](OTf)$_2$ were dealt with using the SQUEEZE subroutine as implemented in Platon.

Synthesis of 50: A CH_2Cl_2 solution (2 mL) of complex **43** (240 mg, 0.25mmol) was slowly added to a CH_2Cl_2 solution (5mL) of AgOTf (130mg, 0.50 mmol) at ambient temperature. After 1 h, the solution was filtered, and the product was precipitated with pentane (5 mL). This precipitate was isolated by filtration, washed with pentane (3 × 5 mL) and dried under vacuum, affording compound **50** as a white, air stable solid 86% yield (256 mg). Crystals of **50** (containing disordered interstitial solvents) suitable for X-ray diffraction were obtained by slow diffusion of pentane into a concentrated CH_2Cl_2 solution of **50** at room temperature. ^{1}H NMR (499.42 MHz; $CDCl_3$): δ 7.45 (t, 8 H, $^3J_{H–H}$ = 7.43 Hz), 7.52 (t, 4 H, $^3J_{H–H}$ = 7.22 Hz), 7.58–7.62 (m, 8 H), 7.69 (m, 4 H), 7.88 (m, 2

H, *o*–P(Sb)C_6H_4), 8.85 (d, 2 H, *o*–P(Sb)C_6H_4, $^3J_{H–H}$ = 7.81 Hz). $^{13}C\{1H\}$ NMR (125.58 MHz; $CDCl_3$): δ 127.4 (q, –C_6H_5, $J_{C–P}$ = 30.9 Hz), 129.0 (t, –C_6H_5, $J_{C–P}$ = 5.9 Hz), 132.0(s), 133.1(s), 133.8 (t, –C_6H_5, $J_{C–P}$ = 6.6 Hz), 134.1(s), 135.3(brs), 135.7(s). $^{31}P\{^1H\}$ NMR (202.16 MHz; $CDCl_3$): δ 48.41 (t, $J_{Pt–P}$ = 2396 Hz). Anal. Calcd for 2: C, 38.91; H, 2.41. Found: C, 39.15; H, 2.54.

Synthesis of [51]OTf_2: One equivalent of cyclohexyl isocyanide (CNCy) was slowly added to a CH_2Cl_2 solution (2 mL) of **50** (38 mg, 0.03 mmol) at ambient temperature. After 30 min, pentane was added to the reaction mixture, leading to formation of a precipitate. This precipitate was isolated by filtration, washed with pentane (3 × 5 mL) and dried under vacuum, affording compound [**51**]OTf_2 as a pale yellow, air stable solid 65% yield (27 mg). Crystals of [**51**]OTf_2 (containing disordered interstitial solvents) suitable for X-ray diffraction were obtained by slow diffusion of pentane into a concentrated CH_2Cl_2 solution of [**51**]OTf_2 at room temperature. ^1H NMR (499.42 MHz; $CDCl_3$): δ 0.85-1.05 (br, 5H), 1.07-1.20 (br, 3H), 1.21-1.33 (br, 1H), 1.43-1.55 (br, 2H), 7.46-7.63 (m, 18H), 7.66 (t, 4 H, $^3J_{H–H}$ = 7.5 Hz), 7.74 (t, 2H, $^3J_{H–H}$ = 7.6 Hz), 7.94 (t, 2H, $^3J_{H–H}$ = 7.8 Hz, *o*–P(Sb)C6H4), 8.50 (d, 2H, *o*–P(Sb)C_6H_4, $^3J_{H–H}$ = 7.8 Hz). $^{13}C\{^1H\}$ NMR (100.45 MHz, $CDCl_3$): δ 22.20 (s, Cy–*C*H2), 24.50 (s, Cy–*C*H2), 31.07 (s, Cy–*C*H2), 56.38 (s, Cy–*C*H), 116.24-123.88 (q, –CF3, $^1J_{C–F}$ = 320 Hz), 128.9 (t, –C6H5, $J_{C–P}$ = 5.5 Hz), 129.3 (t, –C_6H_5, $J_{C–P}$ = 5.1 Hz), 129.93 (s), 130.1 (s), 133.06 (m), 133.3 (s), 133.70 (s), 134.15 (m), 135.25 (s), 135.83 (s). $^{31}P\{1H\}$ NMR (202.16 MHz; $CDCl_3$): δ 46.4 (t, $J_{Pt–P}$ = 2273 Hz). Anal. Calcd for [**51**]OTf_2: C, 42.16; H, 3.07. Found: C, 41.96; H, 3.08.

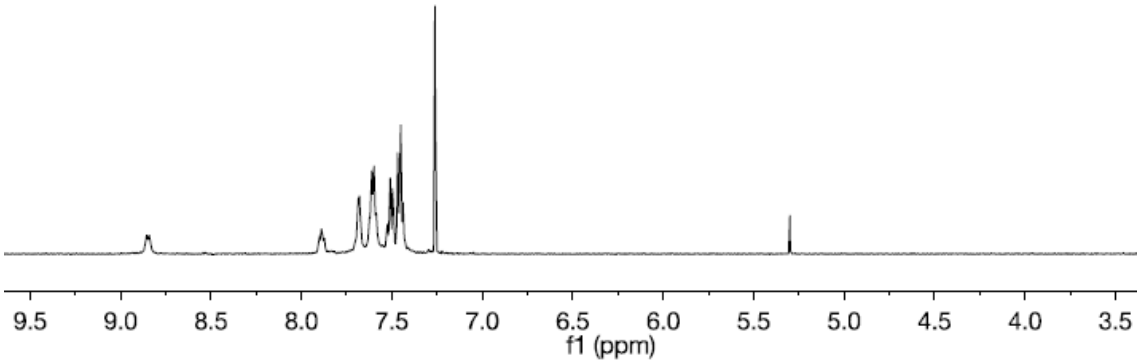

Figure 62. ^{1}H NMR spectrum of **50** in $CDCl_3$.

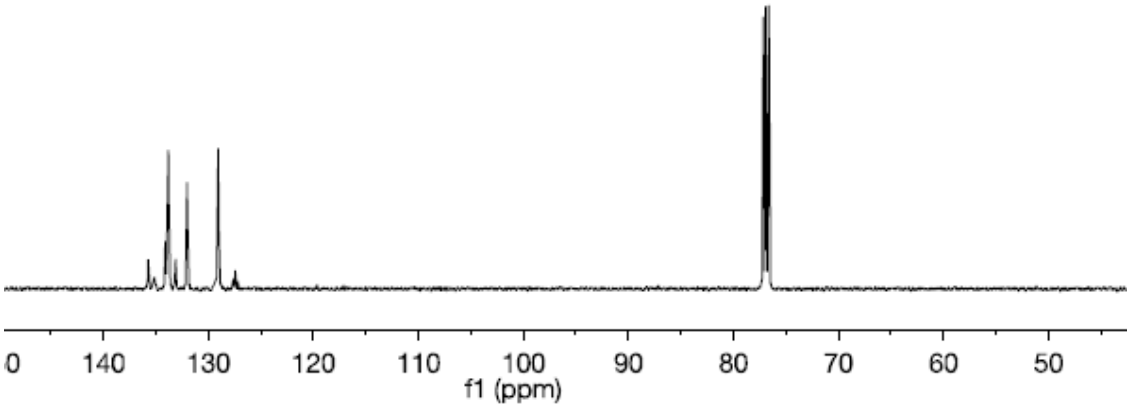

Figure 63. ^{13}C NMR spectrum of **50** in $CDCl_3$**.**

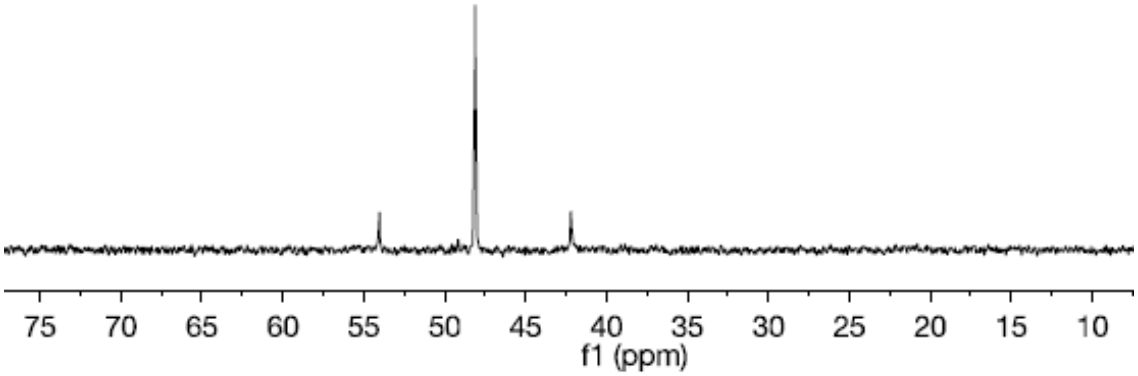

Figure 64. ^{13}P NMR spectrum of **50** in $CDCl_3$.

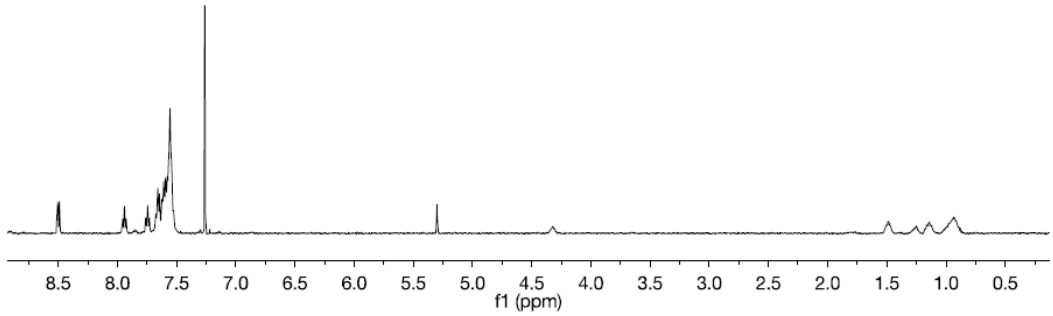

Figure 65. ^{1}H NMR spectrum of [**51**]OTf_2 in $CDCl_3$.

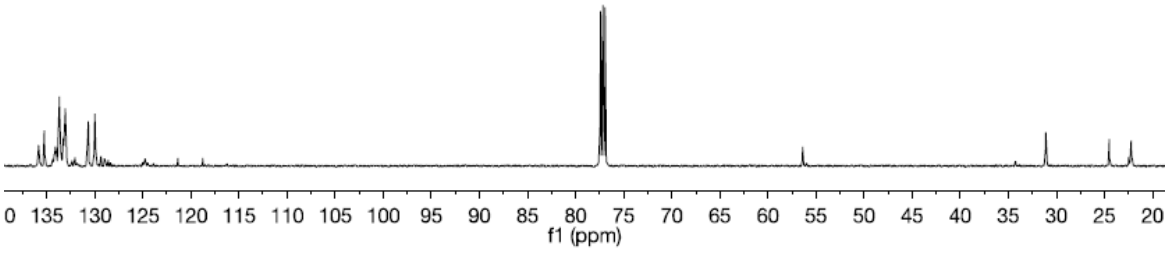

Figure 66. ^{13}C NMR spectrum of of [**51**]OTf_2 in $CDCl_3$.

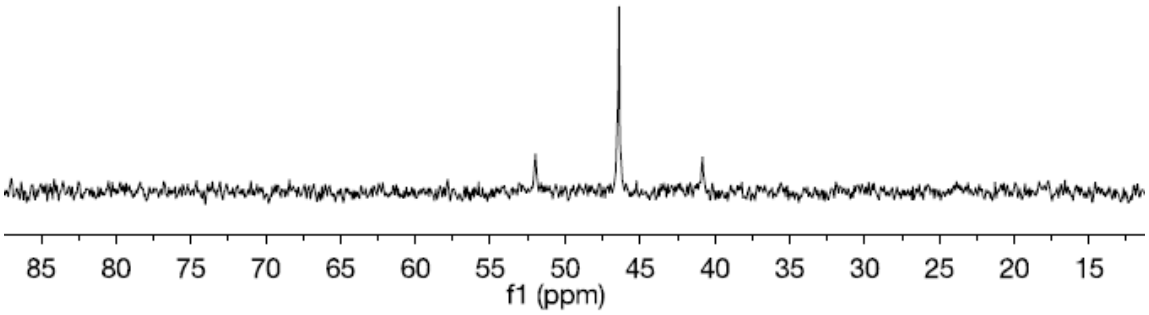

Figure 67. ^{31}P NMR spectrum of of [**51**]OTf_2 in $CDCl_3$.

General procedure for the catalytic cycloisomerization and hydroarylation reactions: Catalytic reactions were carried out under N_2. In a typical reaction, the alkyne-containing substrate (**a** or **b**) was mixed with 5 mol% complex **50** in CH_2Cl_2 or $CHCl_3$. Conversion was estimated using ^1H NMR spectroscopy with 1,2,4,5–tetramethylbenzene as internal standard. Amounts used in a typical experiment are provided hereafter.

Cycloisomerization of a:

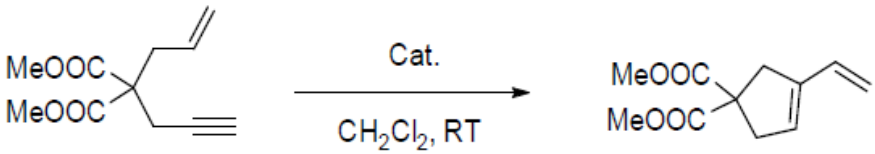

Loading: Dimethyl 2–allyl–2–(2–propynyl)malonate (146.1 mg, 0.69 mmol), catalyst (38.8 mg, 5 mol%). Conversion 96 %. Isolation: The product was isolated as a colorless oil via column chromatography. Isolated yield 88%.

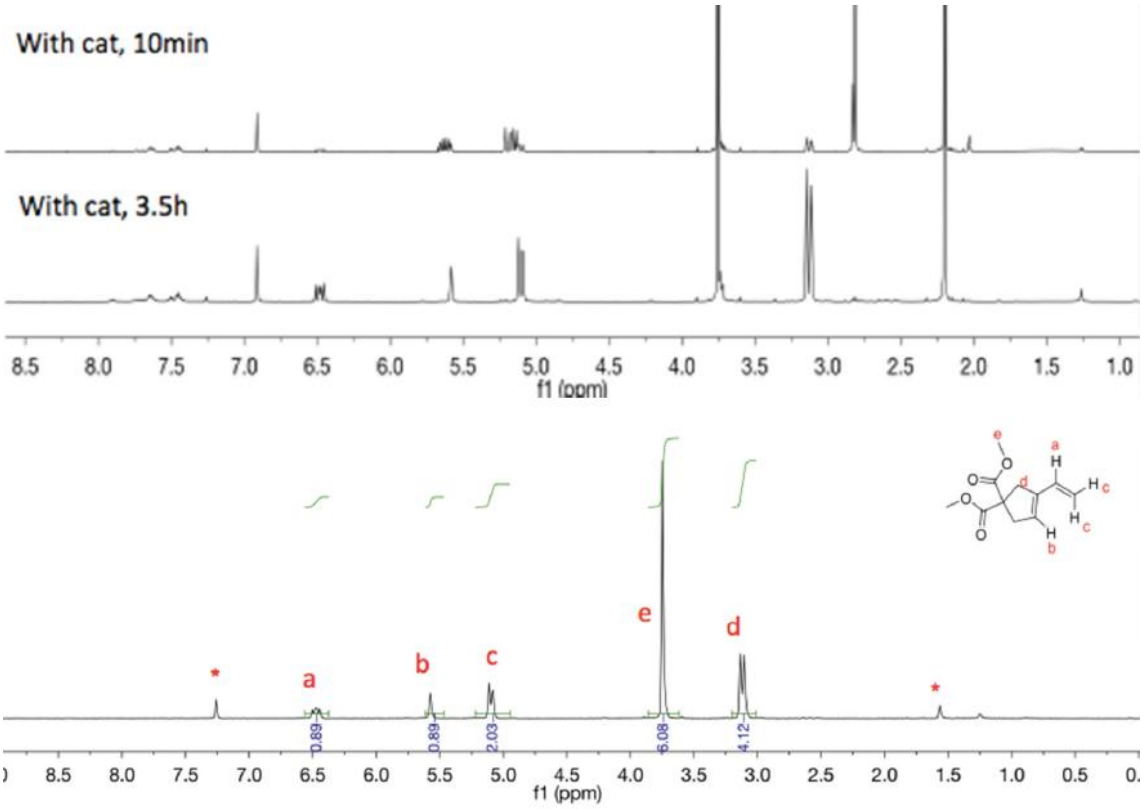

Figure 68. ^{1}H NMR spectra collected during the cycloisomerization reaction of substrate a (top) and upon completion of the reaction after product isolation/purification (bottom). $CDCl_3$ solvent residues (*) are marked on the spectrum.

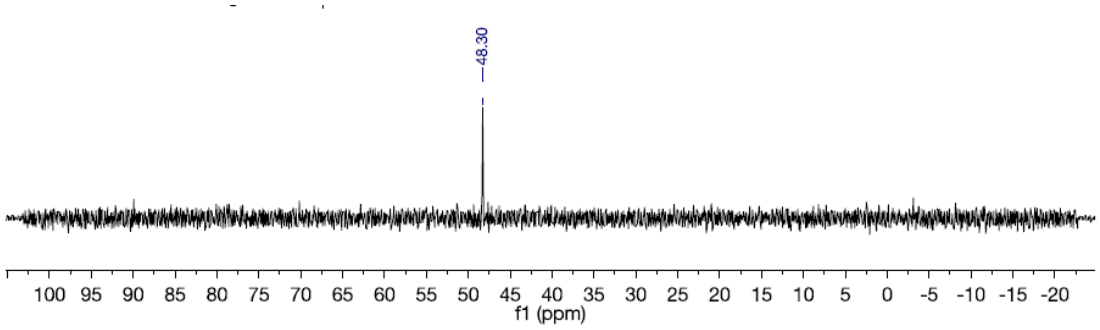

Figure 69. ^{31}P NMR spectra collected upon completion of the cycloisomerization reaction substrate **a**.

Hydroarylation of b:

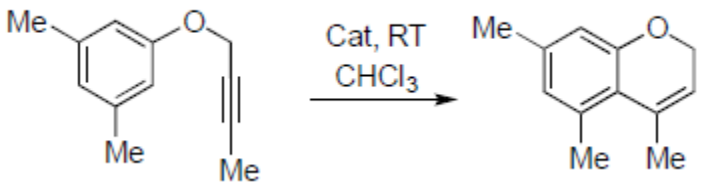

Loading: 1–(2–Butyn–1–yloxy)–3,5–dimethylbenzene (110.7 mg, 0.63 mmol), catalyst (37 mg, 5 mol%).

Conversion: 80% (46% conversion was achieved in the first 10 min). Formation of the product is accompanied by appearance of a side product in less than 5% yield; the identity of this product has not been established.

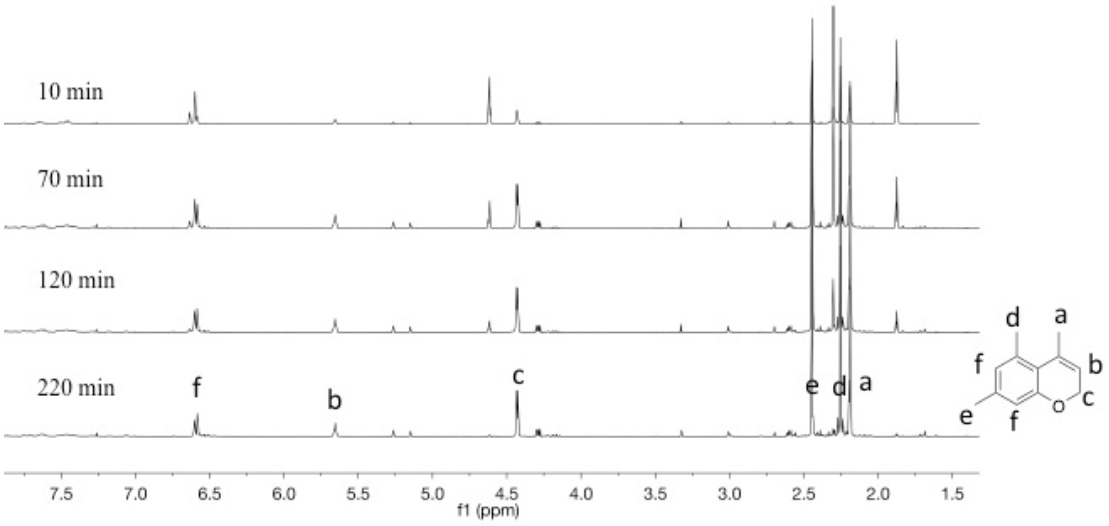

Figure 70. ^{1}H NMR spectra collected during the hydroarylation reaction of substrate **b**.

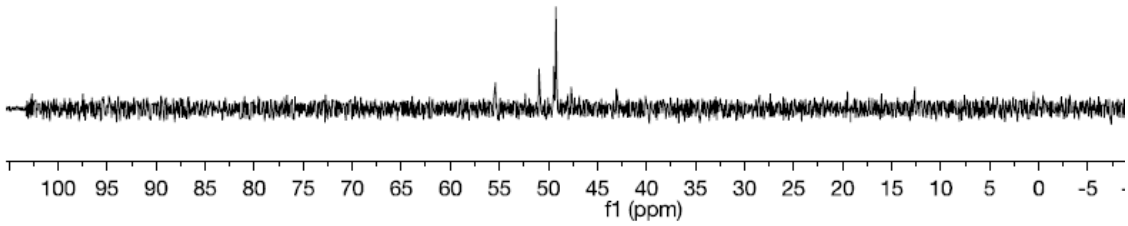

Figure 71. ^{31}P NMR spectra collected upon completion of the hydroarylation reaction of substrate **b**.

CHAPTER IV

ACTIVATION OF ANTIMONY–PLATINUM COMPLEX AS CARBOPHILIC CATALYST THROUGH PERIPHERAL LIGAND SUBSTITUTION

4.1 Introduction

Antimony(V) derivatives are powerful Lewis acids which have been used for the generation of super acids[40,191] or as catalysts for transformations that necessitate strong electrophilic activation.[192-194] While antimony(V) halides have been at the forefront of this chemistry for much of the past 6 decades, recent efforts have shown that organoantimony compounds can also display appealing Lewis acidic properties while also being more convenient to handle than their halide counterparts.[63,65,66,68,74,195-197] These advantageous properties of antimony have come to light in the development of applications in organic reaction catalysis[45,131,192,198-200] and anion sensing.[67,74,138,201] With the view of transferring the electrophilic qualities of antimony(V) compounds to transition metals, we have recently launched a synthetic effort toward the synthesis of complexes that combine a high-valent antimony center and a late transition metal.[125,202,203] Examples of such complexes include **G** and **H**, two compounds in which the high Lewis acidity of the antimony center defines the catalytic properties of the late transition metal center (Figure 72). In complexes of type **G** and **H**, we proposed that the σ-accepting properties of the antimony moiety served to activate the late transition metal center via formation of a M→Sb interaction, leading to an enhancement in the carbophilic reactivity of the metal center. In a separate investigation, we reported an antimony platinum complex (**50**) in

which the Lewis acidity of the stiboranyl moiety is accentuated by the presence of two triflate anion.[165] Despite the apparent coordinative saturation of the platinum center, we observed that this compound is a self-activating catalyst for enyne cyclization and hydroarylation reactions (Figure 60). We speculated that this complex owes its catalytic activity to the presence of a Lewis acidic antimony center which helps activate the Pt–Cl bond intramolecularly, allowing for substrate activation. With the view of further enhancing the properties of such platforms, we have now targeted an analog of **50** in which the chloride ligand bound to platinum is also replaced by a more weakly coordinating triflate anion. Given the lability of the triflate anions, we speculated that such a complex might generate an exposed platinum species, the reactivity of which would be further enhanced by the presence of an adjacent electrophilic antimony triflate unit.

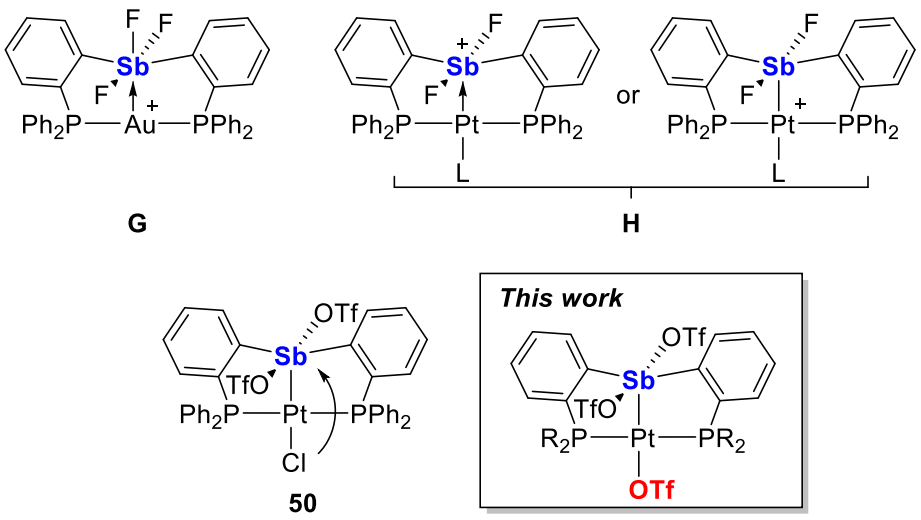

Figure 72. Lewis acidic behavior of antimony ligands.

4.2 Synthesis and structures of the Sb–Pt complexes

We have previously described [(*o*–(Ph_2P)C_6H_4)$_2$$SbCl_2$]PtCl (**43**), a complex with diphenylphosphino groups as anciallry ligands.[159] In this work, I decided to synthesize the di–*iso*–propylphosphino derivative [(*o*–($^iPr_2P$)C_6H_4)$_2$$SbCl_2$]PtCl. (**52**), with a view of testing how substitution of the phosphorus atom influences the chemistry of these complexes. Reaction of the previously reported chlorostibine (*o*–($^iPr_2P$)C_6H_4)$_2$SbCl ligand with $PtCl_2(SEt_2)_2$ in CH_2Cl_2 at reflux temperature under N_2 for 16 h afforded a yellow homogenous solution (Figure 73). The ^{31}P NMR spectrum of this solution shows a single resonance at 72.6 ppm, coupled to the ^{195}Pt nuclei by $^1J_{Pt–P}$ = 2473 Hz. These spectroscopic features provided initial confirmation for the formation of **52**.

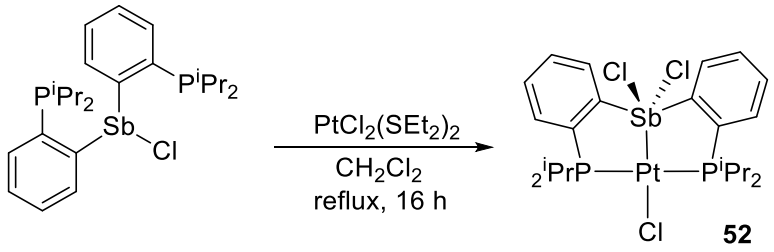

Figure 73. Synthesis of complex **52**.

Single crystals of **52** suitable for X-ray diffraction were obtained by vapor diffusion of pentane into a solution of the compound in CH_2Cl_2. The structure shows that the platinum center adopts square planer geometry (P1–Pt–P2: 170.70(2)^o; Cl3–Pt–Sb1 172.16(2)^o), with the antimony center being trigonal bipyramidal (Pt–Sb–Cl1: 99.57(3)^o; Pt–Sb–Cl2: 100.68(3)^o; C1–Sb–Pt: 106.20(8)^o; C13–Sb–Pt 105.67(8)^o) as in complex **43** (Figure 74). [159] The Sb–Pt separation of 2.4467(10) Å is almost identical to that found in **43** (2.4407(5) Å). The Pt–Cl3 distances found for **52** (Pt–Cl3: 2.376(1) Å) is a little longer

than that found for **43** (Pt–Cl3: 2.349(1) Å), which is likely due to the larger steric repulsion imposed by the *iso*–propyl ligands as well as by their more electron releasing properties.

A close look at the Sb–Pt bond in **52** with Natural Localized Molecular Orbital (NLMO) shows that like **43**, the Sb–Pt σ-bond is largely covalent. The orbital contributions from antimony and platinum are almost identical in both complexes (**43**: Sb, 48.79%; Pt, 45.39%; **52**: 48.58%; Pt, 45.60%). This result indicates that the R (R = Ph or ^{i}Pr) groups on the phosphino substituents has little impact on the Sb–Pt interaction.

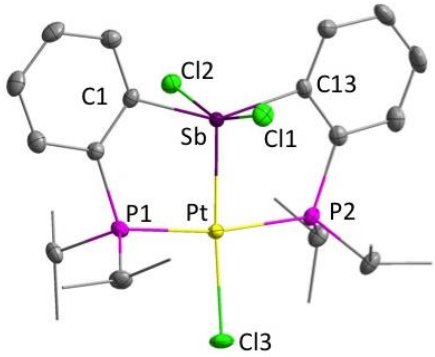

Figure 74. Solid-state structure **52** (right). Thermal ellipsoids are drawn at the 50% probability level. Methyl groups are drawn in wireframe. Hydrogen atoms are omitted for clarity.

While I anticipated that exchange of the platinum-bound chloride anion of **50** may be difficult, I observed that reaction of complex [(*o*–$(Ph_2P)C_6H_4)_2SbCl_2$]PtCl (**43**) with three equivalents of AgOTf proceeded smoothly to afford the target complex [(*o*–$(Ph_2P)C_6H_4)_2SbOTf_2$]PtOTf (**54**) (Figure 75). The same reaction was also carried out with [(*o*–($^{i}Pr_2P)C_6H_4)_2SbCl_2$]PtCl (**52**). Again, I observed facile substitution of the three chloride anions when 3 equivalents of AgOTf were employed, leading to the formation of

[(*o*–(^{i}Pr$_2$P)C$_6$H$_4$)$_2$SbOTf$_2$]PtOTf (**54**). The triflate derivatives **53** and **54** have been isolated as moisture sensitive solids. Their ^{31}P NMR spectra feature a single resonance at 49.4 ppm and 73.9 ppm coupled to the ^{195}Pt nuclei by $^{1}J_{Pt–P}$ = 2450 Hz and 2383 Hz, respectively. These values are close to those measured for **43** ($J_{Pt–P}$ = 2566 Hz) and **52** ($J_{Pt–P}$ = 2473 Hz). Despite several attempts, I failed to obtain single crystals of **54** and I therefore resorted to NMR spectroscopy as a means to confirm the full replacement of the three chloride ligands. To this end, I used pentafluoroacetophenone as a dual ^{1}H/^{19}F internal standard. Using the intensities of the ^{1}H and ^{19}F signals of pentafluoroacetophenone, I found a proton/fluoride ratio of 28/9 for **54**, in agreement with the presence of three triflate anions.

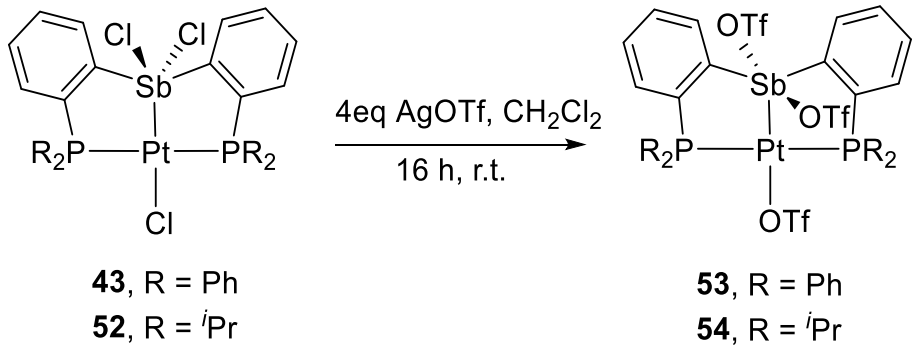

Figure 75. Synthesis of **53** and **54**.

Single crystals of **54** could be easily obtained by diffusion of pentane into a CH_2Cl_2 solution of **54**. An examination of the structure of this complex confirms the presence of three triflate anions bound to the dinuclear core of the complex. The Sb1–O1 (2.199(2) Å) and Sb1–O4 (2.211(2) Å) distances, which are comparable to those measured in complex

50, indicate that the triflate anions are tightly coordinated to the antimony atom. As in complex **50**, the antimony atom adopts a distorted trigonal bipyramidal geometry in which the two triflate anions occupy axial positions as indicated by the O1–Sb–O4 angle of 176.41(6)°. The largest distortion occurs in the equatorial plane where the C1–Sb–C7 angle of 143.52(10)° is notably larger than the ideal value of 120°. The Sb–Pt distance is shorter (2.4237(12) Å) than that in complex **52** (2.4467(10) Å) indicating a contraction of the Pt–Sb core triggered by electron depletion. Finally, the triflate anion bound to the platinum center is held by a Pt–O bond of 2.168(2) Å. This bond distance is comparable to that found in other platinum triflate complexes such as **I** (2.097(2) Å) and [**J**]$^{+}$ (2.102(9) Å) (Figure 76).[204,205]

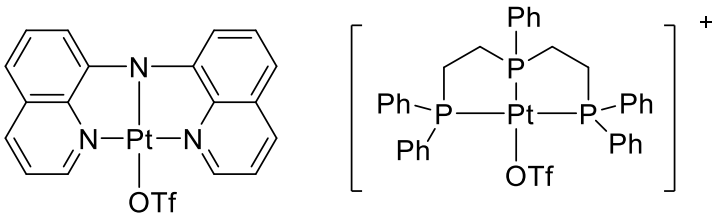

I [**J**]$^{+}$

Figure 76. Examples of complexes containing a Pt center stabilized by a triflate anion.

The structures of **53** and **54** have been studied computationally and some of their bonding features examined using the Natural Bond Orbital method (NBO). Examination of the NBO output indicates that the Sb–Pt bonds in **53** and **54** are covalent (Figure 77). Indeed, the corresponding Natural Localized Molecular Orbitals (NLMO) show that both the antimony and platinum atoms contribute equally to the bond that connects them (Sb,

48.85%, Pt, 45.01% for **53**; Sb, 49.11%, Pt, 44.64% for **54**). The lack of polarization of the Sb–Pt bond is a feature that these new complexes share with the trichloride precursors **43** and **52** as well as with complex **50**. Another relevant parameter to assess is the Natural Population Analysis (NPA) which reveals that the charge at the platinum atom (0.085 for **53** and 0.065 for **54**) is higher than those values found for **43** (-0.0135) and **52** (-0.0142).

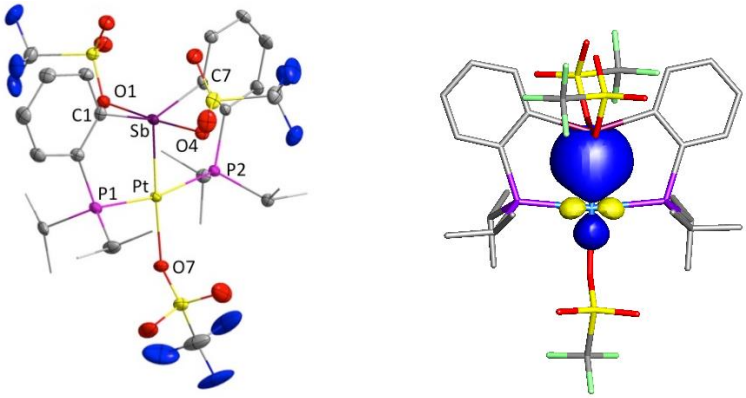

Figure 77. Left: Solid-state structure of **54**. Thermal ellipsoids are drawn at the 50% probability level. Methyl groups are drawn in wireframe. Hydrogen atoms are omitted for clarity. Right: NLMO plot of the major Sb–Pt bonding interactions.

4.3 Study of the catalytic reactivity

Given the known lability of the triflate ligand, we speculated that **53** and **54** might behave as electrophilic platinum catalysts.[126,206-210] To test this possibility, we became eager to investigate their use in the cycloisomerization of 2-allyl-2-(2-propynyl)malonate, reaction often used to benchmark the activity of late transition metal catalysts. Complex **53** proved to be remarkably active. Indeed, when used in a 5 mol% loading, the cycloisomerization reached completion within 10 min when carried out at room temperature (Table 3, entry 2). The same reaction took 3.5 hours to complete when **50** was

employed as a catalyst (Table 3, entry 1). The contrasting activity of these two catalysts underscores the benefit of substituting the platinum-bound chloride ligand of **43** with a more weakly coordinating triflate anion in **53**. I propose that the increased lability of the triflate anion increases accessibility of the platinum center by the reaction substrate, leading to more efficient catalyst.

Table 3. 1, 6–Enyne cyclization catalysis.

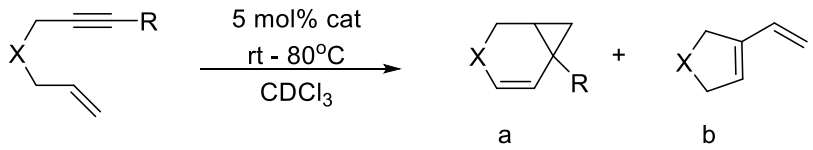

Entry	Cat	X	R	Time	Product	Conversion[b] (%)
1	**50**	$C(COOMe)_2$	H	3.5 h	**b**	96
2	**53**	$C(COOMe)_2$	H	10 min	**b**	96
3	**54**	$C(COOMe)_2$	H	3 h	**b**	0
4	**53**	NTs	H	1 h	**b**[a]	30
5	**53**	NTs	Me	1 h	**a**	58
6	**53**	NTs	Ph	1 h	**a**	47

[a] Trace amount of **a** (R = H) was observed

[b] Conversion determined by ^1H NMR

To our surprise, we found that **53** was inactive for this reaction. We examined the NPA charge of platinum centers in both complexes and found that this value is actually

lower in **54** (0.065) than in **53** (0.085). This lower charge suggests that the platinum center of **54** is less electrophilic, presumably because of the more electron releasing properties of the iso-propyl-substituted phosphino groups. The lack of reactivity for **54** may also originates from steric effect imposed by the bulkier iso-propyl groups, which lead to a less accessible platinum center. To support this argument, we inspected the steric maps of the ligands in both complexes as is shown in Figure 78. Comparison of the topographic steric maps identifies some important differences in the shapes of the catalytic pockets of the two complexes. Consistently, the %VBur (percent buried volume) at Pt in **54** (72.2%) is clearly larger than that in **53** (69.1%), suggesting greater accessibility in the latter. Such steric effects have been previously discussed in the case of the related gold anti-mony complexes $[((o\text{-}(^{i}Pr_2P)C_6H_4)_2(o\text{-}C_6Cl_4O_2)SbPh]Au]^+$ and $[((o\text{-}(Ph_2P)C_6H_4)_2(o\text{-}C_6Cl_4O_2)SbPh]Au]^+$.[157] Indeed while the former displayed no carbophilic reactivity, the latter readily promoted the cycloisomerization of *N*-(prop-2-yn-1-yl)benzamide or the addition reaction of *p*-toluidine to phenylacetylene. No further attempts to use **54** as a catalyst were considered.

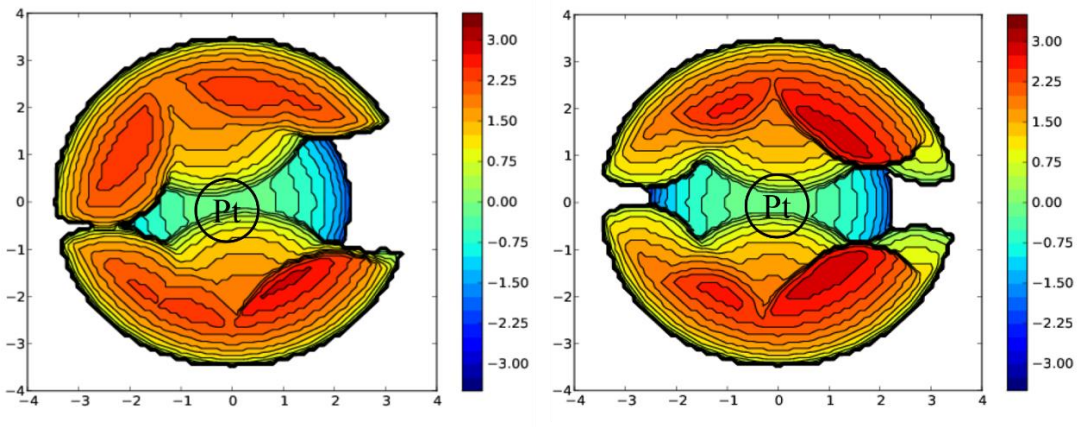

Figure 78. Topographic steric maps of the phosphino-antimony ligands in **53** (69.1%) and **54** (72.2%). The red and blue zones indicate the more- and less-hindered zones in the catalytic pocket, respectively**.**

Having shown that **53** is a much more reactive catalyst than **50**, I set out to investigate if it could catalyze more challenging reactions such as the cycloisomerization of nitrogen tethered 1,6–enynes. These reactions have been largely studied and applied to total synthesis.[167,211] The reactions were carried out at 80 ^{o}C with a 6 mol% catalyst loading for 1 h at which point the yield and product distribution were determined by ^{1}H NMR spectroscopy (Table 3, entry 4-5). I observed that high temperature leads to decomposition of catalyst **53** such that the reaction ceases to proceed. For this reason, all conversions are recorded exactly after 1 h. The platinum catalyzed cycloisomerization reaction in entry 4 (Table 3) mainly afforded product of type **b** with a 30 % conversion. Trace amount of the product of type **a** were however observed. Such a selectivity for the diene product of type B has been reported before when cis–Pt(TMP)$_2$Cl$_2$ (TMP: 1–phenyl–2,3,4,5–tetramethylphosphole) was used as a precatalyst and $AgBF_4$ as an activator in 1,2–dichloroethane. Entries 5 and 6 (Table 3) show that substitution of the alkyne by a methyl

or phenyl group changes the fate of the reaction, with the main product being that of type **a**. These results show that although complex **53** can catalyze cycloisomerisation reactions of *N*–tethered 1,6–enynes, the reactivity is largely limited due to the concomitant decomposition of the catalyst. For this reason, this reaction is not explored further.

I have also probed the reactivity of **53** towards intermolecular hydroarylation reactions involving alkynes and heteroaryls such as pyrrole. These reactions were carried out in $CDCl_3$ with a 5 mol% catalyst loading. The conversions of these reactions were analyzed by ^1H NMR spectroscopy. The results are summarized in Table 4. As anticipated from the reactivity pattern observed in the enyne cyclization reactions, complex **53** showed higher reactivity than **50** in these hydroarylation reactions. When pyrrole was reacted with phenylene in the presence of catalyst **53** (5 mol%), rapid conversion was observed, leading to the formation of the double-addition product in 89 % in just 10 min (Table 4, entry 2) In comparison, catalyst **50** was much less active and necessitated 12 h to reach of 68 % yield of the double addition product(Table 4, entry 1). The reaction of simple indole with phenylacetylene in the presence of catalyst **53** also proceeded to give the bisindole complex, with 71% conversion in 2 h (Figure 79).

Finally, in order to benchmark the activity of **53** against challenging substrates, we have also tested reactions involving thiophene as the heteroaryl. Thiophenes are among one of the most difficult class of substrates to activate as the free electron pair at sulfur can coordinate to the platinum center.[212,213] Because no reaction was observed with phenylacetylene, we decided to use ethyl propiolate, which owing to its greater electron deficiency, shows a higher reactivity. In line with the activity observed in the

aforementioned reactions, complex **53** displayed a much higher activity than **50**. Both catalysts afforded the mono-addition product **7** which was isolated in 87 % yield after 16 h when **53** was employed (Table 4, entry 4). The same reaction with **50** afforded less than a 10% conversion after 19 h (Table 4, entry 3). Interestingly, when the more electron rich 2-methylthiophene was used as the heteroaryl, the double addition product was formed (Table 4, entry 5 and 6). This difference highlights the greater electron-richness and reactivity of 2-methylthiophene as a nucleophile.

Table 4. Hydroarylation of alkynes with pyrrole and thiophene catalysis.

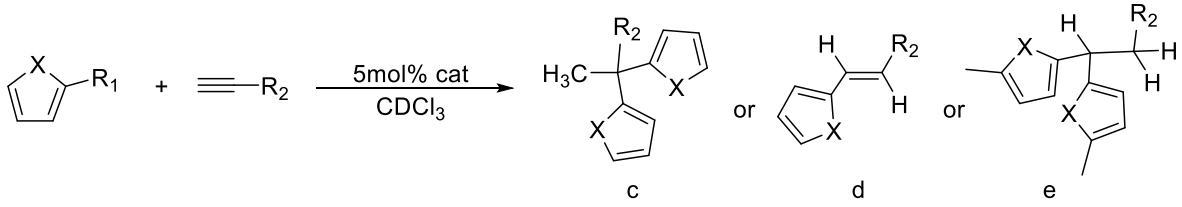

Entry	Cat	X	R_1/R_2	Time	Product	Conversion [a] (%)
1	**50**	NH	H/Ph	12 h	c	68
2	**53**	NH	H/Ph	10 min	c	89
3	**50**	S	H/COOEt	19 h	d	< 10
4	**53**	S	H/COOEt	16 h	d	87
5	**50**	S	Me/COOEt	7 h	e	19
6	**53**	S	Me/COOEt	7 h	e	76

a. Conversion determined by ^{1}H NMR with durene as internal standard.

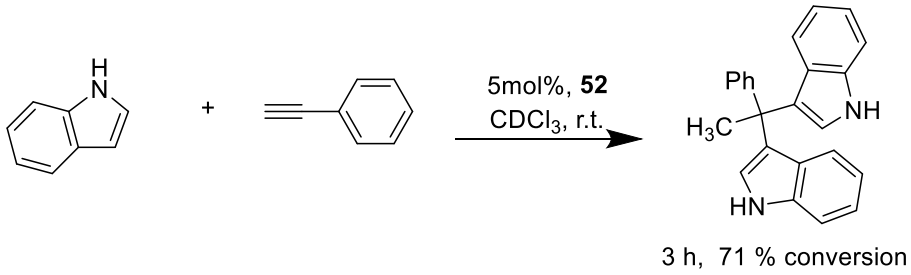

Figure 79. Hydroarylation of alkynes with indole catalysis.

4.4 Carboxylic acids as additives

Srobona Sen, a previous group member, synthesized complex **55** by treatment of the trifluorostiborane–platinum complex **44** with excess trifluoroacetic acid (Figure 80).[214] The structure shows three trifluoroacetate anions coordinated to the SbPt core, a feature reminiscent of the structure of the tristriflate complex **53**. Despite this structural similarity, complex **55** is not catalytically active in enyne cyclization reactions. This lack of reactivity is presumably due to the strong coordination nature of the trifluoroacetate anions. Nevertheless, this structure demonstrates the possibility of replacing a weekly coordinating anion such as triflate by a more coordinating carboxylate. I anticipated that addition of one equivalent of a weak acid such as a carboxylic acid to complex **53** should lead to the displacement of a triflate ligand and coordination of the carboxylate as is shown in Figure 81. Such reactions should be favored since carboxylates (pKa(RCOOH) = 12.3 (R = Me), 11.1 (R = Ph) in DMSO) are more basic than trifalte (pKa(HOTf) = 0.3 in DMSO). It occurred to us that the use of chiral carboxylic acids may afford asymmetric catalysts.

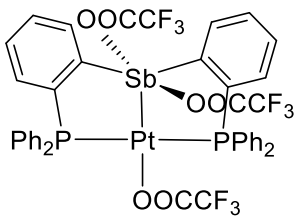

Figure 80. Chemical structure of complex **55.**

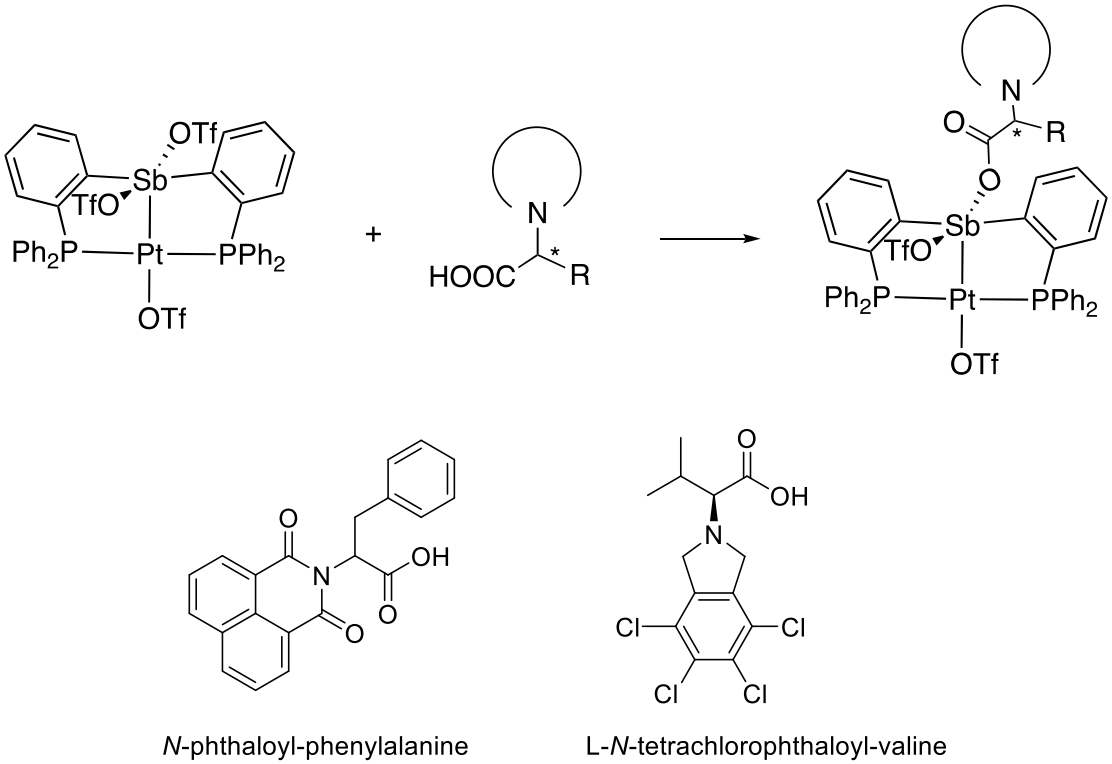

Figure 81. Top: Hypothesized reaction of **53** with carboxylic acid. Bottom: chemical structures of carboxylic acids.

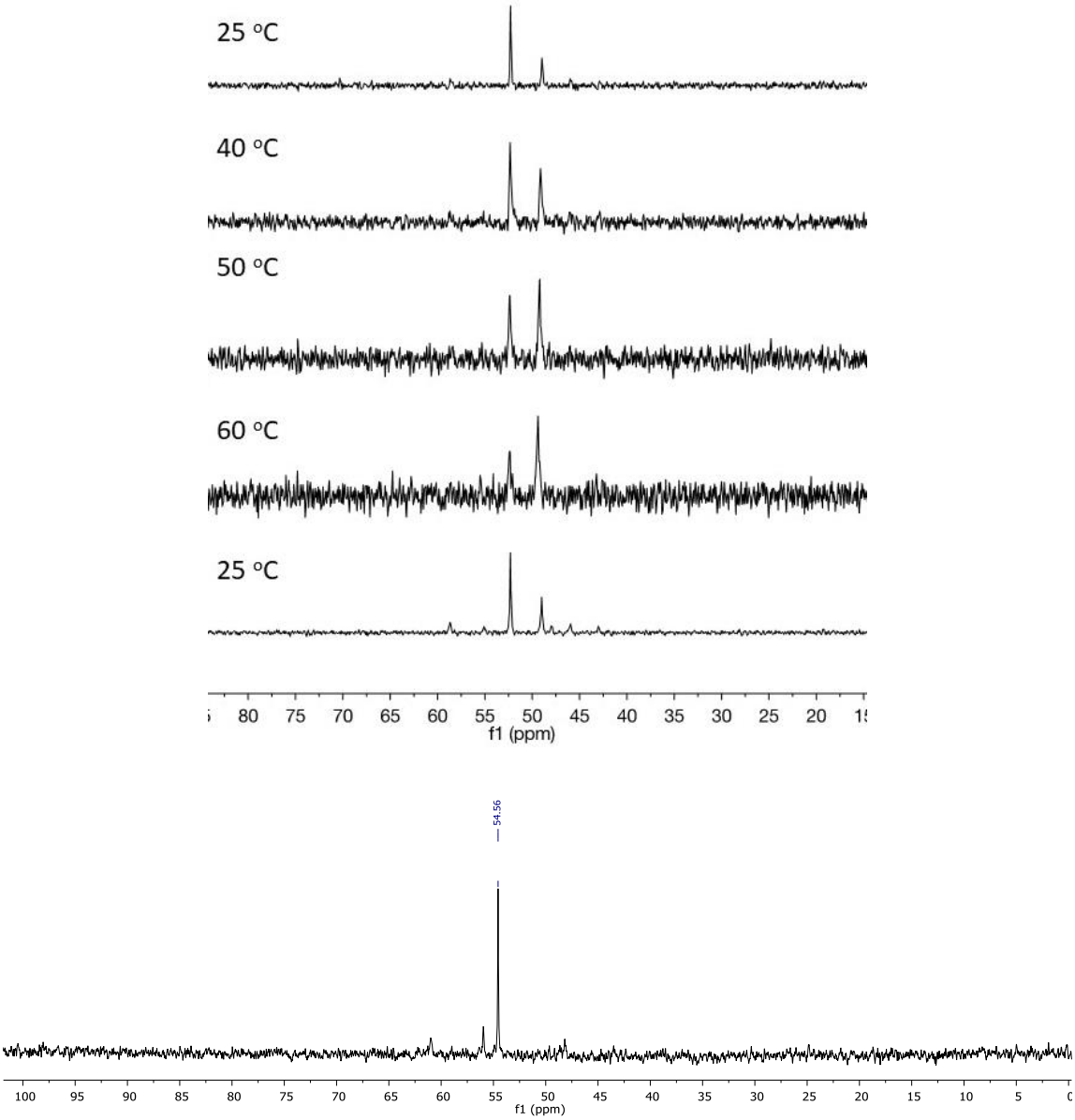

Figure 82. Top: Variable temperature ^{31}P NMR spectrum of a 1:1 mixture of complex **53** and *N*–phthaloyl–phenylalanine. Bottom: In situ ^{31}P NMR spectrum of carboxylate adduct with complex **53**.

Stimulated by this perspective, I decided to use acids such as *N*–phthaloyl–phenylalanine[215] (racemic) and L–*N*–tetrachlorophthaloyl–valine[216] as additives. These acids were added to a CH_2Cl_2 solution of **53** in 1:1 ratio. The ^{31}P NMR spectrum showed

two major resonances at 53.17 and 49.51 ppm for *N*–phthaloyl–phenylalanine in 1:1 ratio. The same observation was made for L–*N* tetrachlorophthaloyl–valine, which displayed two resonances at 53.17 and 49.51 ppm. Next, I performed a variable temperature NMR study to understate the fate of this reaction. The ^{31}P NMR spectrum of a 1:1 mixture of complex **53** and *N*–phthaloyl–phenylalanine was recorded at 25 ^{o}C, 40 ^{o}C, 50 ^{o}C, 60 ^{o}C, 25 ^{o}C respectively, as is shown in Figure 82. The NMR resonance at 53 ppm decreases in height as the temperature increases. At the same time, the resonance at 49 ppm increases in intensity. As the ^{31}P NMR resonance signal for complex **53** is at 49 ppm, it is safe to assume that this reaction takes place reversibly, resulting in a mixture of unreacted **53** and the desired carboxylate adduct.

Next, I decided to treat **53** with the sodium salt of the corresponding carboxylic acid. With this in mind, the sodium salt of L–*N*-tetrachlorophthaloyl–valine was generated by treating the carboxylic acid with Na_2CO_3 in methanol. Removal of the solvent led to a white solid which was used as is. Fortunately, reaction of this sodium salt with **53** led to the complete transformation to the desired carboxylate adduct as indicated by ^{31}P NMR spectroscopy. With this complex in hand, I became eager to test its catalytic properties. To test the validity of this approach, I studied the cyclization of methyl 2–(pent–4–ynyl)acetoacetate[217] (Conia–ene reaction) with 5 mol% of **53** and 5 mol% of the sodium salt additive (Figure 83). Gratifyingly, the cyclization reaction was completed in 20 min. No further efforts were dedicated to this project.

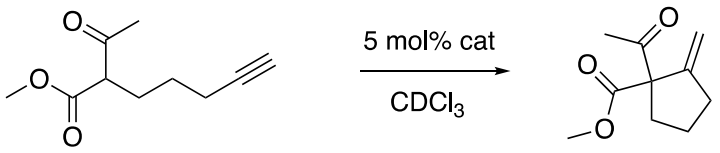

Figure 83. Catalysis of conia–ene reaction.

4.5 Conclusion

In summary, I describe a new highly electrophilic antimony-platinum complex (**53**) featuring three triflate ligands connected to the dinuclear core. This complex is readily isolable but yet it behaves as a highly active catalyst for reactions involving alkynes. Based on a comparison with other catalysts, we assign the unusual catalytic activity of this complex to the weakly coordinating nature of the triflate ligands which, we propose, facilitates access to a reactive platinum center.

4.6 Experimental

General experimental considerations: *Cis*–$PtCl_2(Et_2S)_2$ was prepared according to the reported procedures. Solvents were dried by passing through an alumina column (*n*–pentane and CH_2Cl_2) or by reflux under N over Na/K (Et_2O and THF). All other solvents were used as received. Commercially available chemicals were purchased and used as provided (Commercial sources: Aldrich for $SbCl_3$ and Bu_4NF; Strem chemicals for $AgSbF_6$). Ambient temperature NMR spectra were recorded on a Varian Unity Inova 500 FT NMR (499.42 MHz for ^1H, 125.62 MHz for ^{13}C, 469.89 MHz for ^{19}F, 202.16 MHz for ^{31}P). ^1H and ^{13}C NMR chemical shifts are given in ppm and are referenced against

$SiMe_4$ using residual solvent signals used as secondary standards. ^{19}F NMR chemical shifts are given in ppm and are referenced against $CFCl_3$ using BF_3–Et_2O as an external secondary standard with δ -153.0 ppm. Elemental analyses (EA) were performed at Atlantic Microlab (Norcross, GA).

General procedure for catalytic enyne cyclization reactions: Catalytic reactions were carried out at ambient temperature under air. To a solution of the appropriate enyne in CH_2Cl_2 (1 mL), catalytic amount of catalyst (5 %) in 1 mL of CH_2Cl_2 was added. The reaction mixture was stirred and monitored by ^1H NMR. When the reaction was completed, the conversion was determined by ^1H NMR.

Computational Details: Density functional theory (DFT) structural optimizations were performed on the solid state structures of complexes **53** and **54** using Gaussian 09 suite of programs with effective core potentials on all heavy atoms (functional: BP86; mixed basis set: Sb/Pt: cc-pVTZ-PP; P/S/Cl: 6-31g(d); H/C/O: 6-31g, F: 6-31+g(d'). Frequency calculations were used to confirm convergence of the calculations. The optimized structures, which are in excellent agreement with the solid-state structures were subjected to a NBO analysis and were visualized and plotted using the Jimp 2 program.[170]

Crystallographic Measurements: The crystallographic measurements were performed at 110(2) K using a Bruker APEX–II CCD area detector diffractometer (Mo-K_α radiation, λ = 0.71069 Å). In each case, a specimen of suitable size and quality was selected and mounted onto a nylon loop. The structures were solved by direct methods, which successfully located most of the non-hydrogen atoms. Semi-empirical absorption

corrections were applied. Subsequent refinement on F^2 using the SHELXTL/PC package (version 6.1) allowed location of the remaining non–hydrogen atoms.

Synthesis of 52: A solution of $PtCl_2(Et_2S)_2$ (50.3 mg, 0.13 mmol) in CH_2Cl_2 was added to a solution of $(o\text{–}(^i Pr_2P)C_6H_4)_2SbCl$ (70.4 mg, 0.13 mmol) in CH_2Cl_2 under N_2 and reflux for 16 h. The resulting yellow reaction mixture was concentrated to 2 mL in vacuo, and the product was precipitated by addition of Et_2O. The product was filtered and washed with pentane to afford **52** (86 mg, 83% yield) as yellow solids. Single crystals of **52** suitable for X-ray diffraction were obtained by vapor diffusion of pentane into a solution of the compound in CH_2Cl_2. ^{1}H NMR (499.43 MHz; $CDCl_3$): δ 8.26 (d, 2H, *o*–P(Sb)C_6H_4, $^3J_{H–H}$ = 7.6 Hz), 7.75 (m, 4H), 7.52 (t, 2H, *m*–P(Sb)C_6H_4, $^3J_{H–H}$ = 6.9 Hz), 3.22 (m, 4H, C*H*CH_3), 1.43 (t, 6H, *J* = 7.5 Hz), 1.41 (t, 6H, *J* = 8.0 Hz), 1.25 (t, 6H, *J* = 7.5 Hz), 1.24 (t, 6H, *J* = 7.5 Hz). ^{13}C{^{1}H} NMR (125.62 MHz; $CDCl_3$): δ 167.88 (t, $J_{C–P}$ = 15.6 Hz), 134.41 (s), 131.89 (t, $J_{C–P}$ = 3.1 Hz), 131.64 (t, $J_{C–P}$ = 7.0 Hz), 129.88 (t, $J_{C–P}$ = 3.5 Hz), 125.48 (t, $J_{C–P}$ = 25.0 Hz), 27.98 (t, $J_{C–P}$ = 14.6 Hz, *C*$(CH_3)_2$), 19.19 (s, *C*H_3), 19.09 (s, *C*H_3). ^{31}P{1H} NMR (161.74 MHz; $CDCl_3$): δ 72.63 (s, $^1J_{Pt–P}$ = 2473 Hz). Elemental analysis calcd (%) for C24H36Cl3P2PtSb: C, 35.60; H, 4.48. Found: C, 35.38; H, 4.39.

Synthesis of 53: Complex **43** (208 mg, 0.22 mmol) was dissolved in CH_2Cl_2 (2 mL) and treated with AgOTf (169 mg, 0.66 mmol) under an N_2 atmosphere. The reaction mixture was allowed to stir for 16 h, resulting in white suspension, which is filtered over Celite. The filtrate was treated with hexane (2 mL), leading to precipitation of the product (**53**) as a white solid. The product was isolated by filtration and dried in vacuo (220 mg,

78% yield). ^{1}H NMR (399.43 MHz; $CDCl_3$): δ 8.72 (d, 2H, *o*–P(Sb)C_6H_4, $^{3}J_{H–H}$ = 8.0 Hz), 7.90 (t, 2H, $^{3}J_{H–H}$ = 7.6 Hz), 7.76 -7.61 (m, 12H), 7.59 -7.45 (m, 12H). $^{13}C\{^{1}H\}$ NMR (125.62 MHz; $CDCl_3$): δ 135.28 (s), 134.82 (brs), 134.49 (s), 134.12 (t, $J_{C–P}$ = 6.9 Hz), 133.87 (brs), 132.82 (s), 129.62 (t, $J_{C–P}$ = 5.8 Hz), 126.34 (t, $J_{C–P}$ = 29.5 Hz). $^{31}P\{1H\}$ NMR (161.74 MHz; $CDCl_3$): δ 49.41 (s, $^{1}J_{Pt–P}$ = 2450 Hz). $^{19}F\{^{1}H\}$ NMR (469.89 MHz; CD_2Cl_2): δ -80.4 (brs), -80.85 (s). Elemental analysis calcd (%) for $C_{39}H_{28}F_9O_9P_2PtS_3Sb$: C, 36.41; H, 2.19. Found: C, 35.08; H, 2.30.

Synthesis of 54: Complex **52** (80 mg, 0.10 mmol) was dissolved in CH_2Cl_2 (2 mL) and treated with AgOTf (77 mg, 0.30 mmol) under an N_2 atmosphere. The reaction mixture was allowed to stir for 16 h, resulting in yellow suspension, which is filtered over Celite. The filtrate was treated with hexane (2 mL) leading to precipitation of the product (**54**) as a yellow solid. The product was isolated by filtration and dried in vacuo (84 mg, 73% yield). ^{1}H NMR (399.43 MHz; $CDCl_3$): δ 8.74 (d, 2H, *o*–P(Sb)C_6H_4, $^{3}J_{H–H}$ = 7.9 Hz), 8.01-7.88 (m, 4H), 7.85 (t, 2H, *m*–P(Sb)C_6H_4, $^{3}J_{H–H}$ = 7.4 Hz), 3.44 (m, 4H, C*H*CH_3), 1.36 (t, 6H, *J* = 7.3 Hz), 1.32 (t, 6H, *J* = 8.3 Hz), 1,26 (t, 6H, *J* = 7.5 Hz), 1.24 (t, 6H, *J* = 7.3 Hz). $^{13}C\{^{1}H\}$ NMR (125.62 MHz; $CDCl_3$): 152.04 (t, $J_{C–P}$ = 11.6 Hz), 135.14 (t, $J_{C–P}$ = 5.5 Hz), 134.64 (s), 133.47 (s), 133.19 (t, $J_{C–P}$ = 3.5 Hz), 131.39 (t, $J_{C–P}$ = 23.9 Hz), 27.95 (t, $J_{C–P}$ = 13.9 Hz, *C*$(CH_3)_2$), 18.69 (s, *C*H_3), 18.58 (s, *C*H_3). $^{31}P\{1H\}$ NMR (161.74 MHz; $CDCl_3$): δ 73.94 (s, $^{1}J_{Pt–P}$ = 2383 Hz). $^{19}F\{^{1}H\}$ NMR (469.89 MHz; CD_2Cl_2): δ -79.2 (s, 3F), -81.5 (s, 9F). Elemental analysis calcd (%) for $C_{27}H_{36}F_9O_9P_2PtS_3Sb$: C, 28.19; H, 3.15. Found: C, 28.19; H, 2.99.

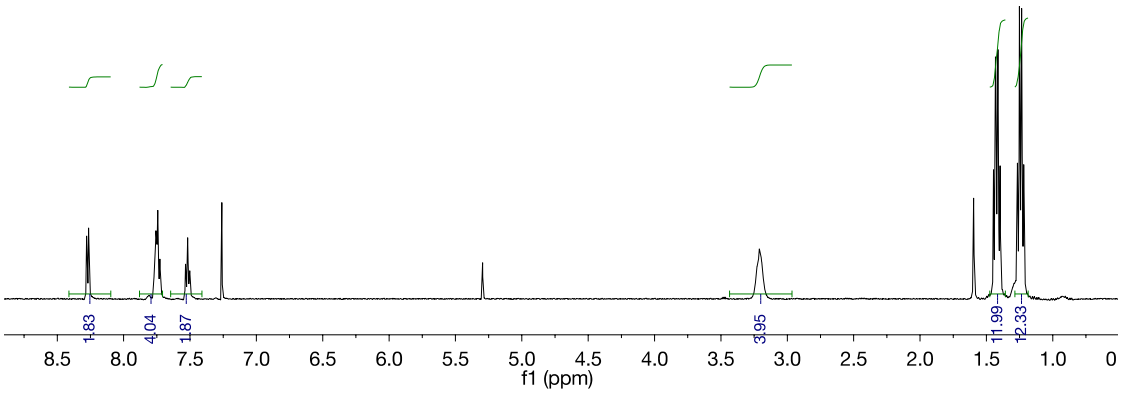

Figure 84. ^{1}H NMR spectrum of **52** in $CDCl_3$.

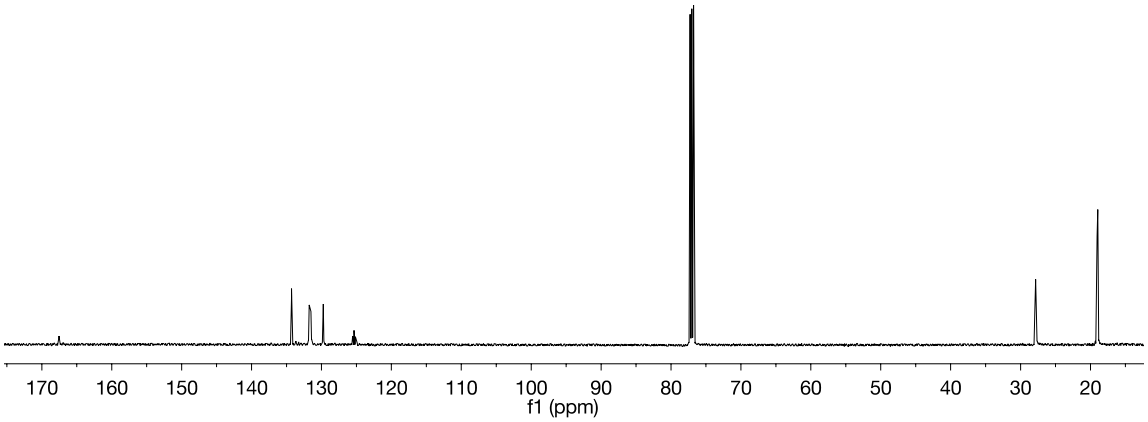

Figure 85. ^{13}C NMR spectrum of **52** in $CDCl_3$

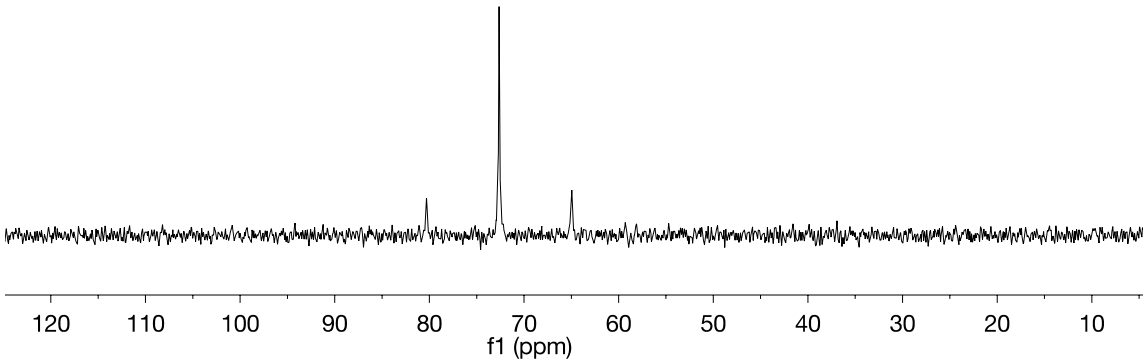

Figure 86. ^{31}P NMR spectrum of **52** in $CDCl_3$

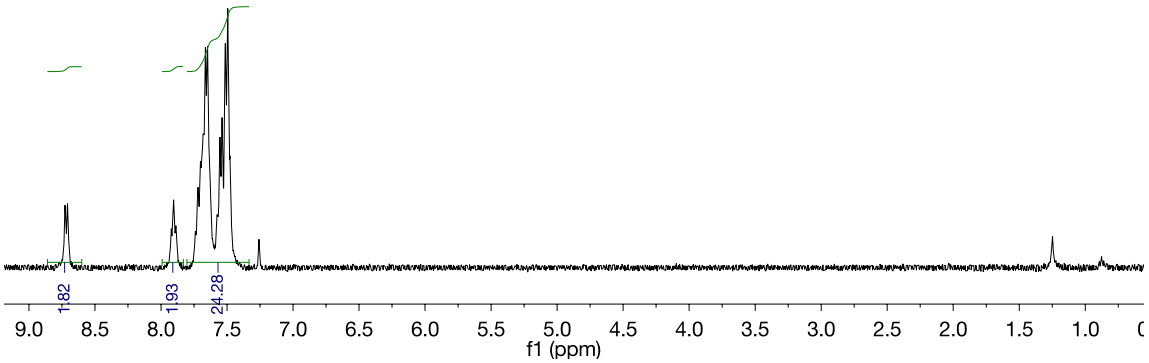

Figure 87. ^{1}H NMR spectrum of **53** in $CDCl_3$

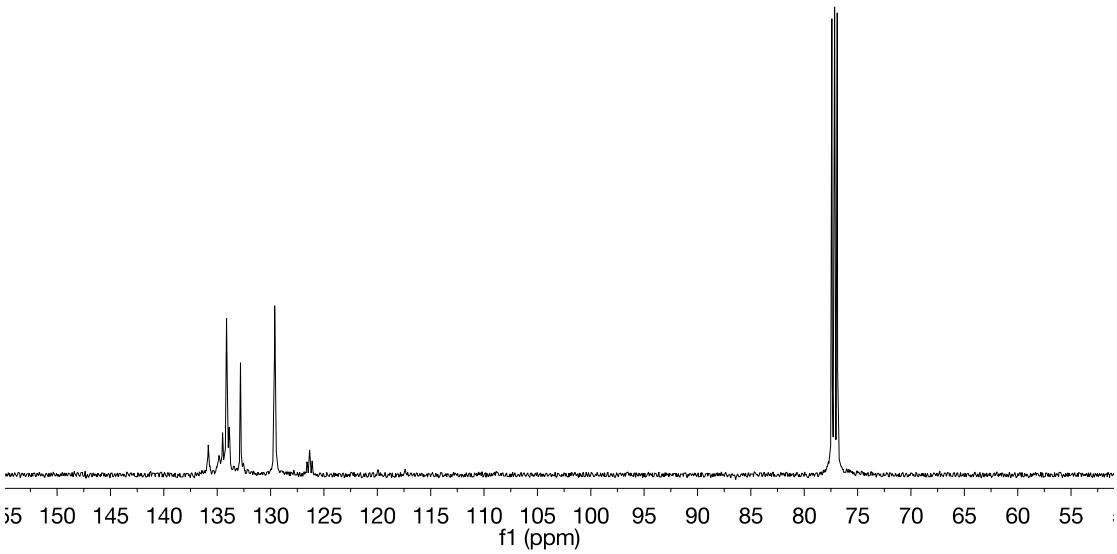

Figure 88. ^{13}C NMR spectrum of **53** in $CDCl_3$

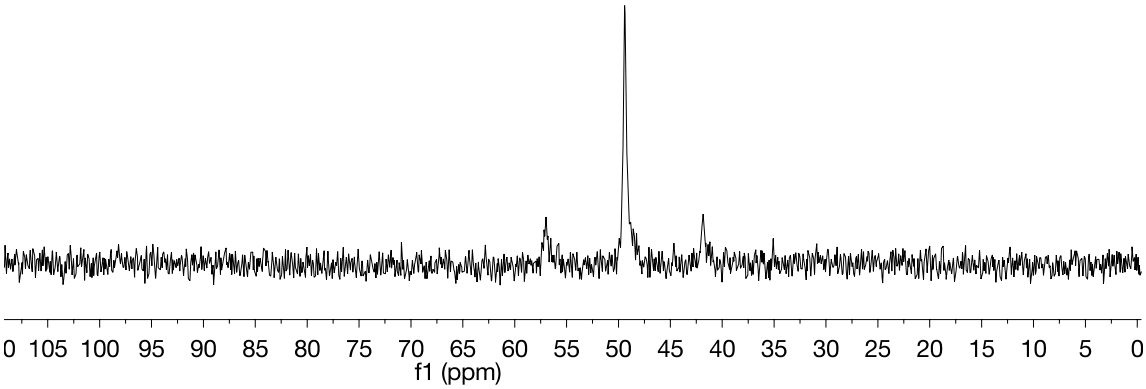

Figure 89. ^{31}P NMR spectrum of **53** in $CDCl_3$

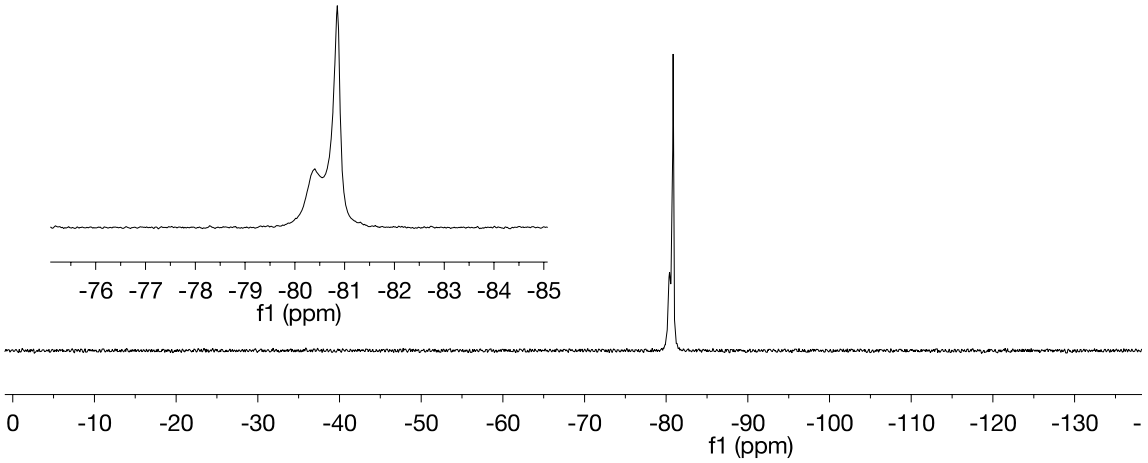

Figure 90. ^{19}F NMR spectrum of **53** in $CDCl_3$.

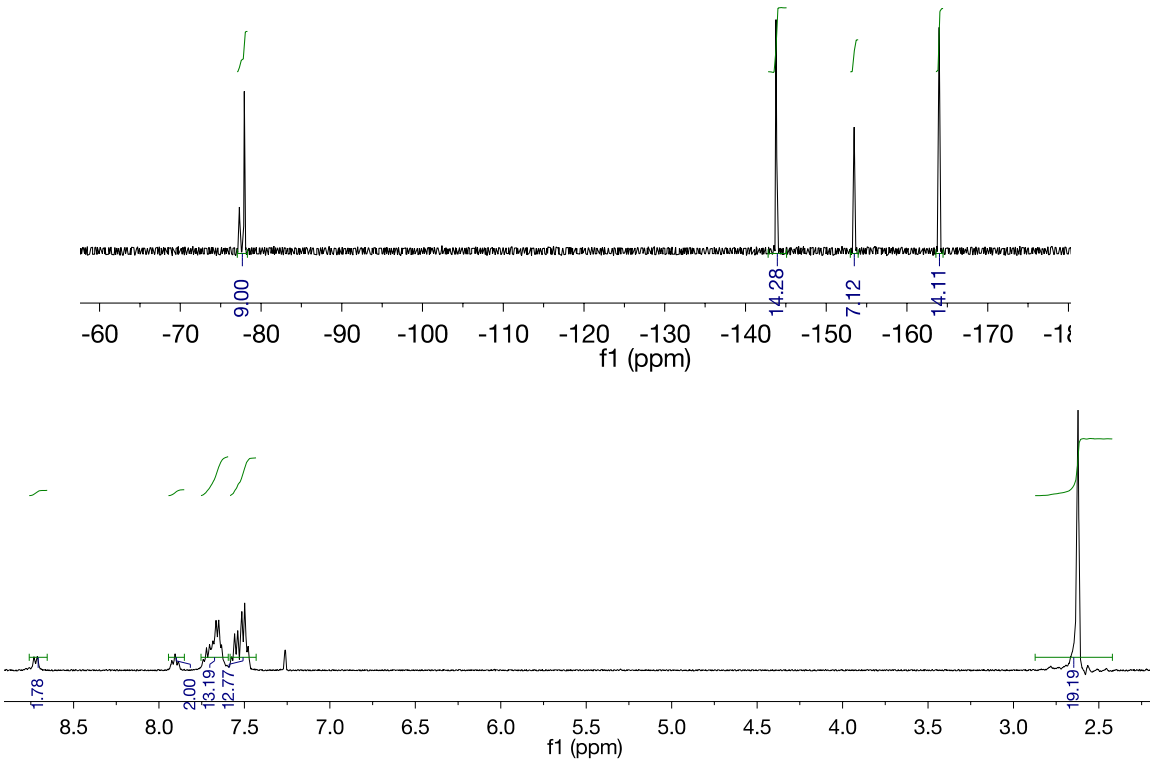

Figure 91. ^{1}H NMR spectrum and ^{19}F NMR spectrum of **53** in $CDCl_3$ with pentafluoroacetophenone as an internal standard. (400M Hz)

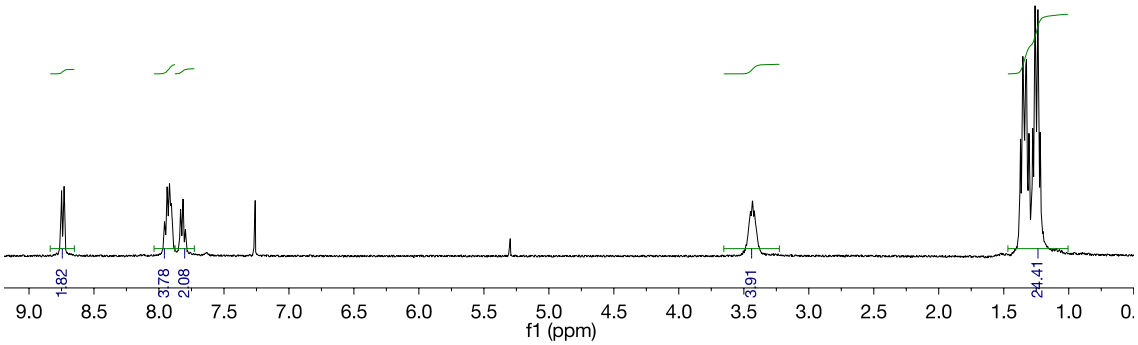

Figure 92. ^{1}H NMR spectrum of **54** in $CDCl_3$.

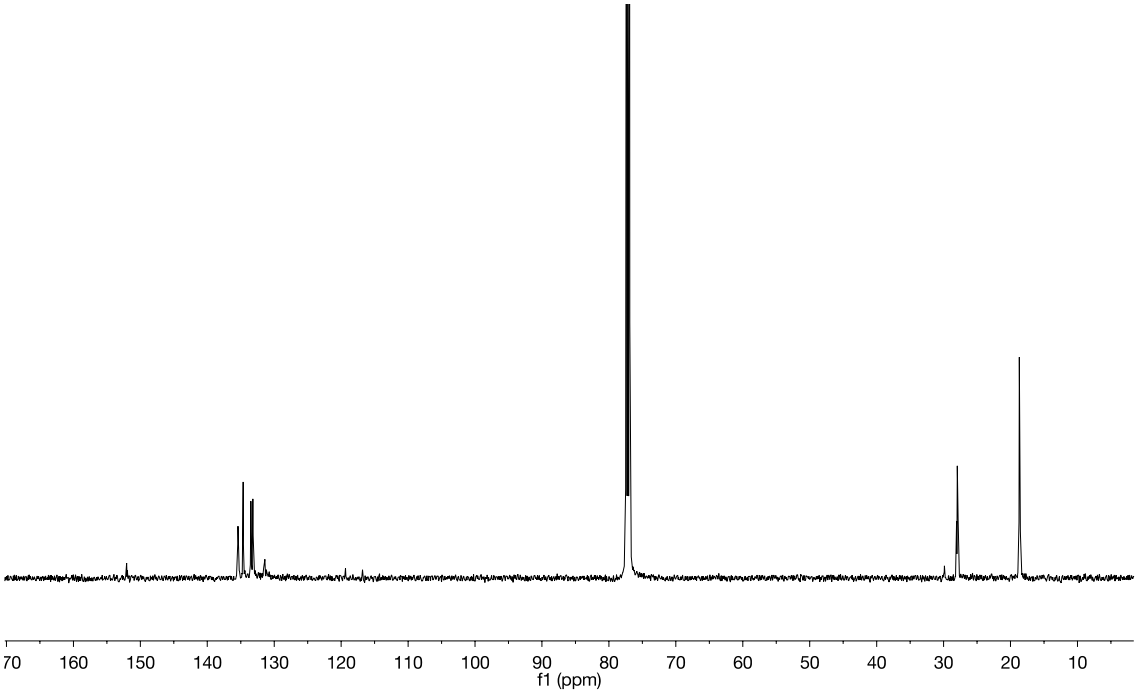

Figure 93. ^{13}C NMR spectrum of **54** in $CDCl_3$. The $CDCl_3$ solvent residual peak is truncated.

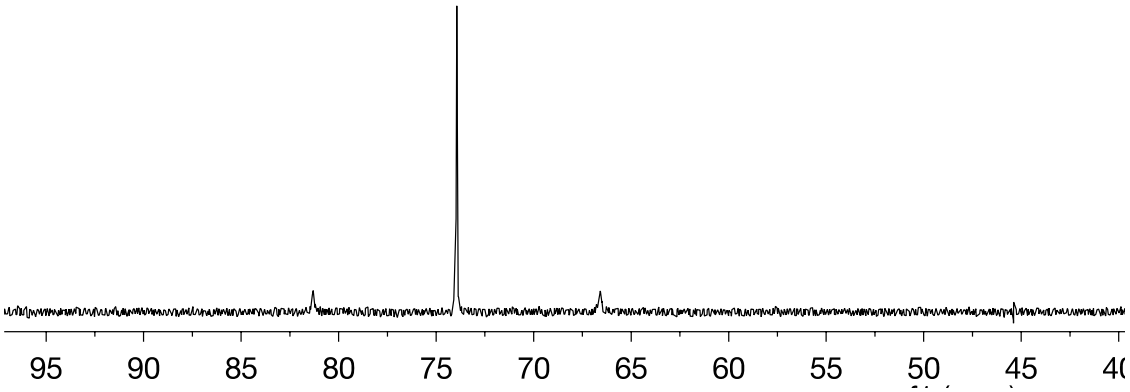

Figure 94. ^{31}P NMR spectrum of **54** in $CDCl_3$

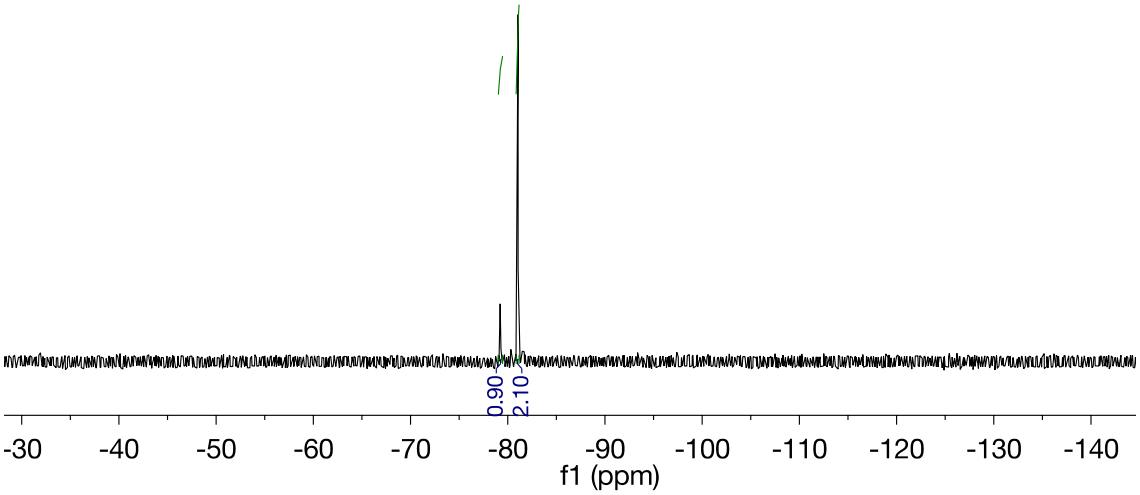

Figure 95. ^{19}F NMR spectrum of **54** in $CDCl_3$.

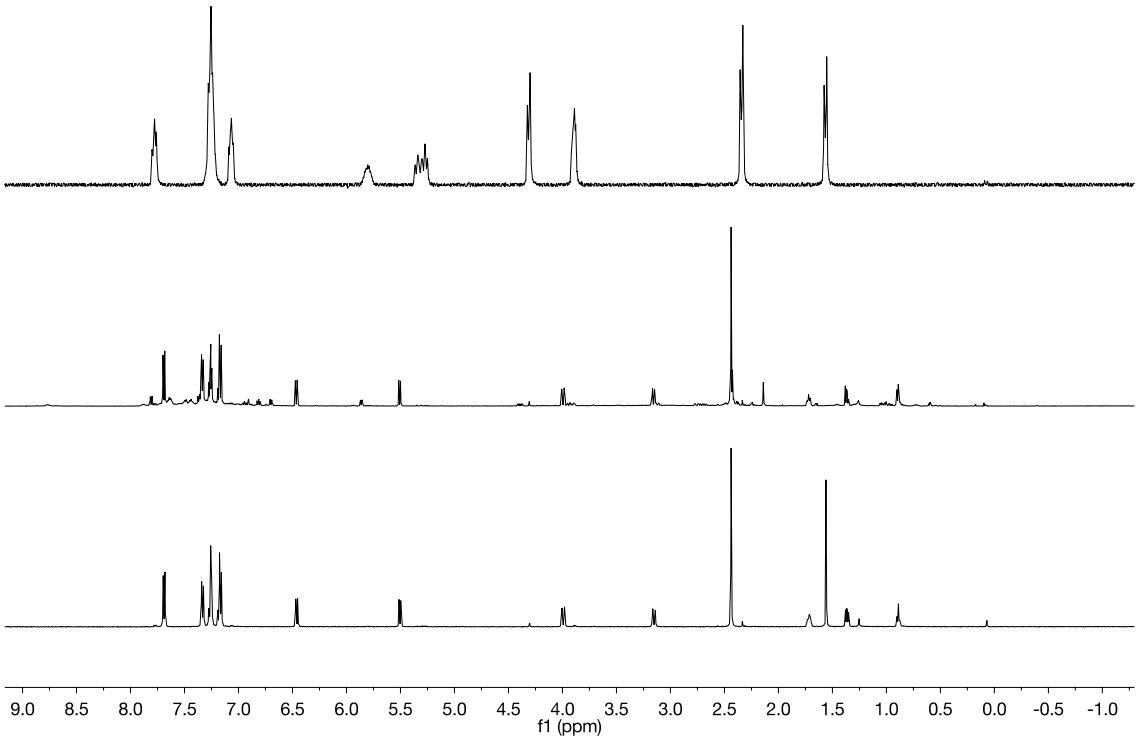

Figure 96. Top: ^{1}H NMR spectrum of the starting material of thiophene and ethyl propiolate. Middle: In situ ^{1}H NMR spectrum recorded during the catalytic reaction after 7h. Bottom: Isolated products.

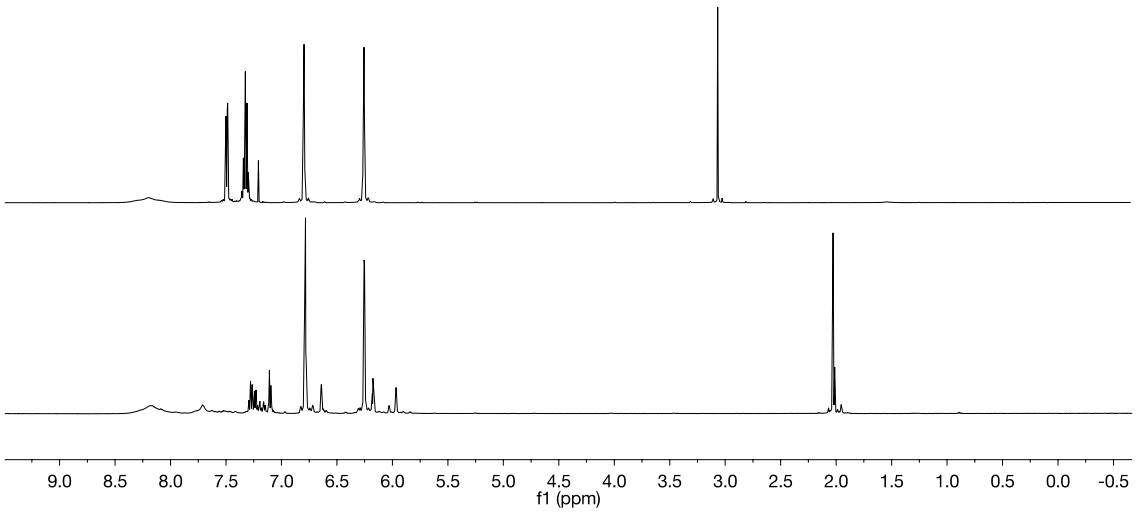

Figure 97. Top: ^{1}H NMR spectrum of the starting material of pyrrole and phenylacetylene. Bottom: In situ ^{1}H NMR spectrum recorded during the catalytic reaction after 10 min.

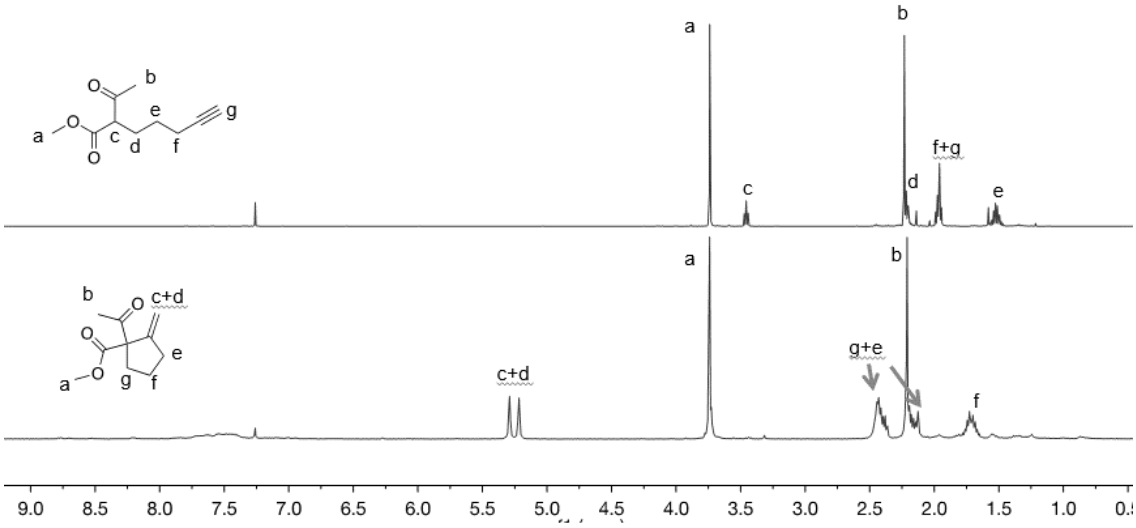

Figure 98. Top: ^{1}H NMR spectrum of the starting material of the Conia–ene reaction. Bottom: In situ ^{1}H NMR spectrum recorded during the catalytic reaction after 1 h.

CHAPTER V

BIFUNCTIONAL DISTIBORANE(V) COMPOUNDS BASED ON *ORTHO*–PHENYLENE BACKBONES

5.1 Introduction

Previous efforts in our group have shown that stiborane derivatives such as **8** can be used for the complexation of fluoride anions in various media. .For example, compound **8** readily binds fluoride in the presence of 95% water while its monofunctional analog $Ph_3Sb(O_2C_6Cl_4)$ shows no measurable fluoride anion binding under the same conditions. This demonstrates that the fluoride affinity is drastically increased as a result of chelation. Similar properties are displayed by bifunctional stiborane **9**, which bears the 1,8–triptycenediyl backbone (Figure 99).[74]

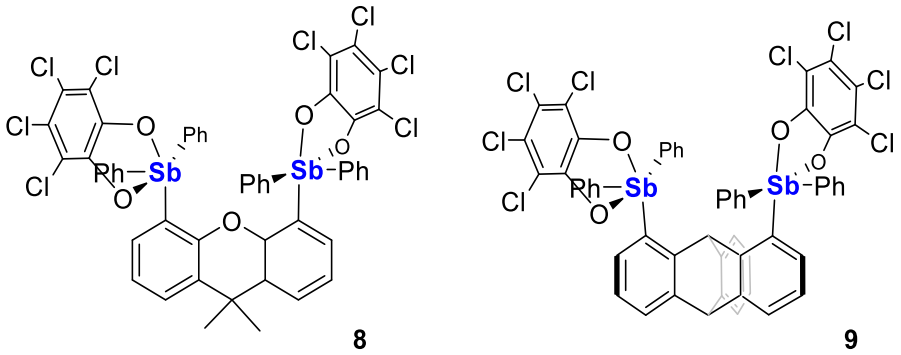

Figure 99. Examples of bifunctional Sb(V) containing species.

The scope of backbones supporting multidentate Lewis acids is not limited to 9,9–dimethylxanthene or 1,8–triptycene backbones. Other platforms such as naphthalene[218,219]

and *ortho*–phenlyene[68,220,221] have also been used to support multiple Lewis acidic functionalities (Figure 100). All of these molecules display higher anion affinities than their monofunctional analogue, indicating the generality of this bifunctionality strategy.

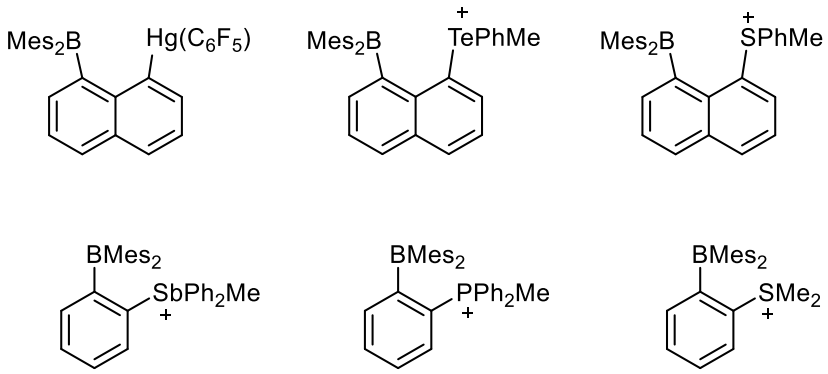

Figure 100. Examples of naphthalene and *ortho*–phenylene bidentate Lewis acids containing boranes and hybrid elements**.**

As part of our ongoing interest in organoantimony(V) chemistry, we decided to investigate bifunctional distiboranes based on the *ortho*–phenylene backbones. We have previously synthesized complexes **56** and **57** and studied their fluoride binding abilities (Figure 101). In this chapter, I will target distiboranes based on perfluoro–*ortho*–phenylene backbone. Although this backbone has been employed before in boron[222-224] and mercury[225-227] chemistry, its use in antimony chemistry is underexplored. The perfluoro–*ortho*–phenylene backbone is electron withdrawing which should increase the Lewis acidity of the compounds.

5.2 Previous results

Masato Hirai, a former student in the Gabbaï group, synthesized and fully characterized derivatives **56** and **57**. Both molecules have C_2 symmetry with a cavity in between the two antimony(V) centers that could accommodate incoming anions. The fluoride adducts of both complexes, TBA[**56**–F] and TBA[**57**–F], have also been obtained by reaction with tetrabutylammonium difluorotriphenylsilicate (TBAT),which is a fluoride source, and the corresponding crystal structures were determined.

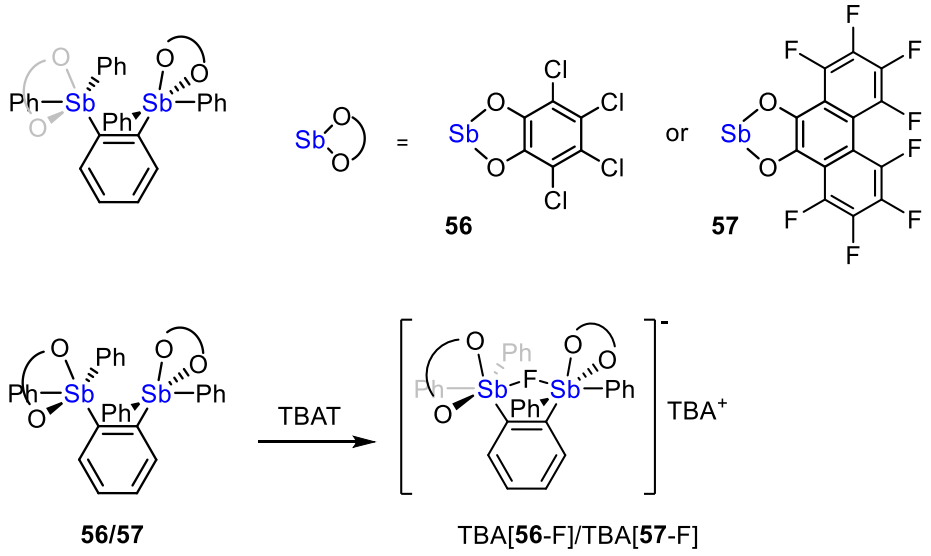

Figure 101. Previously synthesized distiboranes with the *ortho*–phenylene backbone and the synthesis of fluoride adducts of complexes **56** and **57**.

More importantly, the gas phase fluoride ion affinity (FIA) of **56** has been estimated using computational methods. These calculations show that the FIA of **56** is 378.4 kJ mol^{-1}, which is 18.5 kJ mol^{-1} higher than that of the 9,9–dimethylxanthene analog **8** (FIA = 359.9 kJ mol^{-1}). The fluoride affinity of those complexes was also compared by

conducting a competition experiment. For example, reaction of **56** with equimolar amount of [**58**]$^{-}$ in $CDCl_3$ led to a quantitative formation of [**56**–F]$^{-}$ and **8**, thus indicating that **56** is more fluoridophilic than **8**. (Figure 102).

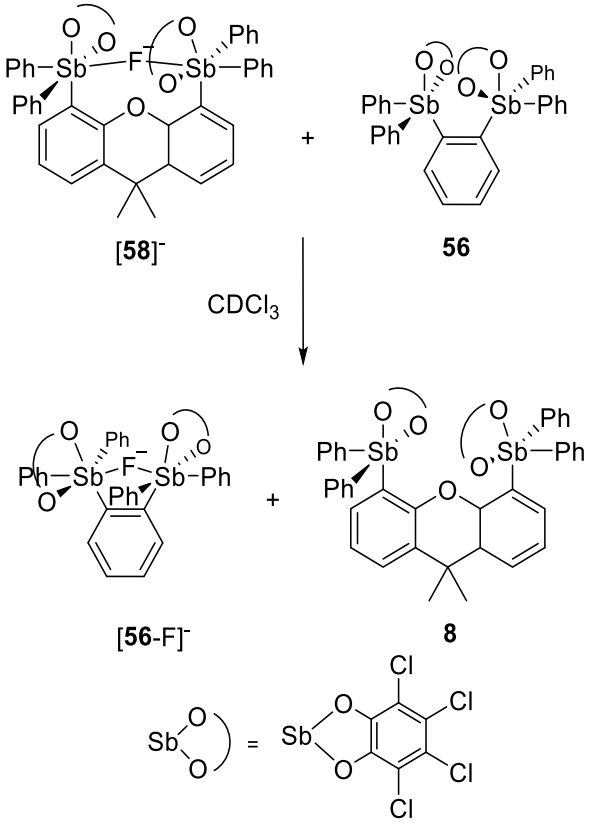

Figure 102. The competition experiment of **56** and [**58**]$^{-}$ in $CDCl_3$.

With these complexes in hand, we became eager to test whether the fluoride ion affinity could be further enhanced by a more electron withdrawing backbone. In the next sections, I will discuss the synthesis and anion binding properties of a series of related complexes based on the perfluoro–*ortho*–phenylene backbone.

5.3 Synthesis of the distiboranes

The distibine **59** was prepared by treating the 1,2–dibromo–3,4,5,6–tetrafluorobenzene with *n*–BuLi (2.4 equiv) in THF at -65 ^{o}C (Figure 103). After stirring this reaction at low temperature for 1 h, diphenylantimony chloride (2.4 equiv) in THF solution was added to quench the dilithium salt. Compound **59** was separated using column chromatography and isolated as a white crystalline solid. This reaction can be easily monitored by ^{19}F NMR spectroscopy, which shows two resonances at -113.99 and -153.42 ppm in a 1:1 ratio corresponding to the fluorine on the tetrafluorobenzene backbone. The ^{1}H NMR shows that the four phenyl rings on antimony are equivalent in solution.

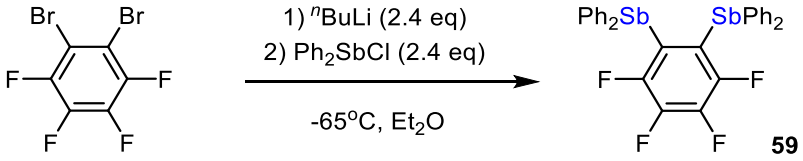

Figure 103. Synthesis of complex **59**.

With this compound in hand, we decided to oxidize the antimony center with *o*–chloranil. Complex **59** underwent a clean oxidation with two equivalents of *o*–chloranil to afford **60** as a bright yellow solids in 93% yield (Figure 104). Unfortunately, **60** is insoluble in common organic solvents preventing its characterization by NMR spectroscopy. However, the formation of **60** could be monitored by ^{19}F NMR during the

reaction, before precipitation occurred. Upon mixing **59** with *o*–chloranil, the solution turned yellow immediately. *In situ* ^{19}F NMR spectroscopy reveals two new resonances at -120 and -150 ppm. These two signals diminished in intensity over time as **60** precipitated out of solution.

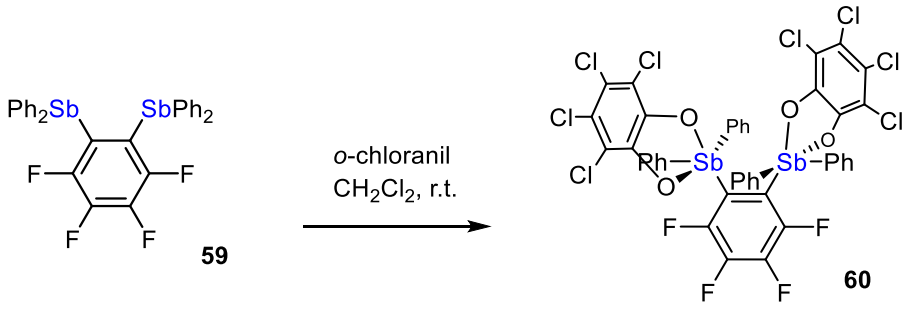

Figure 104. Synthesis of complex **60**.

Single crystals of **60** were obtained by layering a diethyl ether solution of *o*–chloranil with a CH_2Cl_2 solution of **59** at ambient temperature. The structure was determined by X-ray diffraction analysis (Figure 105). The distiborane units adopt a distorted square-pyramidal geometry with an average τ-value of 0.14, which could be the result of repulsions between the distiborane moieties. Such a repulsive interaction is also supported by the values of the Sb2–C2–C1 (123.982(2)^o) and Sb1–C1–C2 (124.219(2)^o) angles, which are larger than the ideal value of 120^o. Comparisons of the structure of **60** with that of **56** reveals a larger Sb–Sb separation in **60** (**56**: 3.7773(5) Å; **60**: 3.8176(8) Å). The average Sb1–O4 and Sb2–O2 distances in both **56** (2.816 Å) and **60** (2.8409 Å) are within the sum of the van der Waals radii of antimony and oxygen (3.05 Å), indicating weak interactions between the antimony and the neighboring oxygen atom.

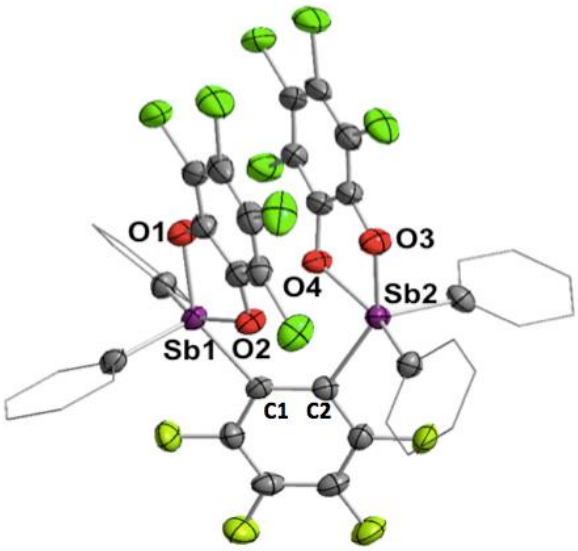

Figure 105. Solid-state structure of **60**. Thermal ellipsoids are drawn at the 50 % probability level. The hydrogen atoms are omitted for clarity. Selected bond lengths (Å) and angles (deg): Sb1–Sb2 3.8176(8), Sb1–O1 2.0369(2), Sb1–O2 2.086(2), Sb1–O4 2.841(2), Sb2–O2 2.841(2), O1–Sb1–O2 79.91(8), Sb1–C1–C2 124.22(2).

To better understand the nature of these differences, **60** has also been investigated computationally using density functional theory (DFT) methods (B3LYP functional with the mixed basis sets: aug-cc-pVTZ-pp for Sb, 6-311g(d) for Cl, 6-31g(d') for F, 6-31g for C, O, and H. The calculations show that the LUMO is concentrated on both antimony(V) centers and has a high Sb–C_{Ph} σ^* character (Figure 106).

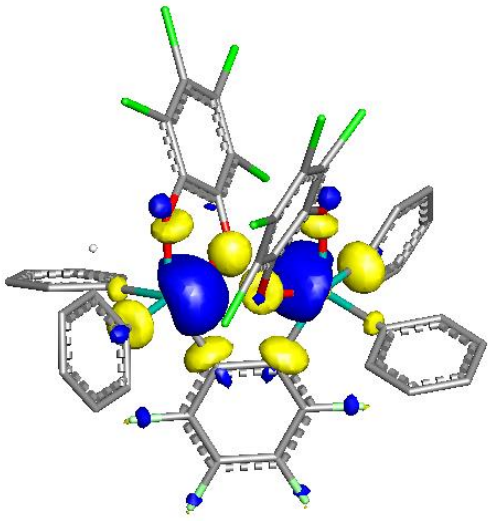

Figure 106. Contour plot of the LUMO of **60** (isovalue = 0.05**).**

Next, we decided to study the fluoride anion binding properties of **60**. Complex **60** was treated with TBAT in CH_2Cl_2. Despite the poor solubility of **60**, addition of TBAT to a yellow suspension of the compound led to a clear and colorless solution (Figure 107). Evaporation of the solvent followed by washing of the residue with Et_2O afforded TBA[**60**–F] as a white solid. The ^{19}F NMR spectrum shows three resonances at -68.04, -119.59, and -154.43 ppm, respectively in a 1 : 2 : 2 ratio. The ^{19}F NMR resonance at -68.04 ppm is very close to the resonance of the bridging fluoride anion in TBA[**60**–F] (-73.3 ppm in $CDCl_3$). These values are slightly downfield from the fluorine resonance signal in TBA[$Ph_3Sb(cat)F$] (-84.6ppm in $CDCl_3$).[65] They are also comparable with that in Ph_4SbF (-81.4 ppm), which contains a covalent Sb–F bond. In comparison, these values are notably different from the fluorine signals of complex [**58**]$^-$, which appears at -26.5 ppm in $CDCl_3$.

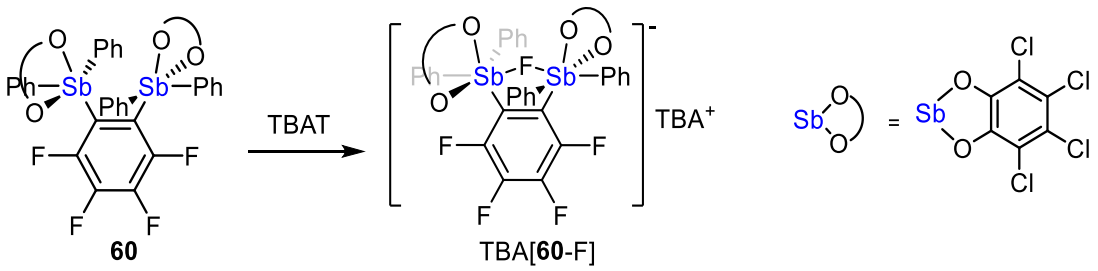

Figure 107. Synthesis of TBA[**60**–F].

To obtain structural insights into TBA[**60**–F], crystals of TBA[**60**–F] were grown by slow diffusion of pentane vapors into a CH_2Cl_2 solution of the salt. The solid-state structure, which was determined by X-ray crystallography, confirmed fluoride anion chelation. In the solid-state, the antimony centers adopt a distorted octahedral geometry. Comparison of the crystal structure of TBA[**60**–F] with TBA[**56**–F] reveals some interesting features. While TBA[**56**–F] still retains C2 symmetry with the fluoride anion positioned trans to two phenyl rings, TBA[**60**–F] crystallizes in a structure of lower symmetry. The fluoride anion is positioned trans to a phenyl ring on one side and trans to a oxygen atom on the other side. This geometry could be the result of crystal packing forces since the ^{19}F NMR spectrum of TBA[**60**–F] in solution is consistent with a symmetrical structure with only two resonances corresponding to the tetrafluorobenzene backbone. In TBA[**56**–F], the fluoride anion sits close to the plane containing the *ortho*-substituted benzene backbone. The Sb1–Sb2 separations are 3.8569(5) Å in TBA[**56**–F] and 3.8643(24) Å in TBA[**60**–F]. These values are slightly increased when compared with the compounds in their fluoride-free form (**56**: 3.7773(5) Å; **60**: 3.8176(8) Å). This slight increased separation may be the result of increased steric as a result of fluoride anion addition. The Sb–F bond lengths (2.1213(14) Å for Sb1–F1 and 2.2356(14) Å for Sb2–F1

in TBA[**56**–F]; 2.2903(65) Å for Sb1–F1, and 2.1069(72) Å for Sb2–F1 in TBA[**60**–F]) are comparable to the Sb-F separations in the fluoride adduct of 9,9–dimethylxanthene. On the other hand, the Sb1–F1–Sb2 angles (124.54(7)^{o} in TBA[**56**–F], 122.943(31)^{o} in TBA[**60**–F]) (Figure 108) indicated significant bending of the Sb-F-Sb motif. The same motif in [**58**]$^{-}$ was significantly more linear (Sb-F-Sb angle 165.45(9)°). These differences are assigned to the structure of the distiboranes.

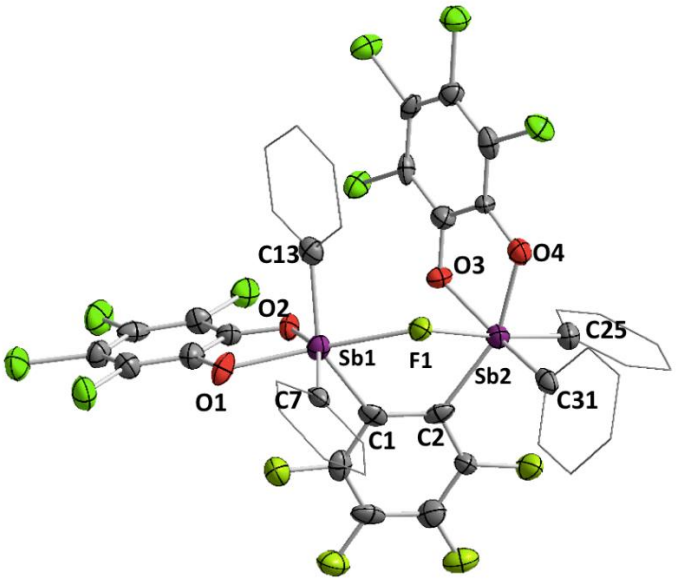

Figure 108. Crystal structure of TBA[**60**–F]. Thermal ellipsoids are drawn at the 50 % probability level. The hydrogen atoms and tetrabutylammonium cation are omitted for clarity. Selected bond lengths (Å) and angles (deg) of TBA[**60**–F]: Sb1–Sb2 3.8643(2), Sb1–F1 2.2903(7), Sb2–F1 2.1069(7), Sb1–F1–Sb2 122.943(3), F1–Sb2–O1 162.959(3), F1–Sb2–C25 169.25(8), O1–Sb1–O2 76.253(3), O3–Sb2–O4 78.76(7).

Having confirmed the bidentate nature of complex TBA[**60**–F], we wanted to compare the Lewis acidity of **60** to that of the previously synthesized derivatives **8** and **56**. We first computed the fluoride ion affinity (FIA) of **60** and found it to be equal to 388.3 kJ mol^{-1}. This FIA is 9.9 kJ mol^{-1} higher than that of **56** (378.4 kJ mol^{-1}) and 28.42 kJ mol^{-}

[1] than that of **8** (359.88 kJ mol^{-1}). These calculations support the notion that fluorination of the *o*–phenylene backbone enhances the Lewis acidity of the Sb(V) centers.

Next, we decided to carry out a competition experiments in order to compare the fluoride anion affinity of **56** and **60** (Figure 109). However, the low solubility of **60** prevented us from testing the reaction of **60** with TBA[**56**–F]. Faced with this difficulty, we decided to add 1 equivalent of $Al(NO_3)_3$ to a 1:1 mixture of TBA[**56**–F] and TBA[**60**–F] in THF. This reaction afforded complete decomplexation of TBA[**56**–F], while TBA[**60**–F] remained intact. This result supports the notion that **60** indeed has a higher fluoride affinity than **56**. Addition of more of $Al(NO_3)_3$ led to decomplexation of TBA[**60**–F].

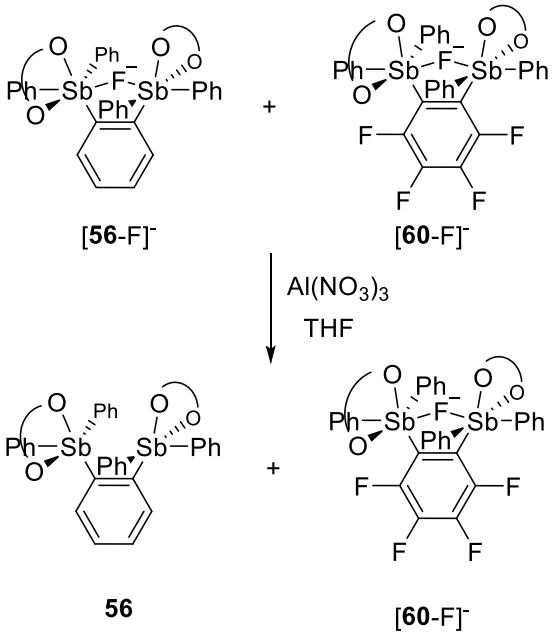

Figure 109. Reverse competition experiment of TBA[**56**–F] and TBA[**60**–F] with $Al(NO_3)_3$

5.4 Synthesis and properties of a distiborane obtained by oxidation of the distibine 59 with octafluorophenanthra–9,10–quinone

Contemplating strategies that would ameliorate the solubility of these compounds, we considered octafluorophenanthra–9,10–quinone as an oxidant.[228,229] Complex **61** could be easily generated by treatment of **59** with 2 equivalents of octafluorophenthra–9,10–quinone (Figure 111). After stirring the solution for 30 min, solvents were evaporated, and the remaining solid was washed with Et_2O, affording **61** as a yellow solid. This compound is very soluble in THF and CH_2Cl_2. While the ^{19}F NMR spectrum of the octafluorophenanthra–9,10–quinone exhibits four distinct resonances, the ^{19}F NMR spectrum of **61** shows ten peaks in $CDCl_3$, consistent with the formation of a compound of C_2 symmetry.

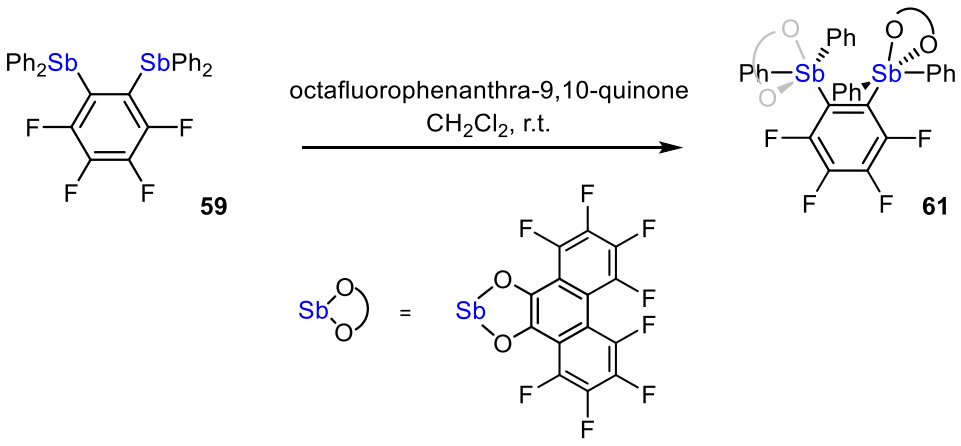

Figure 110. Synthesis of complex **61**.

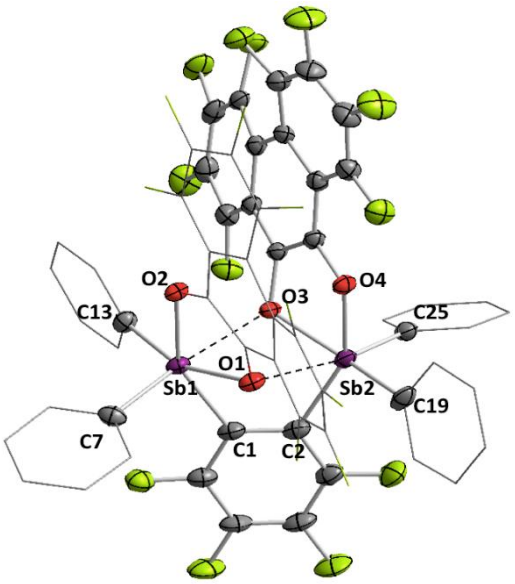

Figure 111.Structure of one of the two independent molecules in the solid-state structure of 1. Thermal ellipsoids are drawn at the 50 % probability level. The hydrogen atoms and toluene molecules are omitted for clarity. Selected bond lengths (Å) and angles (deg): isomer **61**. Sb1–Sb2 3.5690(7), Sb1–O3 2.4291(4), Sb2–O1 2.5725(5), O1–Sb1–O2 78.449(2), O3–Sb2–O4 78.374(2), Sb1–C1–C2 120.031(5), Sb2–C2–C1 120.055(6). Isomer 2: Sb1–Sb2 3.5969(7), Sb1–O3 2.4727(5), Sb2–O1 2.6432(5), O1–Sb1–O2 78.551(2), O3–Sb2–O4 78.479(2), Sb1–C1–C2 120.790(5), Sb2–C2–C1 120.696(6).

The solid-state structure of **61**, which contains two independent molecules in the asymmetric unit, confirms this view and is discussed hereafter, in direct comparison with that of **57**, its perprotio-*ortho*-phenylene analog, which was isolated and characterized by Masato Hirai. In both compounds, the Sb1–Sb2 separations are small with a value of 3.568(3) Å in **57**, and 3.5690(7) Å/3.5969(7) Å in **61**. These values are significantly smaller compared with those values in **56** and **60** (**56**: 3.7773(5) Å; **60**: 3.8176(8) Å), despite that the fact that fluorophenanthrene ligand is bulkier. We propose that this is due to π- π interaction between the fluorophenanthrene ligands as they are clearly bent towards each other. This attraction also induces some bending in the phenanthrene ligands. These

distortions result in short Sb-O separations, across the bidentate pocket. Indeed, **61** features short Sb1–O3 and Sb2–O1 distances of 2.4291(4) Å and 2.5725(5) Å, respectively, leading to an average value of 2.520 Å. This average value is slightly shorter than that in **57** (2.541 Å), suggesting that the antimony centers of **61** are more Lewis acidic. It is also interesting to note that these values are shorter than those in **60** (av. Sb···O = 2.8409 Å).

The geometry of **61** has been investigated computationally using DFT methods (B3LYP functional with the mixed basis sets: aug-cc-pVTZ-pp for Sb, 6-31g(d') for F, 6-31g for C, O and H). As expected, the LUMO is concentrated on both antimony(V) centers and has a high Sb–C_{Ph} σ^* character, as observed for **60** (Figure 112) The Sb–O interactions in complexes **57** and **61** have also been investigated using a natural bond orbital (NBO) analysis. This analysis reveals the presence of a $lp_{(O)} \rightarrow \sigma^*_{Sb-C}$ donor-acceptor interactions which, as indicated by deletion calculations, contributes E_{del} = 22.18 kcal mol^{-1} to the stability of **57** and E_{del} = 29.79 kcal mol^{-1} to the stability of **61** (Figure 113). The higher value in **61** also support the greater Lewis acidity of the Sb(V) centers in **61**.

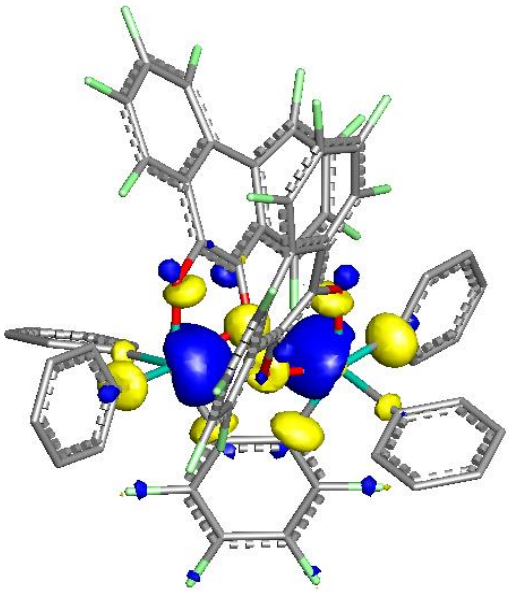

Figure 112. Contour plot of the LUMO of **61** (isovalue = 0.05).

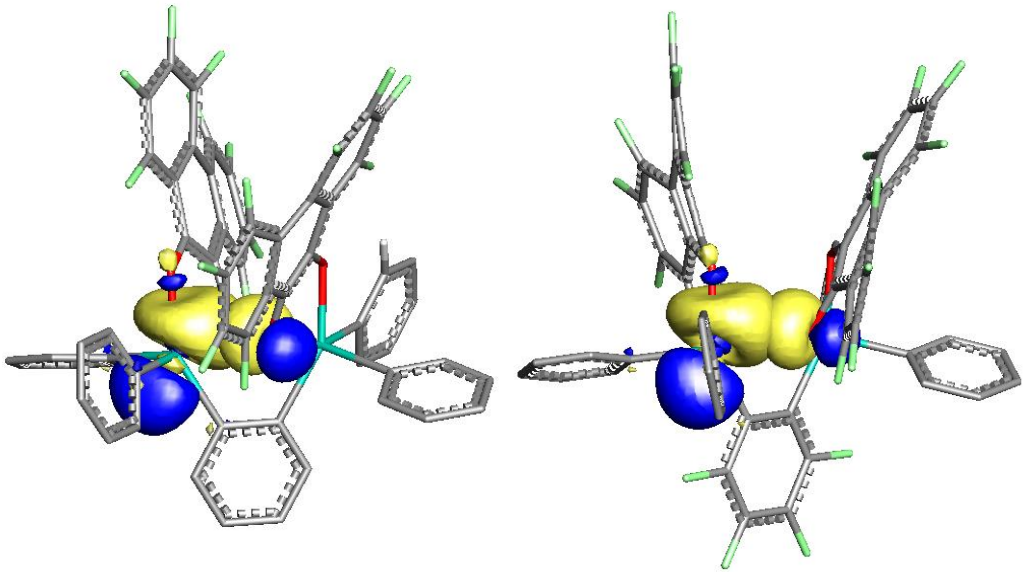

Figure 113. Left: Plot of the NBO $lp_{(O)} \rightarrow \sigma^*_{Sb-C}$ donor-acceptor interactions calculated for **57**. Right: Plot of the NBO $lp_{(O)} \rightarrow \sigma^*_{Sb-C}$ donor-acceptor interactions calculated for **61**. Density isovalues are set at 0.05, and hydrogen atoms have been omitted for clarity.

After full characterization of complex **61**, we wanted to investigate how the Sb–O interactions would affect its fluoride ion affinities. Towards this end, **61** was treated with TBAT in CH_2Cl_2 at ambient temperature (Figure 114). After stirring for 30 min, the solvent was removed in vacuo to afford an orange oil, which was washed with a large amount of pentane. This procedure afforded TBA[**61**–F] as yellow solid in 80% yield. The ^{1}H NMR spectrum of this anionic complex shows that the resonances of the aryl rings in TBA[**61**–F] are significantly sharpened compared to those of the free distiborane **61** and that all four phenyl rings are equivalent in solution. In the ^{19}F NMR spectrum of TBA[**61**–F], nine distinct resonances are found between -115 and -170 ppm, corresponding to the perfluorophenanthrenediyl–9,10–dioxy ligand and the tetrafluorobenzene backbone. The fluoride ion appears at -77.09 ppm in $CDCl_3$.

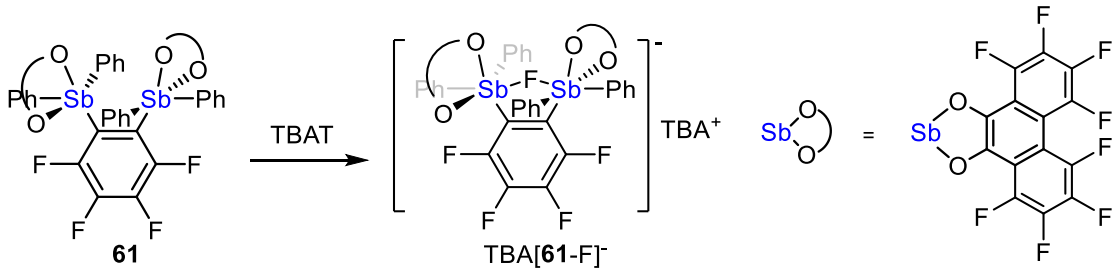

Figure 114. Synthesis of TBA[**61–**F].

Single crystals of TBA[**61**–F] were obtained by diffusion of pentane into a saturated dichloromethane solution of the salt (Figure 115). The solid-state structure was obtained by X-ray crystallography. The structure confirms that the fluoride is tightly bound to both antimony centers in a chelating fashion. In both TBA[**57**–F] and TBA[**61**–

F], the perfluorophenanthrenediyl–9,10–dioxy ligands are clamping down on the bridging fluoride, thus indicating the flexibility of such ligands. The Sb1–Sb2 separation in TBA[**57**–F] and TBA[**61**–F] are 3.8084(1) Å and 3.8525(6) Å, respectively. These values are slightly shorter than those in their *o*–chloranil analogues (TBA[**56**–F]: 3.8569(5) Å; TBA[**60**–F]: 3.8643(2) Å) despite the fact that the perfluorophenanthrene ligand is bulkier. The bridging fluoride adopts a bent geometry with a Sb1–F100–Sb2 angle of 126.27(2)^{o} in TBA[**57**–F] and a Sb1–F1–Sb2 angle of 129.48(6)^{o} in TBA[**61**–F].

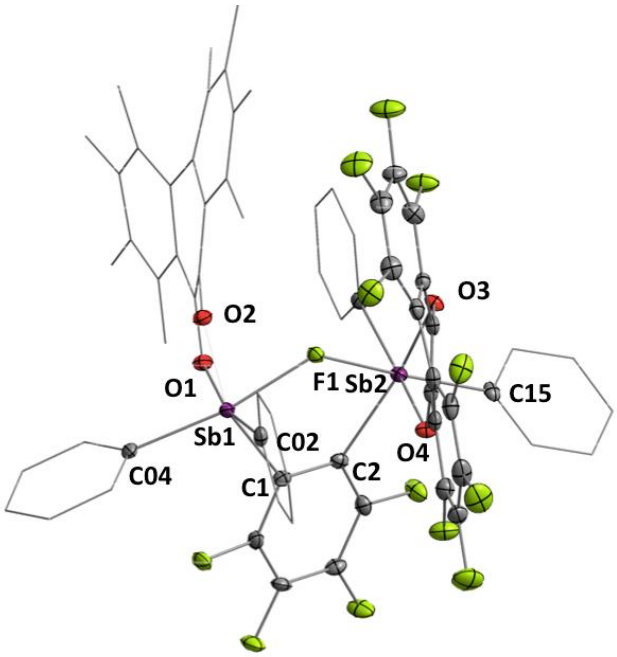

Figure 115. Crystal structure of [TBA][**61**–F]. Thermal ellipsoids are drawn at the 50 % probability level. The hydrogen atoms and the TBA cation are omitted for clarity. Selected bond lengths (Å) and angles (deg) in [TBA][**61**–F]: Sb1–Sb2 3.8525(6), Sb1–C1 2.1824(2), Sb1–C04 2.1430(2), Sb1–O1 2.0516(1), Sb1–O2 2.0614(1), Sb2–C2 2.1853(2), Sb2–C40 2.1344(2), Sb2–O3 2.0658(1), Sb2–O4 2.0570(1), Sb1–F–Sb2 129.48(6), O1–Sb1–O2 78.940(6), O3–Sb2–O4 79.190(5), F1–Sb1–C04 169.979(7), F1–Sb2–C15 170.314(7).

We have also estimated the FIA of **57** and **61** using DFT methods. The optimization and frequency calculation have been carried out at the B3LYP functional with the mixed basis sets: aug-cc-pVTZ-pp for Sb, 6-31g(d') for F, 6-31g for C, O and H. Subsequently, enthalpies have been determined by a single point calculation at the DFT optimized structure applying the B3LYP functional and aug-cc-pVTZ-pp level of theory on Sb and 6-311+g(2d, p) level of theory on C, H, O, and F. The results show that the FIA of **57** (388.1 kJ mol^{-1}) is marginally higher than that of **56**. That of **61** (396.3 kJ mol^{-1}) is the highest among the four stiboranes discussed so far.

Next, we wanted to compare the fluoride anion affinity to their 9,9–dimethylxanthene analogue. To this end, we studied the reaction of [**58**]$^-$ with an equimolar amount of **61** in THF. Unfortunately, no exchange of the fluoride anion occurred over 30 min. The reason is likely due to the Sb–O interaction in **61** that imposes a high energy barrier for the fluoride exchange reaction. To test this hypothesis, we treated a 1:1 mixture of **57** and **61** with 1 equivalent of TBAT in THF and found that the major product is TBA[**57**–F], even if **61** possess a higher FIA by calculation. Next, we performed a reverse competition experiment as descried in section 5.3. We treated a 1:1 mixture of TBA[**57**–F] and TBA[**61**–F] in THF with $Al(NO_3)_3$. Upon incremental addition of $Al(NO_3)_3$, we observed that the ^{19}F NMR resonance signal corresponding to the bridging fluoride in TBA[**57**–F] disappeared completely while that of TBA[**61**–F] remained intact. Further addition of $Al(NO_3)_3$ led to the disappearance of TBA[**61**–F] signals. The corresponding ^{19}F NMR spectra are shown in Figure 116. This experiment indeed suggests that **61** has a higher fluoride ion affinity than **57**. However, the decomplexation of fluoride

ion is accompanied by decomposition of the free distiboranes. As a result, this fluoride decomplexation chemistry is not reversible.

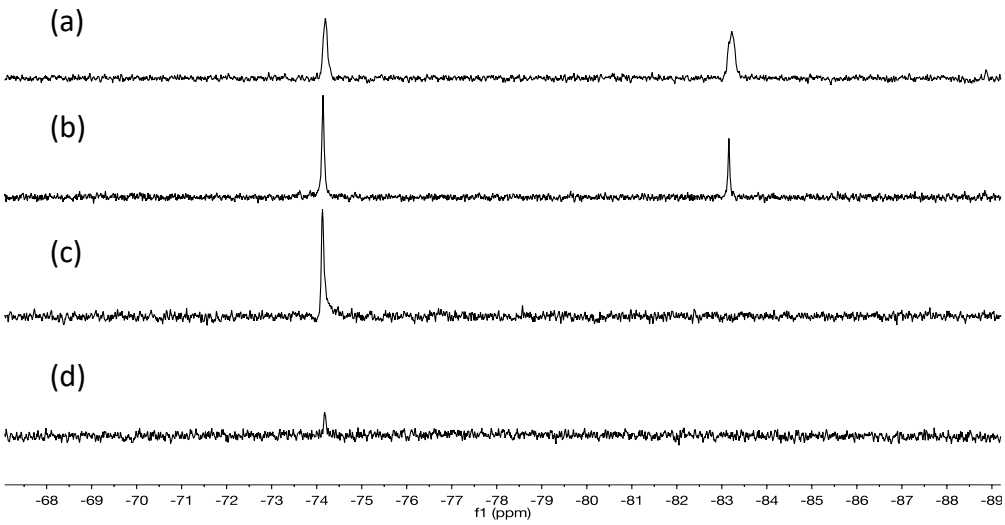

Figure 116. a) 1:1 mixture of TBA**[57**–F] and TBA[**61**–F] in THF; b) Reaction with 0.5 equiv $Al(NO_3)_3$; c) Reaction with 1 equiv $Al(NO_3)_3$; d) Reaction with 2 equiv $Al(NO_3)_3$ in 5min.

5.5 Synthesis and properties of a distiboranes obtained by oxidation of the distibines 56 and 59 with phenanthrenequinone

We have also used commercially available phenanthrenequinone to generate distiboranes. Compound **62** was generated by treatment of **56** with 2 equivalents of phenanthrenequinone under N_2 atmosphere. The compound precipitates as a yellow, insoluble solid that has very poor solubility in common organic solvents, preventing its characterization by NMR spectroscopy. Single crystals of **62** were obtained by carefully

layering a CH_2Cl_2 solution of phenanthrenequinone with a CH_2Cl_2 solution of **56** under an N_2 atmosphere.

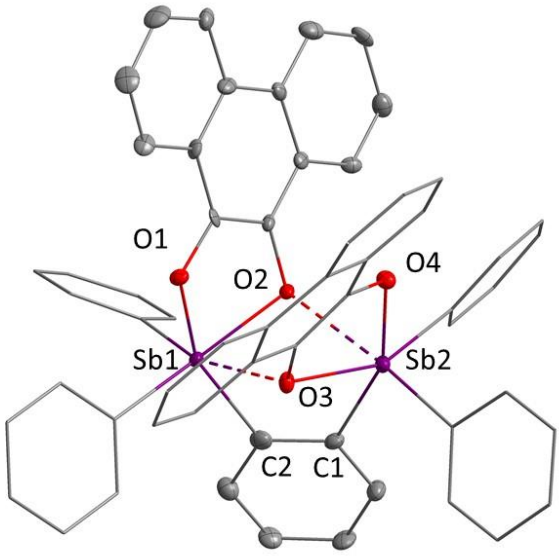

Figure 117. Structure of one of the two independent molecules in the solid-state structure of **62**. Thermal ellipsoids are drawn at the 50 % probability level. The hydrogen atoms and solvents are omitted for clarity. Selected bond lengths (Å) and angles (deg) in **62**: Sb1–Sb2 3.507(5), Sb1–O1 2.018(5), Sb1–O2 2.150(5), Sb2–O3 2.153(5), Sb2–O4 2.009(4), Sb1–O3 2.462(5), Sb2–O2 2.446(5), O1–Sb1–O2 79.11(18), O3–Sb2–O4 79.35(18), Sb1–C2–C1 119.3(5), Sb2–C1–C2 120.4(7). The other independent molecule features similar metrical parameters.

Complex **62** crystallizes with two independent molecules in the asymmetric unit (Figure 117). Because these two molecules are very similar, the structure of only one of them is discussed here. The Sb1–Sb2 separation in this molecule is small with a value of 3.507(5) Å. This value is significantly smaller than those in **56** (3.7773(5) Å) and **57** (3.568(3) Å). The Sb and neighboring O distance is short with a value of 2.462(5) Å for the Sb1–O3 distance and 2.446(5) Å for the Sb2–O2 distance. These values are well

below the van der Waals radii of the two elements and they are significantly smaller than those in **56**. The Sb2–C1–C2 (120.4(7)^{o}) and Sb1–C2–C1 (119.3(5)^{o}) angles are close to the ideal value of 120 ^{o}. Complex **62** was treated with TBAT in CH_2Cl_2 at ambient temperature under N_2. A new peak emerged at -70.1 ppm in the ^{19}F NMR spectrum within 5 min indicating the formation of a fluoride adduct. However, this adduct quickly decomposed when exposed to air.

Realizing the fluoride adduct of **62** may be difficult to isolate, we turned our attention to compound **59**. To a stirred solution of **59** in CH_2Cl_2 (2 mL) was added a solution of phenanthrenequinone in CH_2Cl_2 dropwise under N_2. Stirring for 30 min resulted in a yellow precipitate of the product **63** which was isolated by filtration. The ^{19}F NMR spectrum shows two distinct signals at -124.37 and -152.71 ppm corresponding to the fluoro–*ortho*–phenylene backbone. The ^{1}H NMR spectrum features eleven distinct signals, thus indicating that the hydrogen atoms on the phenanthrene moiety are inequivalent.

Single crystals of **63** were obtained as yellow needles by slow evaporation of a CH_2Cl_2 solution of 9,10–phenanthrenequinone and **59** at -20^{o}C. The structure was determined by X-ray diffraction analysis. In the solid-state, the antimony centers adopt a distorted square-pyramidal geometry (Figure 118). The Sb1–Sb2 separation is small with a value of 3.513(4) Å. The Sb1–O3 (2.444(4) Å) and Sb2-O2 (2.448(4) Å) distances are well below the sum of van der Waals radii of the two elements indicating the presence of an interaction. These distances are significantly smaller than those in **60**, which have the value around 2.8 Å. The formation of these short distances is consistent with the higher

basicity of the oxygen atoms resulting from the presence of a non-fluorinated phenanthrene back bone. The fluorinated phenylene backbone and the resulting higher Lewis acidity of the antimony centers also plays a role. The Sb2–C1–C2 and Sb1–C2–C1 angles are 119.7(5)^{o} and 119.3(5)^{o}, respectively, which are close to the ideal value of 120 ^{o}.

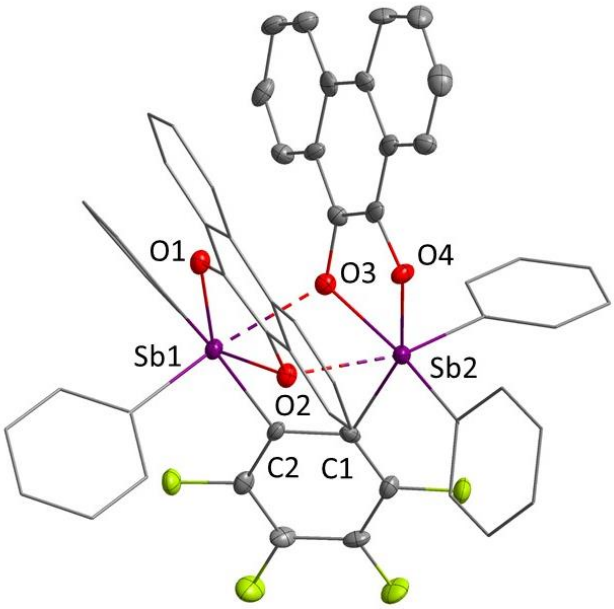

Figure 118. Structure of one of the two independent molecules in the solid-state structure of **63**. Thermal ellipsoids are drawn at the 50 % probability level. The hydrogen atoms and solvents are omitted for clarity. Selected bond lengths (Å) and angles (deg) in **63**: Sb1–Sb2 3.513(4), Sb1–O1 2.000(5), Sb1–O2 2.128(4), Sb2–O3 2.131(4), Sb2–O4 2.008(4), Sb1–O3 2.444(4), Sb2–O2 2.448(4), O1–Sb1–O2 80.77(17), O3–Sb2–O4 80.16(17), Sb1–C2–C1 119.3(5), Sb2–C1–C2 119.7(5).

Next, I decided to study the anion binding properties of **63** towards fluoride. Complex **63** was treated with TBAT in CH_2Cl_2. To a solution of **63** in dichloromethane was added a solution of TBAT in dichloromethane. After stirring for 10 min, the mixture

was clear yellow. The solvent was then removed in vacuo to afford TBA[**63**–F] as a green yellow solid. The ^{19}F NMR spectrum shows three resonance signals -63.79, -121.80, -157.61 ppm, respectively in a 1: 2: 2 ratio. The ^{1}H NMR spectrum features ten distinct signals, thus indicating that the hydrogen atoms on the phenanthrene moiety are inequivalent.

5.6 Conclusion

The results in this chapter show that the use of the perfluro–*ortho*–phenylene backbone can be used to access highly Lewis acidic distiboranes. Although these distiboranes readily complex fluoride anions, their lack of solubility or their instability has prevented an unambiguous clarification of their anion affinity. Nevertheless, the results I have obtained have allowed me to identify particularly promising scaffold that maximize anion chelation. These include distiborane **61** whose exterior is fully fluorinated.

5.7 Experimental

General considerations: Antimony is potentially toxic and should be handled with caution. Perfluoro(tetradecahydrophenanthrene) was purchased from Beantown Chemical and used as received. *n*–BuLi (2.65 M in hexane) was purchased from Alfa Aesar and used as received. Tetrachloro–*o*–benzoquinone (*o*–chloranil) was purchased from Acros Organics. TBAT was purchased from TCI and used as received. Ph_2SbCl,[230] $PhICl_2$,[231] was prepared by following or modifying previously reported procedure from literature. All preparations were carried out under an atmosphere of dry N_2 employing either a glovebox or standard Schlenk techniques unless specified. Solvents were dried by

passing through an alumina column (pentane and CH_2Cl_2) or by refluxing under N_2 over Na/K (hexanes, Et_2O, and THF). All other solvents were ACS reagent grade and used as received. NMR spectra were recorded on a Varian Unity Inova 400 FT NMR (399.508 MHz for ^1H, 100.466 MHz for ^{13}C) or Varian Unity Inova 500 FT NMR (499.42 MHz for ^1H, 469.86 MHz for ^{19}F, 125.60 MHz for ^{13}C) spectrometer at ambient temperature. ^1H and ^{13}C NMR chemical shifts are given in ppm and are referenced against $SiMe_4$ using residual solvent signals used as secondary standards. ^{19}F NMR chemical shifts are given in ppm and are referenced against $CFCl_3$ using BF_3–Et_2O as an external secondary standard with δ -153.0 ppm. Elemental analyses (EA) were performed at Atlantic Microlab (Norcross, GA).

Computational Details: Density functional theory (DFT) structural optimizations with the Gaussian 09 program.208 In all cases, the structures were optimized using the B3LYP functional;209, 210, and the following mixed basis set: Sb, aug-cc-pVTZ-PP;240 Cl, 6-311+g(d); F, 6-31g(d');212 C/O/H, 6-31g. For all optimized structures, frequency calculations were carried out to confirm the absence of imaginary frequencies. The molecular orbitals were visualized and plotted in Jimp 2 program.[170]

Crystallographic measurements: The crystallographic measurements were performed at 110(2) K using a Bruker APEX-II CCD area detector diffractometer, with a 194 graphite-mono chromated Mo-Kα radiation (λ = 0.71069 A). A specimen of suitable size and quality was selected and mounted onto a nylon loop. The semi-empirical method SADABS was applied for absorption correction. The structure was solved by direct methods, which successfully located most of the non-hydrogen atoms. Subsequent

refinement on F2 using the SHELXTL/PC package (version 6.1) allowed location of the remaining non-hydrogen atoms. All H-atoms were geometrically placed and refined using a standard riding model.

Synthesis of 59: A solution of *n*–BuLi in hexane (3.5 mL, 2.2 M, 7.73 mmol) was added dropwise to a solution of 1, 2–dibromotetrafluorobenzene (0.9951 g, 3.22 mmol) in THF (20 mL) at -78 °C. After stirring at this temperature for 45 min, a suspension of Ph_2SbCl (1.9960 g, 6.44 mmol) in THF (10 mL) was transferred with a cannula to the solution. The solution was slowly warmed up to ambient temperature and stirred for an additional 12 h. The solvent was removed in vacuo and CH_2Cl_2 (30 mL) was added to the residue. The solution was then filtered through Celite. The solvent of the filtrate was removed in vacuo and resulted in yellow oily product which was isolated with silica gel column in hexane. Removal of hexane gave white crystalline solid (1.41g, 62.3%). Single crystals of $(C_6F_4)Sb_2Ph_4$ suitable for X-ray diffraction were obtained by a hexane solution of the compound to stand at room temperature overnight. ^{1}H NMR (499.42 MHz, $CDCl_3$): δ 7.30-7.34 (m, 12H, *p*–Sb*Ph*, *o*–Sb*Ph*), δ=7.46 ppm (m, 8H, *m*–Sb*Ph*), $^{13}C\{^1H\}$ NMR (125.60 MHz, $CDCl_3$): δ 149.52-151.57 (dm, $^1J_{C-F}$=260.9 Hz),139.64-142.04 (dm, $^1J_{C-F}$ = 257.0 Hz), 137.63, 136.13, 129.00, 128.92 ppm. ^{19}F NMR (469.86 MHz, $CDCl_3$): δ -113.99 (d, $^3J_{F-F}$ = 18.3Hz), -153.42 ppm (d, 2F, $^3J_{F-F}$=18.3 Hz). Elemental analysis calculated (%) for **59**: C, 51.48; H, 2.88; found C, 51.27; H, 3.00.

Synthesis of 60: To a stirred solution of $(C_6F_4)Sb_2Ph_4$ (50.2 mg, 0.072 mmol) in CH_2Cl_2. (2 mL) was added a solution of *o*–chloranil (35.3 mg, 0.14 mmol) in CH_2Cl_2 (2 mL) dropwise over 5 min. Stirring for 30 min resulted in yellow precipitate which was

isolated through filtration to afford the product as yellow solid (79.5 mg, 93%). Single crystals were obtained as yellow blocks by layering a diethyl ether solution of *o*–chloranil with a CH_2Cl_2 solution of $(C_6F_4)Sb_2Ph_4$ at ambient temperature. ^{1}H NMR and ^{13}C NMR cannot be obtained due to the poor solubility of this complex. ^{19}F NMR (469.86 MHz, collect in the process of the reaction): δ -120.59 (d, 2F, $^3J_{F–F}$ = 16.3Hz), -149.41 ppm (d, 2F, $^3J_{F–F}$ = 16.1Hz). Elemental analysis calculated (%) for $C_{42}H_{20}Cl_8F_4O_4Sb_2 \cdot CH_2Cl_2$: C, 40.45; H, 1.74, Cl, 27.77; found C, 40.66; H, 1.84; Cl, 27.39.

Synthesis of TBA[60–F]: To a suspension of **60** (87.8 mg, 0.074 mol) in dichloromethane (3 mL) was added a solution of TBAT (39.8 g, 0.074mol) in dichloromethane (3 mL). After stirring for 30 min, the mixture was clear. Removal of the solvent in vacuo afforded TBA[**60**–F] as a white solid which was washed with two portions of Et_2O (3 mL each), resulting in white solid (116.9mg, 91.8%). Single crystals of TBA[**60**–F] were obtained as colorless blocks by slow diffusion of pentane into a CH_2Cl_2 solution of the compound at ambient temperature. ^{1}H NMR (499.42 MHz, $CDCl_3$): δ 8.06 (d, 4H, $^3J_{H–H}$ = 6.62 Hz, *o*–Sb*Ph*), 7.43 (m, 6H, $^3J_{H–H}$ = 6.77 Hz, Sb*Ph*), 7.31 (d, 4H, $^3J_{H–H}$ = 7.28 Hz, Sb*Ph*), 7.21 (pseudo t, 2H, $^3J_{H–H}$ = 7.28 Hz, *p*–Sb*Ph*), 7.16 (t, 4H, $^3J_{H–H}$ = 7.28 Hz, Sb*Ph*), 2.72 (pseudo t, 8H, $^3J_{H–H}$ = 8.72 Hz, TBA–CH_2), 1.34 (broad, 8H, TBA–CH_2), 1.07 (q, 8H, $^3J_{H–H}$ = 7.54 Hz, TBA–CH_2), 0.85 ppm (t, 12H, $^3J_{H–H}$ = 7.24 Hz, TBA–CH_3). ^{13}C{^{1}H} NMR (125.60 MHz, $CDCl_3$): 146.19, 145.96, 132.88, 130.08, 129.25, 128.72, 128.27, 118.74, 117.91, 115.14, 65.88(TBA), 59.23(TBA), 24.11(TBA), 19.66 (TBA) ppm. ^{19}F NMR (469.86 MHz, $CDCl_3$): δ -68.04 (s, 1F), -119.59

(d, 2F, $^{3}J_{F-F}$=18.3Hz), -154.43 ppm (d, 2F, $^{3}J_{F-F}$ =16.9Hz). Elemental analysis calculated (%) for $C_{58}H_{56}Cl_8F_5NO_4Sb_2$: C, 47.94; H, 3.88; N, 0.96; found C, 48.21; H, 4.01; N, 1.08.

Synthesis of 61: To a stirred solution of $(C_6F_4)Sb_2Ph_4$ (78.0 mg, 0.11 mmol) in CH_2Cl_2 (2mL) was added a solution of octafluorophenthra–9,10–quinone (78.4 mg, 0.22 mmol) in CH_2Cl_2 (2 mL) dropwise. The solvent was removed in vacuo after stirring for 30 min and washed with 2 portions (2 ml each) of Et_2O and 2ml of pentane to afford the product as yellow solid in 69% yield (107.9 mg, 0.077 mol). Single crystals were obtained by slow evaporation of a CH_2Cl_2 solution. ^{1}H NMR (499.42 MHz, $CDCl_3$): δ 7.94 (d, 4H, $^{3}J_{H-H}$ =7.72 Hz), 7.73 (t, 2H, $^{3}J_{H-H}$ = 7.41 Hz), 7.59 (t, 4H, $^{3}J_{H-H}$ = 7.41 Hz), 7.40 (d, 4H, $^{3}J_{H-H}$ =8.40 Hz), 7.29 (t, 2H, $^{3}J_{H-H}$ =7.77 Hz), 7.20ppm (t, 4H, $^{3}J_{H-H}$ =7.82 Hz). ^{13}C{^{1}H} NMR (125.60 MHz, $CDCl_3$): 137.00, 135.28, 134.44, 132.98, 132.38, 131.71, 129.70, 129.43ppm. ^{19}F{^{1}H} NMR (469.86 MHz, CH_2Cl_2): -119.28 (s, 2F), -129.00 (pseudo q, 4F), -141.71 (s, 2F), -146.02 (s, 2F), -147.83 (s, 2F), -156.47 (s, 2F), -157.20 (s, 2F), -160.20 (s, 2F), -160.97ppm (s, 2F). Elemental analysis calculated (%) for $C_{58}H_{20}F_{20}O_4Sb_2$: C, 49.61; H, 1.44; found C, 49.87; H, 1.64.

Synthesis of TBA[61–F]: To a solution of **61** (58 mg, 0.041 mmol) in dichloromethane (1 mL) was added a solution of TBAT (22 mg, 0.041 mmol) in dichloromethane (2 mL). After stirring for 30 min, the solvent was removed *in vacuo*. The orange oil was washed with a large amount of pentane. This procedure afforded TBA[**61**–F] in 80% yield (63 mg, 0.033 mol). Single crystals of TBA[**61**–F] were obtained by diffusion of pentane into a saturated dichloromethane solution. ^{1}H NMR (499.42 MHz, $CDCl_3$): δ 7.64 (d, 4H, J_{H-H}=7.72 Hz), 7.40 (d, 4H, $^{3}J_{H-H}$=7.17 Hz), 7.13 (m, 6H), 6.91 (t,

4H, $^{3}J_{H–H}$=7.17 Hz), 6.82 (t, 2H, $^{3}J_{H–H}$=7.87 Hz), δ=2.72 (pseudo t, 8H, TBA–CH_2), 1.27 (broad, 8H, TBA–CH_2), 1.13 (m, 8H, TBA–CH_2), 0.82 ppm(t, 12H, $^{3}J_{H–H}$=7.45 Hz, TBA–CH_3). $^{13}C\{^{1}H\}$ NMR (125.60 MHz, CD_2Cl_2): 134.87, 133.12, 132.65, 128.81, 128.41, 128.06, 127.80, 127.54, 58.88, 23.76, 10.62,13.25ppm. $^{19}F\{^{1}H\}$ NMR (469.86 MHz, $CDCl_3$): -77.09 (s, 1F), -117.48 (s, 2F), -131.71 (pseudo q, 4F), -144.61 (s, 2F), -148.13 (s, 2F), -152.79 (s, 2F), -160.00 (s, 4F), -165.34(s, 2F), -165.66ppm (s, 2F). Elemental analysis calculated (%) for $C_{74}H_{56}F_{21}NO_4Sb_2$: C, 53.36; H, 3.39; N, 0.84; found C, 53.62; H, 3.53; N, 0.99.

Synthesis of 63: To a stirred solution of $(C_6F_4)Sb_2Ph_4$ (80.4 mg, 0.115 mol) in CH_2Cl_2 (2 mL) was added a solution of 9,10–phenanthrenequinone (47.8 mg, 0.23 mol) in CH_2Cl_2 (2 mL) dropwise in a glovebox. Stirring for 30 min resulted in yellow precipitate which was isolated through filtration and washed with 3 portions of Et_2O to afford the product as yellow solid in 86% yield (109.9 mg, 0.099 mol). Single crystals were obtained as yellow needles by slow evaporation of CH_2Cl_2 solution of 9,10–phenanthrenequinone and $(C_6F_4)Sb_2Ph_4$ at -20^{o}C. ^{1}H NMR (499.42 MHz, $CDCl_3$): δ 8.29 (d, 2H, $J_{H–H}$ = 8.59 Hz), 8.03 (d, 6H, $^{3}J_{H–H}$ = 8.73 Hz), 7.82 (t, 2H, $^{3}J_{H–H}$ = 8.59 Hz), 7.70 (t, 4H, $^{3}J_{H–H}$ = 7.60 Hz), 7.45 (d, 4H, $^{3}J_{H–H}$ = 7.60 Hz), 7.19 (mt, 4H, $^{3}J_{H–H}$ = 7.56 Hz), 7.10 (t, 4H, $^{3}J_{H–H}$ = 7.49 Hz), 6.95 (dt, 2H, $^{3}J_{H–H}$ = 8.20 Hz), 6.90 (d, 2H, $^{3}J_{H–H}$=8.60 Hz), 6.81 (t, 2H, $^{3}J_{H–H}$ = 8.51 Hz), 6.73-6.71ppm (m, 4H). $^{13}C\{^{1}H\}$ NMR (125.60 MHz, $CDCl_3$): 139.98, 137.29, 135.63, 135.36, 134.01, 132.13, 130.62, 129.89, 129.01, 127.99, 125.87, 124.74, 123.97, 123.83, 123.73, 123.50, 122.35, 120.91, 120.41, 119.97 ppm. $^{19}F\{^{1}H\}$ NMR (469.86

MHz, $CDCl_3$): -124.37 (s, 2F), -152.71ppm (s, 2F). Elemental analysis calculated (%) for $C_{42}H_{20}Cl_8F_4O_4Sb_2$: C, 62.40; H, 3.25; found C, 61.80; H, 3.77.

Synthesis of TBA[63–F]: To a solution of **63** (68.0 mg, 0.061 mmol) in dichloromethane (2 mL) was added a solution of TBAT (32.8 mg, 0.061 mmol) in dichloromethane (2 mL). After stirring for 10 min, the mixture was clear yellow. 4h late the solvent was removed in vacuo to afford TBA[**63**–F] as a green yellow solid which was washed with three portions of Et_2O (3 mL each), resulting in green yellow solid (63.0 mg, 62.5%). ^{1}H NMR (499.42 MHz, $CDCl_3$): δ 8.48 (m, 4H), 8.29 (d, 4H, $^3J_{H–H}$ = 7.29 Hz), 8.07 (d, 2H, $^3J_{H–H}$ = 7.62 Hz), 7.85 (d, 2H, $^3J_{H–H}$ = 8.40 Hz), 7.53 (t, 2H, $^3J_{H–H}$ = 7.52 Hz), 7.37 (m, 6H), 7.25 (d, 2H, $^3J_{H–H}$ = 7.49 Hz), 7.20 (t, 2H, $^3J_{H–H}$ = 6.53 Hz), 7.09 (t, 4H, $^3J_{H–H}$ = 7.20 Hz), 7.02 (q, 4H), 6.95 (t, 4H, $^3J_{H–H}$ = 7.29 Hz), 2.09 (t, 8H, $^3J_{H–H}$ = 7.19 Hz), 0.70-0.60 (m, 16H), 0.51ppm(t, 12H, $J_{H–H}$ = 7.27 Hz). ^{13}C{^{1}H} NMR (125.60 MHz, $CDCl_3$): 138.6, 137.58, 134.97, 133.04, 129.21, 128.28, 128.14, 127.69, 127.03, 126.92, 125.36, 124.57, 124.24, 123.04, 122.49, 121.95, 121.76, 121.33, 121.24, 59.35, 24.21, 19.31, 13.39 ppm. ^{19}F{^{1}H} NMR (469.86 MHz, $CDCl_3$): -63.79 (s, F), -121.80 (d, 2F, $^3J_{F–F}$ = 18.08 Hz), -157.61ppm (d, 2F, $^3J_{F–F}$=19.04 Hz). Elemental analysis calculated (%) for $C_{74}H_{72}F_5NO_4Sb_2$: C, 64.50; H, 5.27, N, 1.02; Found C, 64.04, H, 5.72, N, 0.96.

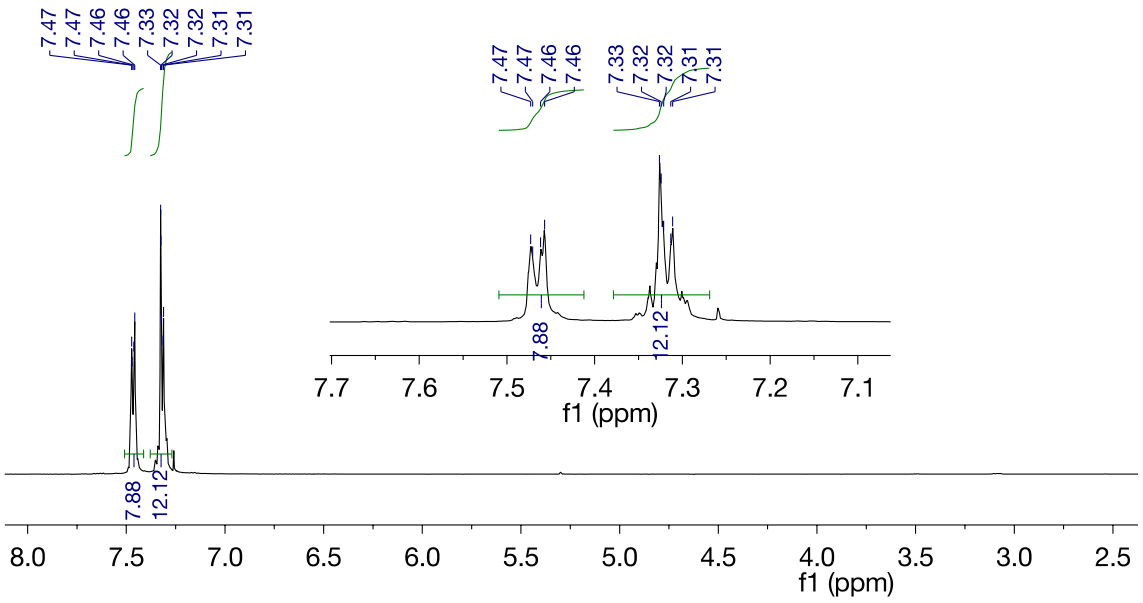

Figure 119. ^{1}H NMR spectra of **59** in $CDCl_3$

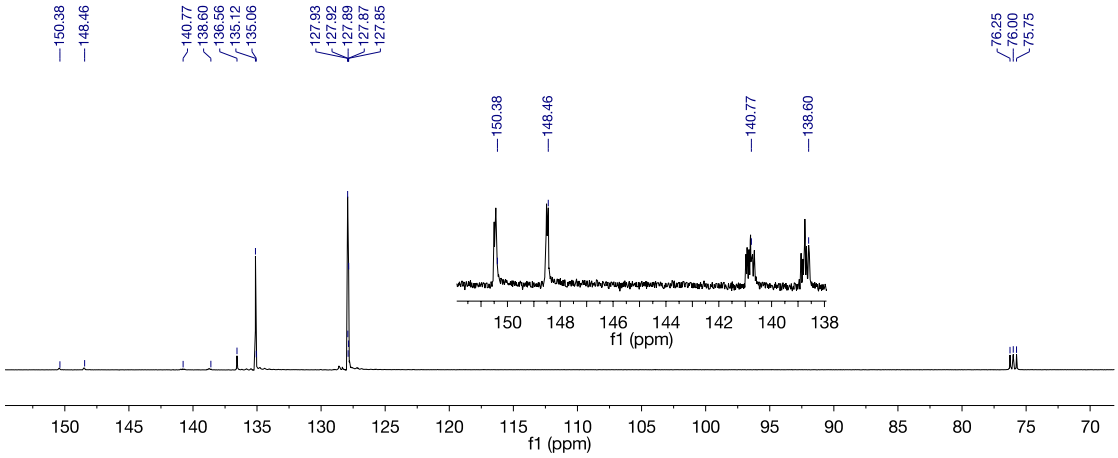

Figure 120. ^{13}C NMR spectra of **59** in $CDCl_3$.

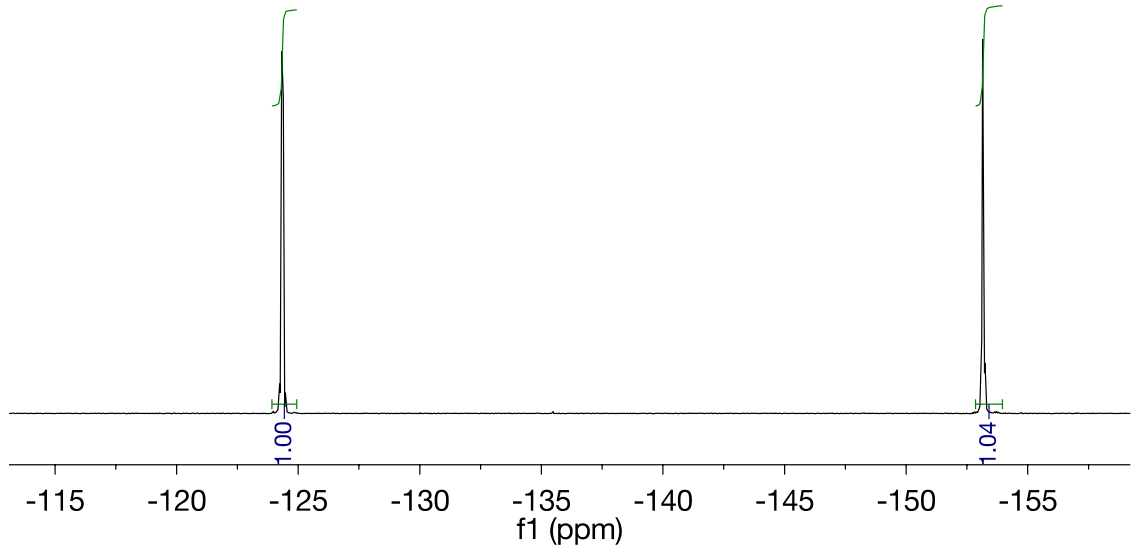

Figure 121. ^{19}F NMR spectra of **59** in $CDCl_3$

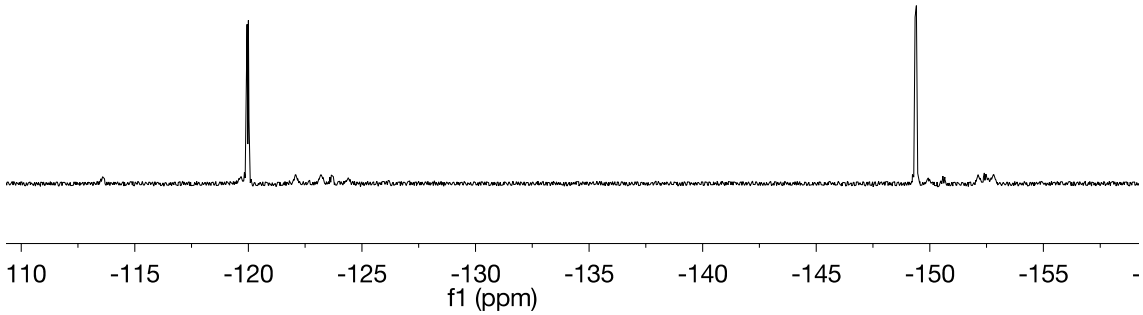

Figure 122. ^{19}F NMR spectra of **60** in $CDCl_3$

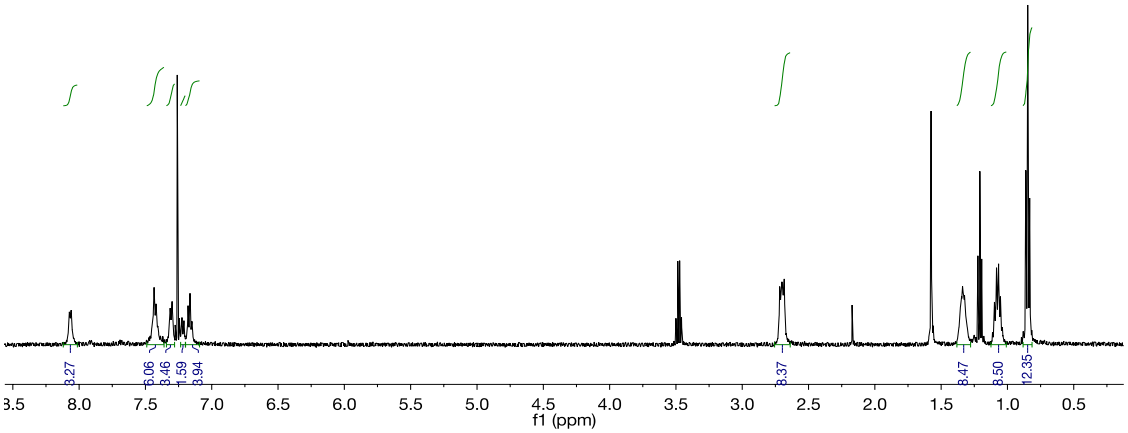

Figure 123. ^{1}H NMR spectra of TBA[**60**–F] in $CDCl_3$.

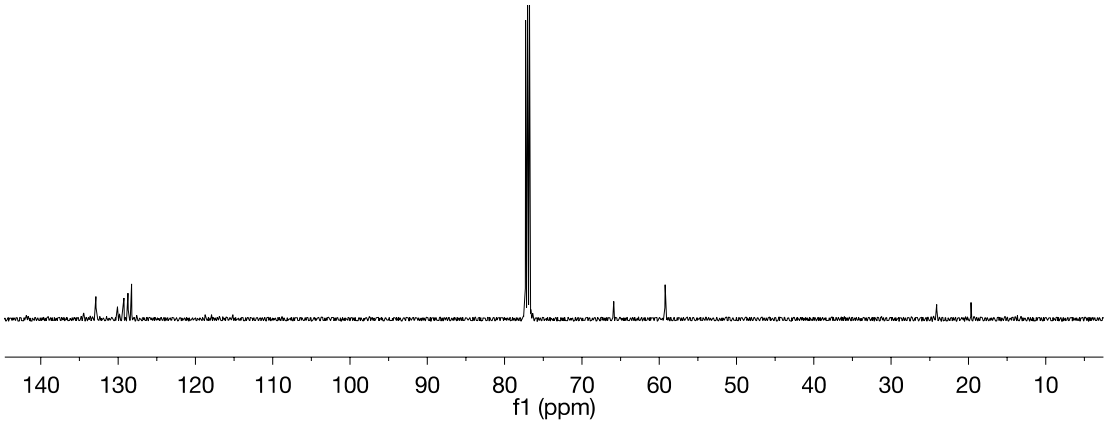

Figure 124. ^{13}C NMR spectra of TBA[**60**–F] in $CDCl_3$.

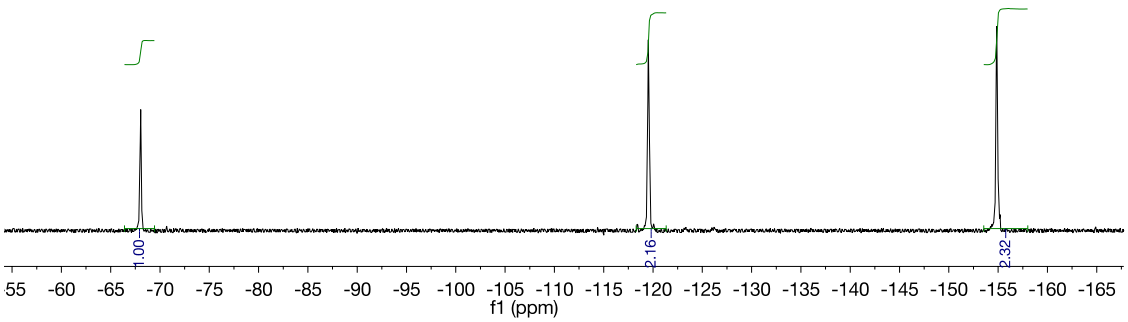

Figure 125. ^{19}F NMR spectra of TBA[**60**–F] in $CDCl_3$.

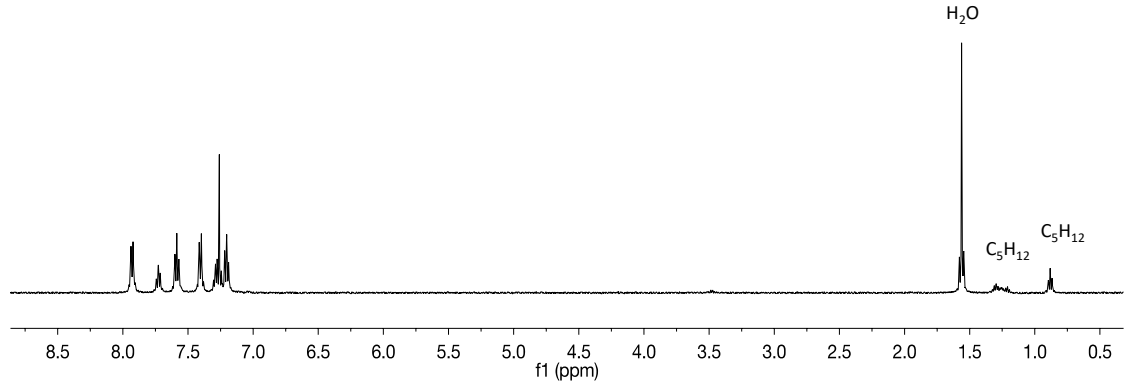

Figure 126. ^{1}H NMR spectra of **61** in $CDCl_3$.

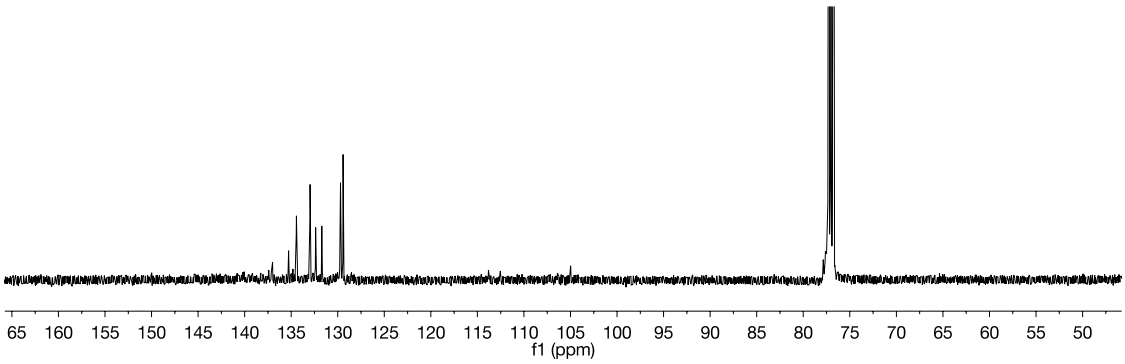

Figure 127. ^{13}C NMR spectra of **61** in $CDCl_3$.

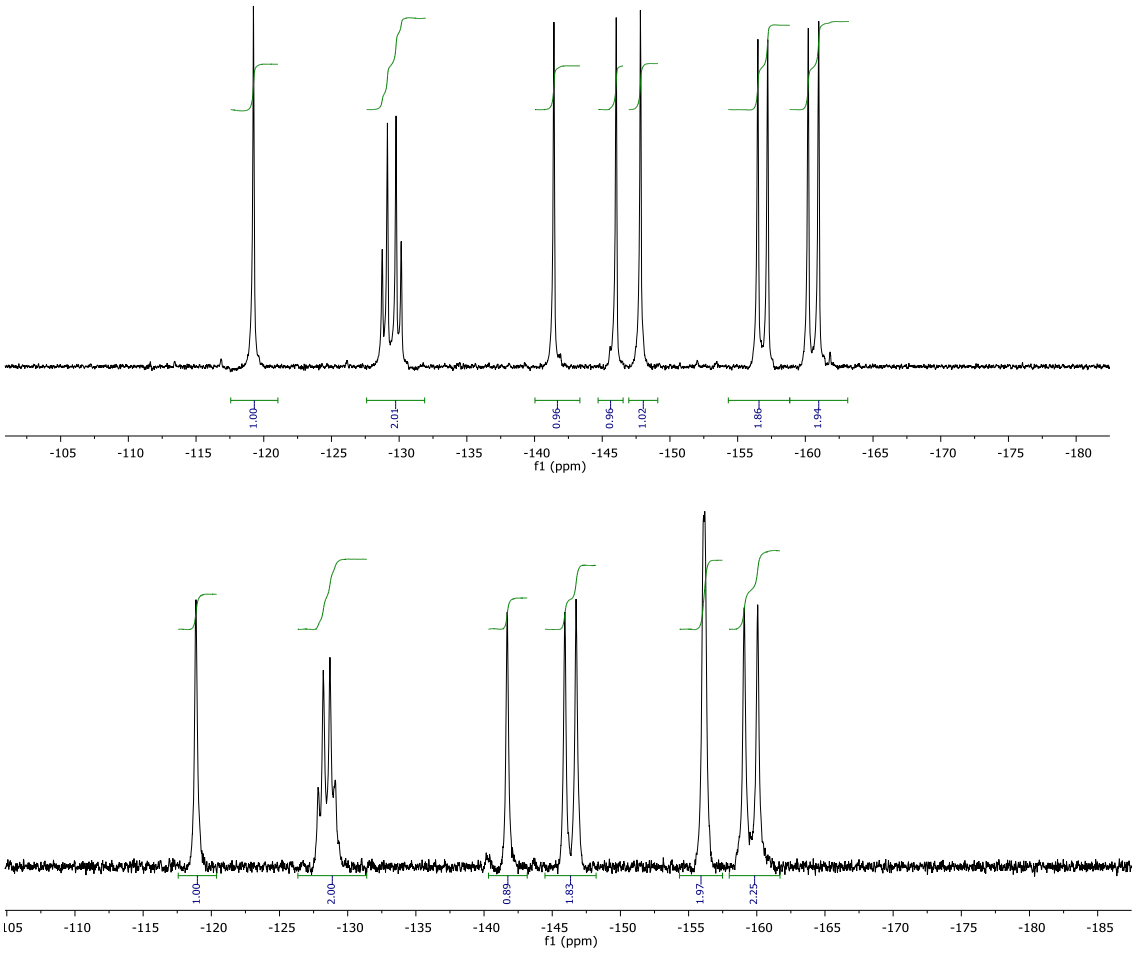

Figure 128. ^{19}F NMR spectra of **61** in CH_2Cl_2 (top) and in $CDCl_3$ (bottom).

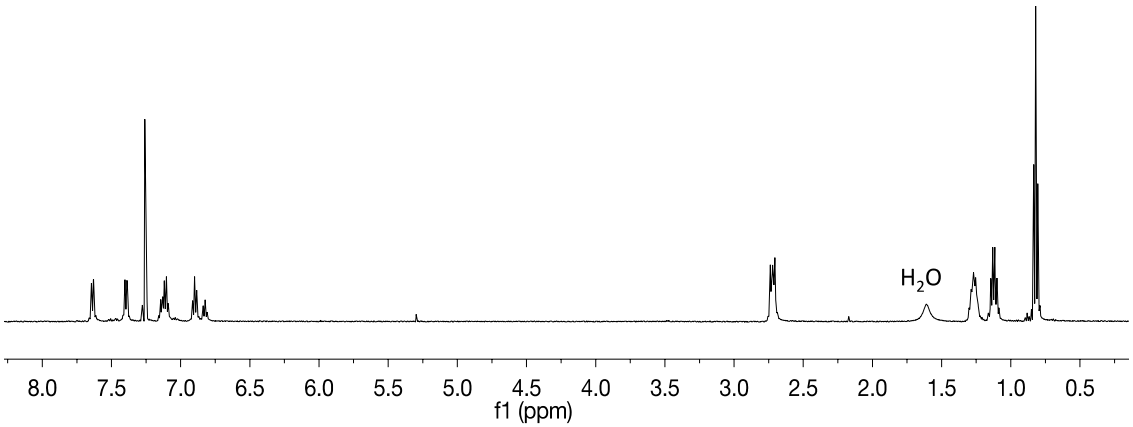

Figure 129. ^{1}H NMR spectra of **61** in $CDCl_3$.

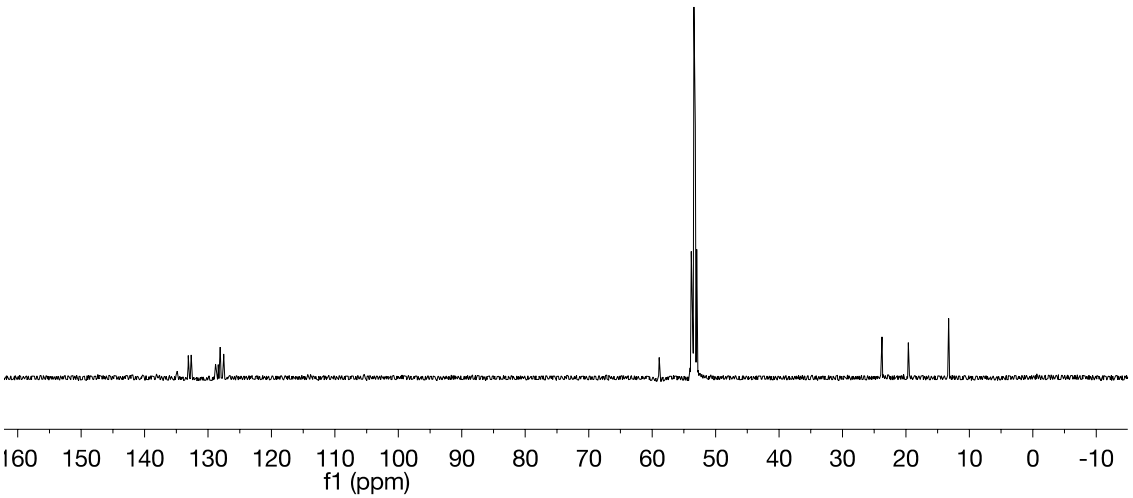

Figure 130. ^{13}C NMR spectra of **61** in $CDCl_3$.

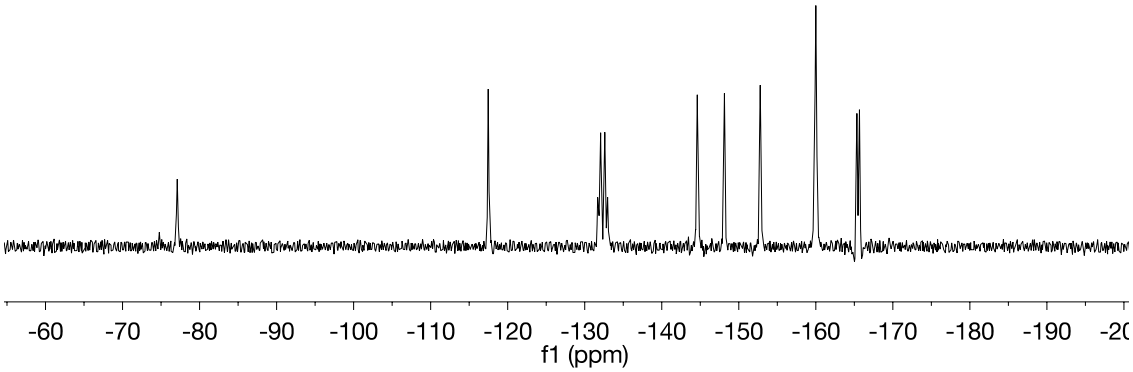

Figure 131. ^{19}F NMR spectra of **61** in $CDCl_3$.

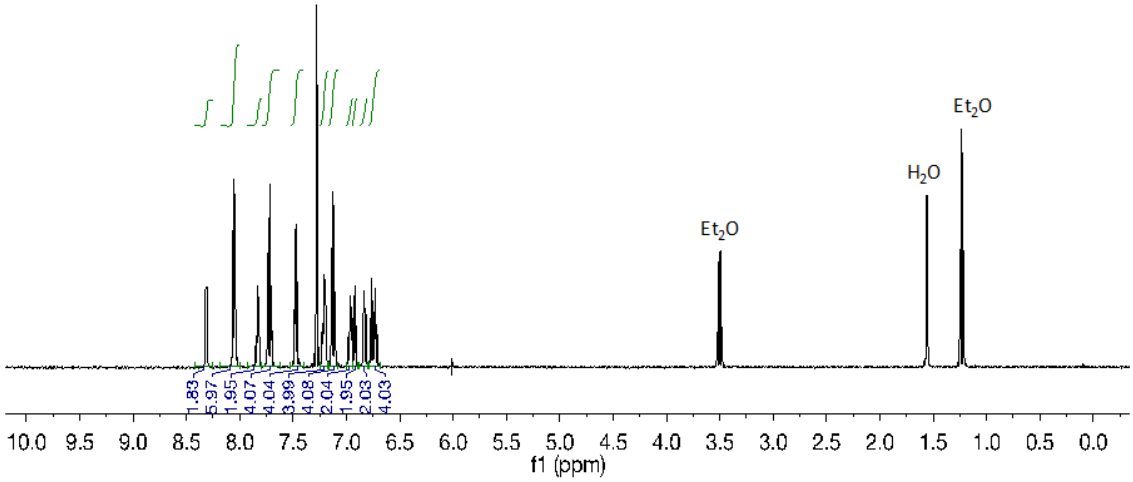

Figure 132. ^{1}H NMR spectra of **63** in $CDCl_3$.

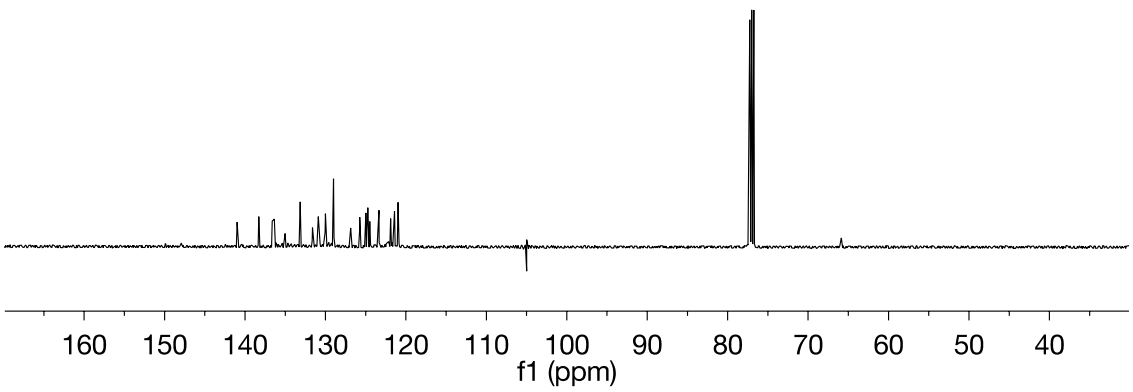

Figure 133. ^{13}C NMR spectra of **63** in $CDCl_3$.

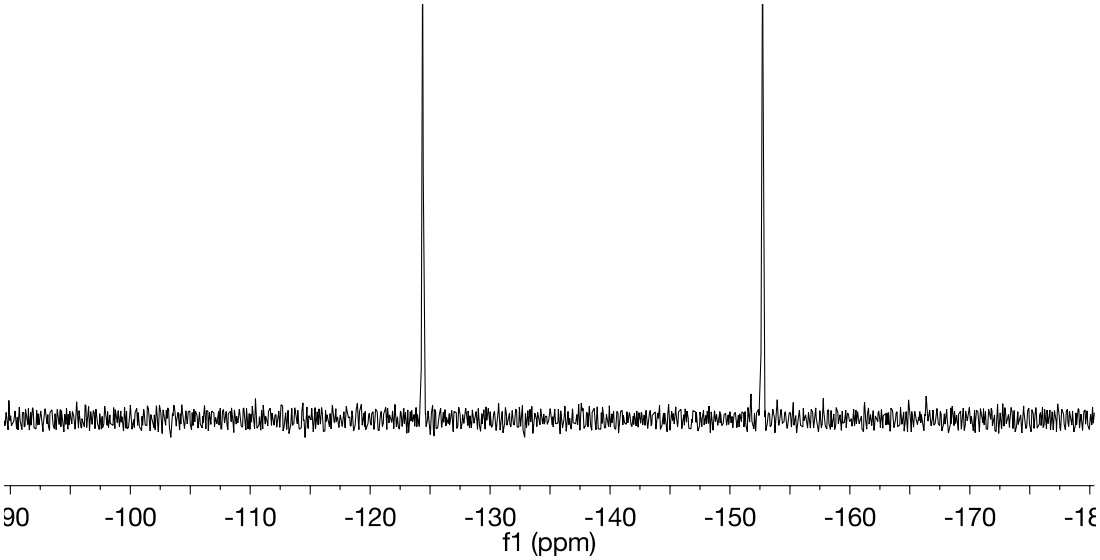

Figure 134. ^{19}F NMR spectra of **63** in $CDCl_3$.

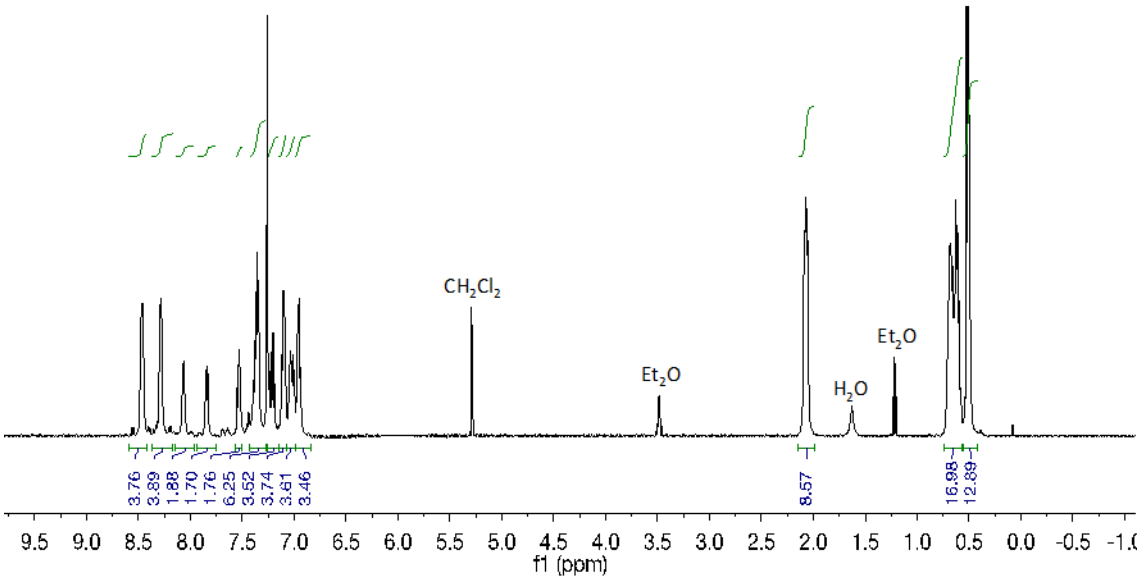

Figure 135. [1]H NMR spectra of TBA[**63**–F] in $CDCl_3$.

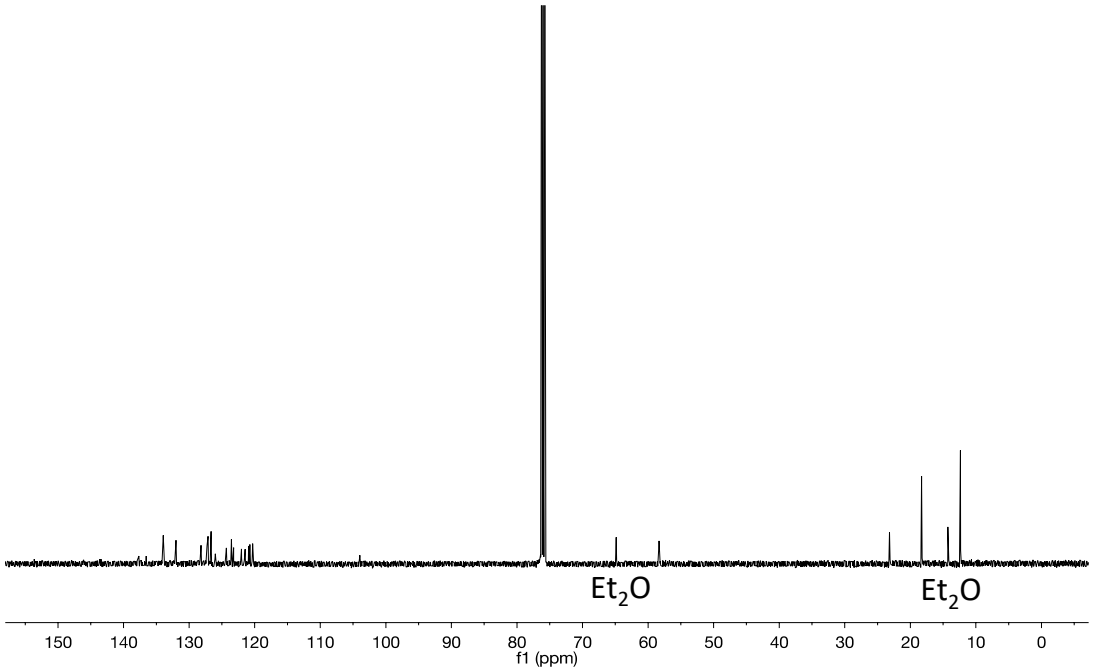

Figure 136. [13]C NMR spectra of TBA[**63**–F] in $CDCl_3$.

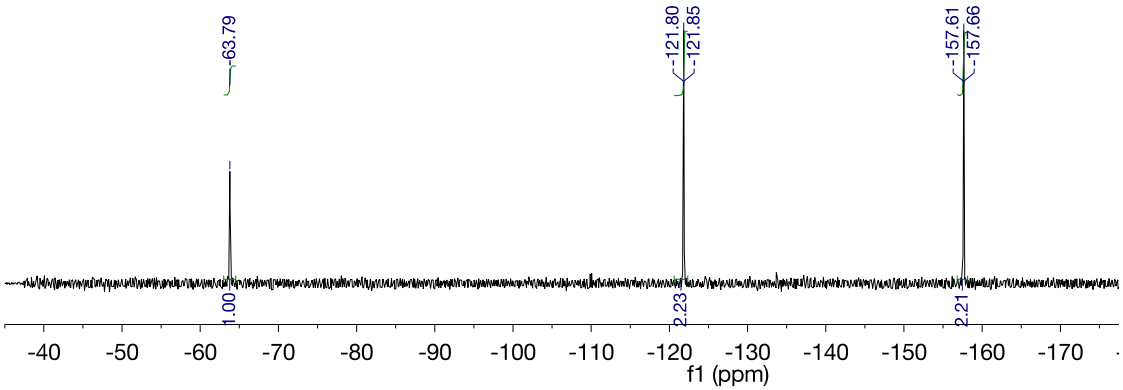

Figure 137. ^{19}F NMR spectra of TBA[**63**–F] in $CDCl_3$

CHAPTER VI

SUMMARY

In search of ligand platforms, which can be used to remotely control the catalytic activity of a transition metal, I have investigated the coordination non-innocence of amphiphilic L_2/Z-type ligands containing a trifluorostiborane unit or a (triflato)stiboranyl ligand as a Lewis acid. Complexes containing these ligands are derived from the known dichlorostiboranyl platinum complex ((*o*–$(Ph_2P)C_6H_4)_2SbCl_2$)PtCl (**43**). In Chapter II, I generated **44** (*o*–$(Ph_2P)C_6H_4)_2SbF_3$)Pt–NCMe) and **45** (*o*–$(Ph_2P)C_6H_4)_2SbF_3$)Pt–CNCy) with a view of testing halide abstraction reactions using $B(C_6F_5)_3$. These reactions afford the cationic complexes [*o*–$(Ph_2P)C_6H_4]_2SbF_2$]Pt–NCMe]$^+$ ([**46**]$^+$) and [*o*–$(Ph_2P)C_6H_4]_2SbF_2$]Pt–CNCy]$^+$ ([**47**]$^+$) which have been isolated as $[BF(C_6F_5)_3]^-$ salts. These complexes possess a highly Lewis acidic difluorostibonium moiety, which exerts an intense draw on the electron density of the platinum center. As a result, the latter becomes significantly more electrophilic. In the case of [**46**]$^+$, which contains a labile acetonitrile ligand, this increase electrophilicity translates into increased carbophilicity as reflected by the ability of this complex to promote enyne cyclization reactions. These results demonstrate that the coordination non-innocence of antimony Z-ligands can be used to adjust the catalytic activity of an adjoining metal center.

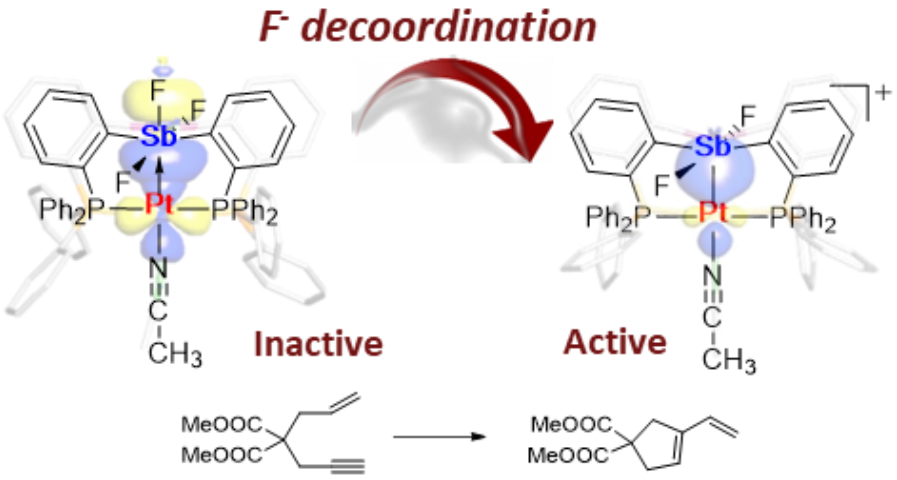

Figure 138. Modulating the σ-accepting properties of an antimony Z-type ligand via anion abstraction as presented in Chapter II.

In Chapter III, I have synthesized a platinum complex in which the metal is connected to a Lewis acidic bis(triflato)stiboranyl ligand. This complex, ((*o*–(Ph_2P)C_6H_4)$_2$$SbOTf_2$)PtCl (**50**), which was obtained by treatment of ((*o*–(Ph_2P)C_6H_4)$_2$$SbCl_2$)PtCl (**43**) with two equivalents of AgOTf, is surprisingly air stable. Yet, it promptly reacts with cyclohexylisocyanide to afford the dicationic chlorostibine complex [((*o*–(Ph_2P)C_6H_4)$_2$SbCl)PtCNCy]$^{2+}$ ([**51**]$^{2+}$) as a bis-triflate salt. Formation of [**51**]$^{2+}$ occurs through abstraction of the platinum-bound chloride ligand by the adjacent Lewis acidic antimony center. This halide migration reaction leads to activation of the platinum center. In turn, **50** behaves as a self-activating catalyst in reactions involving alkynes and readily mediate both enyne cyclisation and intramolecular hydroarylation reactions, at room temperature, without addition of a chloride abstracting reagent. These results demonstrate that the coordination non-innocence of antimony ligands can be exploited for the purpose of electrophilic catalysis.

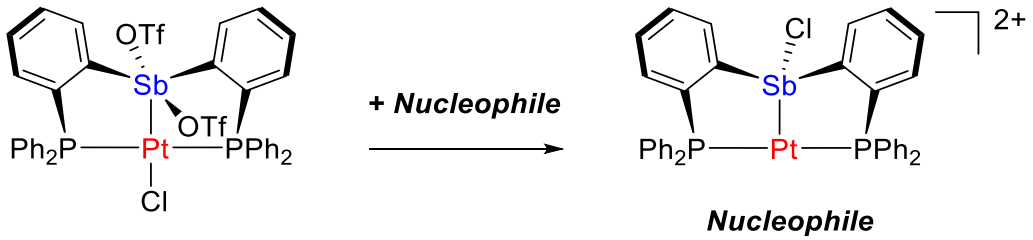

Figure 139. Idealized representation of the self-activating properties of the antimony bis(triflate) platinum complex investigated in Chapter III.

In Chapter IV, I synthesized two types of highly Lewis acidic antimony–platinum complexes, namely [(*o*–(Ph_2P)C_6H_4)$_2$Sb($OTf)_2$]Pt(OTf) (**53**) and (*o*–(^{i}Pr_2P)C_6H_4)$_2$Sb($OTf)_2$]Pt(OTf) (**54**) by treatment of [(*o*–(R_2P)C_6H_4)$_2$$SbCl_2$]PtCl (R = Ph or ^{i}Pr) with 3 equiv of AgOTf. The crystal structure of **54** confirmed that the chloride ligands have been fully substituted with more labile triflate ligands. Despite the structural and electronic similarities between **53** and **54**, only **52** is reactive in enyne cyclization reaction. Reactivity tests towards enyne cyclization reactions and hydroarylation reactions of pyrrole with acetylene and thiophene with ethyl propiolate showed that **53** has a higher reactivity than the previously reported self-activating catalyst [(*o*–(Ph_2P)C_6H_4)$_2$Sb($OTf)_2$]PtCl (**50**).

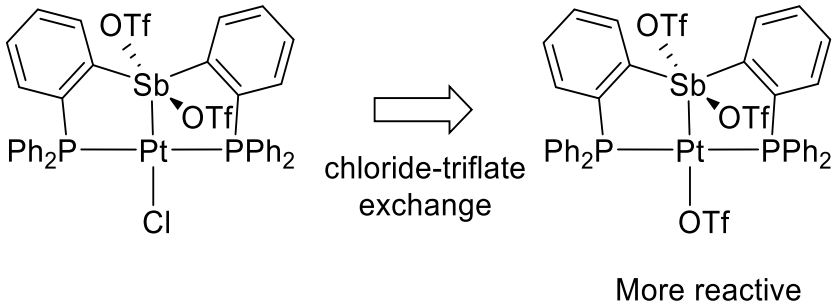

Figure 140. Illustration of the higher catalytic activity displayed by the tris(triflate) derivative described in Chapter IV.

In Chapter V, I inspected the strong Lewis acidity of antimony in the area of anion binding. Previous studies have shown that bifunctional Lewis acids form fluoride adducts stabilized by chelation effect. Based on this precedent, I developed a new bifunctional stibine(III) **59** featuring the fluorinated *ortho*–phenylene backbone. Oxidation of this complex with *o*–chloranil, octafluorophenthra–9,10–quinone and phenanthrenequinone generated stiborane(V) **60**, **61**, and **63**, respectively. The crystal structures of these compounds reveal that the two antimony centers are separated by 3.8176(8) Å in **60**, 3.5690(7)Å/3.5969(7)Å in **61**, and 3.507(5) Å in **63**. The small Sb–Sb separations in **61** and **63** are due to the strong Sb-O▪▪▪Sb interactions that bridge the two antimony atoms. The reaction of **60**, **61**, and **63** with fluoride ions resulted in the formation of the corresponding bridging fluoroantimonate complexes [**60**–F]$^-$, [**61**–F]$^-$, and [**63**–F]$^-$. Computational studies reveal that the fluoride ion affinities are 388.3 kJ mol^{-1} for **60**, and 396.3 kJ mol^{-1} for **61**. These values exceed that of the 9,9-dimethylxanthene-based distiborane **8** (FIA = 359.88 kJ mol^{-1}), thus indicating that **60** and **61** are more fluorophilic than **8**.

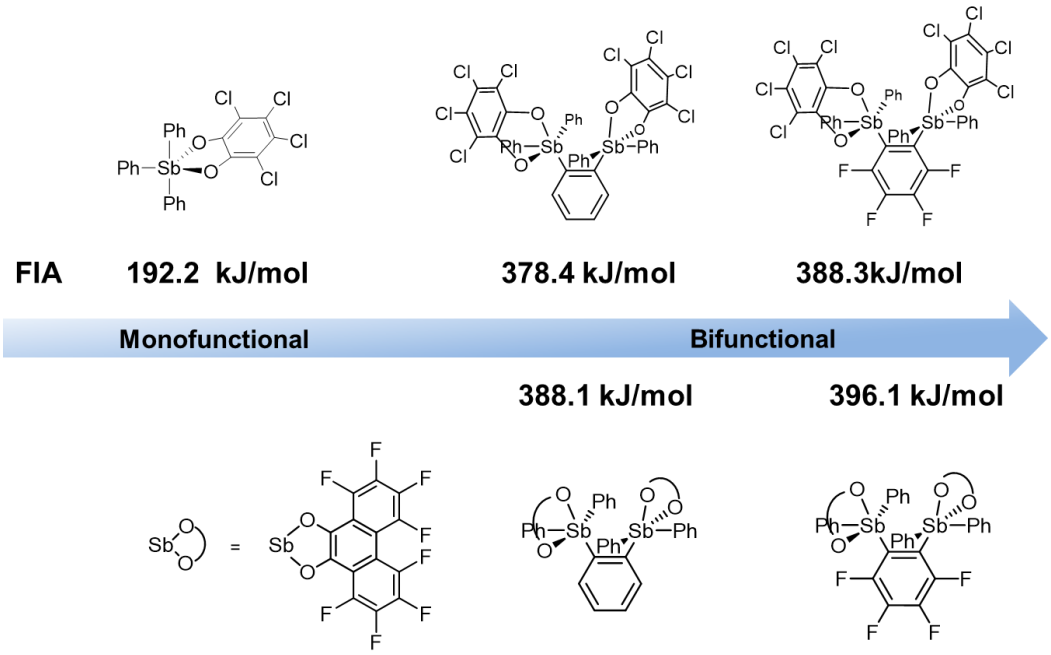

Figure 141. Increase in fluoride anion affinity resulting from the use of fluorinated substituents for the bifunctional antimony(V) Lewis acids described in Chapter V.

REFERENCES

(1) Price, C. C.; Ciskowski, J. M. *J. Am. Chem. Soc.* **1938**, *60*, 2499-2502.

(2) Harring, S. R.; Livinghouse, T. *J. Chem. Soc., Chem. Commun.* **1992**, 502-503.

(3) Hyatt, J. A.; Raynolds, P. W. *J. Org. Chem.* **1984**, *49*, 384-385.

(4) Tou, J. S.; Reusch, W. *J. Org. Chem.* **1980**, *45*, 5012-5014.

(5) Ruff, J. K. *Inorg. Chem.* **1964**, *3*, 1205-1206.

(6) Ishihara, K.; Yamamoto, H. **1999**, *1999*, 527-538.

(7) Ishihara, K.; Ohara, S.; Yamamoto, H. *J. Org. Chem.* **1996**, *61*, 4196-4197.

(8) Ishihara, K.; Kondo, S.; Yamamoto, H. *J. Org. Chem.* **2000**, *65*, 9125-9128.

(9) Schweighauser, L.; Wegner, H. A. *Chem. Eur. J.* **2016**, *22*, 14094-14103.

(10) Kessler, S. N.; Neuburger, M.; Wegner, H. A. *Eur. J. Org. Chem.* **2011**, *2011*, 3238-3245.

(11) Kessler, S. N.; Wegner, H. A. *Org. Lett.* **2010**, *12*, 4062-4065.

(12) Song, K. C.; Lee, K. M.; Kim, H.; Lee, Y. S.; Lee, M. H.; Do, Y. *J. Organomet. Chem.* **2012**, *713*, 89-95.

(13) Galbraith, E.; James, T. D. *Chemical Society Reviews* **2010**, *39*, 3831-3842.

(14) Prakash Reddy, V.; Sinn, E.; Hosmane, N. *J. Organomet. Chem.* **2015**, *798, Part 1*, 5-12.

(15) Chen, J.; Wenger, O. S. *Chem. Sci.* **2015**, *6*, 3582-3592.

(16) Zhao, H.; Leamer, L. A.; Gabbaï, F. P. *Dalton Trans.* **2013**, *42*, 8164-8178.

(17) Yamaguchi, S.; Akiyama, S.; Tamao, K. *J. Am. Chem. Soc.* **2001**, *123*, 11372-11375.

(18) Jia, L.; Yang, X.; Ishihara, A.; Marks, T. J. *Organometallics* **1995**, *14*, 3135-3137.

(19) Yang, X.; Stern, C. L.; Marks, T. J. *J. Am. Chem. Soc.* **1991**, *113*, 3623-3625.

(20) Yang, X.; Stern, C. L.; Marks, T. J. *J. Am. Chem. Soc.* **1994**, *116*, 10015-10031.

(21) Grassi, A.; Pellecchia, C.; Oliva, L.; Laschi, F. *Macromol. Chem. Phys.* **1995**, *196*, 1093-1100.

(22) Stephan, D. W.; Erker, G. *Angew. Chem. Int. Ed.* **2015**, *54*, 6400-6441.

(23) Stephan, D. W. *Acc. Chem. Res.* **2015**, *48*, 306-316.

(24) Courtemanche, M.-A.; Légaré, M.-A.; Maron, L.; Fontaine, F.-G. *J. Am. Chem. Soc.* **2014**, *136*, 10708-10717.

(25) Courtemanche, M.-A.; Légaré, M.-A.; Maron, L.; Fontaine, F.-G. *J. Am. Chem. Soc.* **2013**, *135*, 9326-9329.

(26) Stephan, D. W.; Erker, G. *Angew. Chem. Int. Ed.* **2010**, *49*, 46-76.

(27) Ménard, G.; Stephan, D. W. *Angew. Chem. Int. Ed.* **2012**, *124*, 4485-4488.

(28) Erős, G.; Mehdi, H.; Pápai, I.; Rokob, T. A.; Király, P.; Tárkányi, G.; Soós, T. *Angew. Chem. Int. Ed.* **2010**, *122*, 6709-6713.

(29) Eisenberger, P.; Bailey, A. M.; Crudden, C. M. *J. Am. Chem. Soc.* **2012**, *134*, 17384-17387.

(30) Babbini, D. C.; Mulligan, F. L.; Schulhauser, H. R.; Sweigart, T. C.; Nichol, G. S.; Hurst, S. K. *Inorg. Chem.* **2010**, *49*, 4307-4312.

(31) Copolovici, D.; Isaia, F.; Breunig, H. J.; Raţ, C. I.; Silvestru, C. *RSC Adv.* **2014**, *4*, 26569-26576.

(32) Ohkata, K.; Takemoto, S.; Ohnishi, M.; Akiba, K.-Y. *Tetrahedron Lett.* **1989**, *30*, 4841-4844.

(33) Benjamin, S. L.; Levason, W.; Reid, G.; Warr, R. P. *Organometallics* **2012**, *31*, 1025-1034.

(34) Qiu, J.; Song, B.; Li, X.; Cozzolino, A. F. *Phys. Chem. Chem. Phys.* **2018**, *20*, 46-50.

(35) Christianson, A. M.; Gabbaï, F. P. *Inorg. Chem.* **2016**, *55*, 5828-5835.

(36) Böhrer, H.; Trapp, N.; Himmel, D.; Schleep, M.; Krossing, I. *Dalton Trans.* **2015**, *44*, 7489-7499.

(37) Olah, G. A.; Tolgyesi, W. S.; Kuhn, S. J.; Moffatt, M. E.; Bastien, I. J.; Baker, E. B. *J. Am. Chem. Soc.* **1963**, *85*, 1328-1334.

(38) Olah, G. A.; Lukas, J. *J. Am. Chem. Soc.* **1967**, *89*, 2227-2228.

(39) Commeyras, A.; Olah, G. A. *J. Am. Chem. Soc.* **1969**, *91*, 2929-2942.

(40) Olah, G. A.; Schlosberg, R. H. *J. Am. Chem. Soc.* **1968**, *90*, 2726-2727.

(41) Krossing, I.; Raabe, I. *Angew. Chem. Int. Ed.* **2004**, *43*, 2066-2090.

(42) Gutmann, V.; H., T. *Monatsh. Chem.* **1957**, *88*, 216-227.

(43) Gutmann, V.; Hubacek, H.; Steininger, A. *Monatsh. Chem.* **1964**, *95*, 678-686.

(44) Gutmann, V. *Dalton Trans* **1976**, *18*, 225-255.

(45) Pan, B.; Gabbaï, F. P. *J. Am. Chem. Soc.* **2014**, *136*, 9564-9567.

(46) Bowen, L. H.; Rood, R. T. *J. Inorg. Nucl. Chem.* **1966**, *28*, 1985-1990.

(47) Jean, M. *Anal. Chim. Acta.* **1971**, *57*, 438-439.

(48) Holmes, R. R.; Day, R. O.; Chandrasekhar, V.; Holmes, J. M. *Inorg. Chem.* **1987**, *26*, 157-163.

(49) Cherkasov, V. K.; Abakumov, G. A.; Grunova, E. V.; Poddel'sky, A. I.; Fukin, G. K.; Baranov, E. V.; Kurskii, Y. V.; Abakumova, L. G. *Chem.--Eur. J.* **2006**, *12*, 3916-3927.

(50) Arsenyev, M. V.; Shurygina, M. P.; Poddel'sky, A. I.; Druzhkov, N. O.; Chesnokov, S. A.; Fukin, G. K.; Cherkasov, V. K.; Abakumov, G. A. *J. Polym. Res.* **2013**, *20*, 1-9.

(51) Abakumov, G. A.; Poddel'sky, A. I.; Grunova, E. V.; Cherkasov, V. K.; Fukin, G. K.; Kurskii, Y. A.; Abakumova, L. G. *Angew. Chem. Int. Ed.* **2005**, *44*, 2767-2771.

(52) Abakumov, G. A.; Vavilina, N. N.; Kurskii, Y. A.; Abakumova, L. G.; Fukin, G. K.; Cherkasov, V. K.; Shavyrin, A. S.; Baranov, E. V. J. R. C. B. *Russ. Chem. Bull.* **2007**, *56*, 1813-1820.

(53) Breunig, H. J.; Koehne, T.; Moldovan, O.; Preda, A. M.; Silvestru, A.; Silvestru, C.; Varga, R. A.; Piedra-Garza, L. F.; Kortz, U. *J. Organomet. Chem.* **2010**, *695*, 1307-1313.

(54) Lim, Y. Y.; Drago, R. S. *Inorg. Chem.* **1972**, *11*, 202-204.

(55) Nishii, N.; Matsumura, Y.; Okawara, R. *J. Organomet. Chem.* **1971**, *30*, 59-65.

(56) Nishii, N.; Hashimoto, K.; Okawara, R. *J. Organomet. Chem.* **1973**, *55*, 133-137.

(57) Bordner, J.; Doak, G. O.; Peters, J. R. *J. Am. Chem. Soc.* **1974**, *96*, 6763-6765.

(58) Hall, M.; Sowerby, D. B. *J. Am. Chem. Soc.* **1980**, *102*, 628-632.

(59) Tunde Bamgboye, T.; Begley, M. J.; Bryan Sowerby, D. *J. Organomet. Chem.* **1989**, *362*, 77-85.

(60) Dodonov, V. A.; Fedorov, A. Y.; Fukin, G. K.; Zaburdyaeva, S. N.; Zakharov, L. N.; Ígnatenko, A. V. *Main Group Chemistry* **1999**, *3*, 15-22.

(61) Robertson, A. P. M.; Burford, N.; McDonald, R.; Ferguson, M. J. *Angew. Chem. Int. Ed.* **2014**, *53*, 3480-3483.

(62) Chitnis, S. S.; Robertson, A. P. M.; Burford, N.; Patrick, B. O.; McDonald, R.; Ferguson, M. J. *Chem. Sci.* **2015**, *6*, 6545-6555.

(63) Robertson, A. P. M.; Chitnis, S. S.; Jenkins, H. A.; McDonald, R.; Ferguson, M. J.; Burford, N. *Chem. Eur. J.* **2015**, *21*, 7902-7913.

(64) Tofan, D.; Gabbaï, F. P. *Chem. Sci.* **2016**, *7*, 6768-6778.

(65) Hirai, M.; Gabbaï, F. P. *Angew. Chem. Int. Ed.* **2015**, *54*, 1205-1209.

(66) Hirai, M.; Gabbaï, F. P. *Chem. Sci.* **2014**, *5*, 1886-1893.

(67) Hirai, M.; Myahkostupov, M.; Castellano, F. N.; Gabbaï, F. P. *Organometallics* **2016**, *35*, 1854-1860.

(68) Wade, C. R.; Gabbaï, F. P. *Organometallics* **2011**, *30*, 4479-4481.

(69) Hirai, M.; Cho, J.; Gabbaï, F. P. *Chem. Eur. J.* **2016**, *22*, 6537-6541.

(70) Yang, M.; Pati, N.; Belanger-Chabot, G.; Hirai, M.; Gabbaï, F. P. *Dalton Trans.* **2018**, *47*, 11843-11850.

(71) Yang, M.; Tofan, D.; Chen, C.-H.; Jack, K. M.; Gabbaï, F. P. *Angew. Chem. Int. Ed.* **2018**, *57*, 13868-13872.

(72) Yang, M.; Gabbaï, F. P. *Inorg. Chem.* **2017**, *56*, 8644-8650.

(73) Ke, I.-S.; Myahkostupov, M.; Castellano, F. N.; Gabbaï, F. P. *J. Am. Chem. Soc.* **2012**, *134*, 15309-15311.

(74) Chen, C.-H.; Gabbaï, F. P. *Angew. Chem. Int. Ed.* **2017**, *56*, 1799-1804.

(75) Hall, M.; Sowerby, D. B. *Journal of the Chemical Society, Dalton Transactions* **1983**, 1095-1099.

(76) Holthausen, M. H.; Mehta, M.; Stephan, D. W. *Angew. Chem. Int. Ed.* **2014**, *53*, 6538-6541.

(77) Tsao, F. A.; Waked, A. E.; Cao, L.; Hofmann, J.; Liu, L.; Grimme, S.; Stephan, D. W. *Chem. Commun.* **2016**, *52*, 12418-12421.

(78) Maity, A.; Teets, T. S. *Chem. Rev.* **2016**, *116*, 8873-8911.

(79) Shook, R. L.; Borovik, A. S. *Inorg. Chem.* **2010**, *49*, 3646-3660.

(80) Lewis, J. C. *ACS Catal.* **2013**, *3*, 2954-2975.

(81) Dogutan, D. K.; Bediako, D. K.; Graham, D. J.; Lemon, C. M.; Nocera, D. G. *J. Porphyr. Phthalocyanines* **2015**, *19*, 1-8.

(82) Cook, S. A.; Borovik, A. S. *Acc. Chem. Res.* **2015**, *48*, 2407-2414.

(83) Hale, L. V. A.; Szymczak, N. K. *ACS Catal.* **2018**, *8*, 6446-6461.

(84) Creutz, S. E.; Peters, J. C. *Chem. Sci.* **2017**, *8*, 2321-2328.

(85) Bullock, R. M.; Helm, M. L. *Acc. Chem. Res.* **2015**, *48*, 2017-2026.

(86) Dahl, E. W.; Dong, H. T.; Szymczak, N. K. *Chem. Commun.* **2018**, *54*, 892-895.

(87) Azcarate, I.; Costentin, C.; Robert, M.; Savéant, J.-M. *J. Am. Chem. Soc.* **2016**, *138*, 16639-16644.

(88) Sung, S.; Kumar, D.; Gil-Sepulcre, M.; Nippe, M. *J. Am. Chem. Soc.* **2017**, *139*, 13993-13996.

(89) Schmeier, T. J.; Dobereiner, G. E.; Crabtree, R. H.; Hazari, N. *J. Am. Chem. Soc.* **2011**, *133*, 9274-9277.

(90) Kiernicki, J. J.; Zeller, M.; Szymczak, N. K. *J. Am. Chem. Soc.* **2017**, *139*, 18194-18197.

(91) Tseng, K.-N. T.; Kampf, J. W.; Szymczak, N. K. *J. Am. Chem. Soc.* **2016**, *138*, 10378-10381.

(92) Miller, A. J. M.; Labinger, J. A.; Bercaw, J. E. *J. Am. Chem. Soc.* **2008**, *130*, 11874-11875.

(93) Shriver, D. F. *Acc. Chem. Res.* **1970**, *3*, 231-238.

(94) Parkin, G. *Organometallics* **2006**, *25*, 4744-4747.

(95) Hill, A. F. *Organometallics* **2006**, *25*, 4741-4743.

(96) Bouhadir, G.; Amgoune, A.; Bourissou, D. *Adv. Organomet. Chem.* **2010**, *58*, 1-107.

(97) Amgoune, A.; Bourissou, D. *Chem. Commun.* **2011**, *47*, 859-871.

(98) Braunschweig, H.; Dewhurst, R. D. *Dalton Trans.* **2011**, *40*, 549-558.

(99) Kameo, H.; Nakazawa, H. *Chem. Asian J.* **2013**, *8*, 1720-1734.

(100) Jones, J. S.; Gabbaï, F. P. *Acc. Chem. Res.* **2016**, *49*, 857-867.

(101) Jones, J. S.; Gabbaï, F. P. *Chem. Lett.* **2016**, *45*, 376-384.

(102) Bouhadir, G.; Bourissou, D. *Chem. Soc. Rev.* **2016**, *45*, 1065-1079.

(103) Anderson, J. S.; Rittle, J.; Peters, J. C. *Nature* **2013**, *501*, 84-87.

(104) Cammarota, R. C.; Lu, C. C. *J. Am. Chem. Soc.* **2015**, *137*, 12486-12489.

(105) Vollmer, M. V.; Xie, J.; Lu, C. C. *J. Am. Chem. Soc.* **2017**, *139*, 6570-6573.

(106) Kameo, H.; Ikeda, K.; Bourissou, D.; Sakaki, S.; Takemoto, S.; Nakazawa, H.; Matsuzaka, H. *Organometallics* **2016**, *35*, 713-719.

(107) Kameo, H.; Kawamoto, T.; Sakaki, S.; Bourissou, D.; Nakazawa, H. *Chem. Eur. J.* **2016**, *22*, 2370-2375.

(108) Schindler, T.; Lux, M.; Peters, M.; Scharf, L. T.; Osseili, H.; Maron, L.; Tauchert, M. E. *Organometallics* **2015**, *34*, 1978-1984.

(109) Fong, H.; Moret, M.-E.; Lee, Y.; Peters, J. C. *Organometallics* **2013**, *32*, 3053-3062.

(110) Shih, W.-C.; Gu, W.; MacInnis, M. C.; Timpa, S. D.; Bhuvanesh, N.; Zhou, J.; Ozerov, O. V. *J. Am. Chem. Soc.* **2016**, *138*, 2086-2089.

(111) Barnett, B. R.; Moore, C. E.; Chandrasekaran, P.; Sproules, S.; Rheingold, A. L.; DeBeer, S.; Figueroa, J. S. *Chem. Sci.* **2015**, *6*, 7169-7178.

(112) Lin, T.-P.; Nelson, R. C.; Wu, T.; Miller, J. T.; Gabbaï, F. P. *Chem. Sci.* **2012**, *3*, 1128-1136.

(113) Frenking, G.; Fau, S.; Marchand, C. M.; Grützmacher, H. *J. Am. Chem. Soc.* **1997**, *119*, 6648-6655.

(114) Huggett, P. G.; Manning, K.; Wade, K. *J. Inorg. Nucl. Chem.* **1980**, *42*, 665-673.

(115) Bontemps, S.; Bouhadir, G.; Gu, W.; Mercy, M.; Chen, C.-H.; Foxman, B. M.; Maron, L.; Ozerov, O. V.; Bourissou, D. *Angew. Chem. Int. Ed.* **2008**, *47*, 1481-1484.

(116) Sircoglou, M.; Mercy, M.; Saffon, N.; Coppel, Y.; Bouhadir, G.; Maron, L.; Bourissou, D. *Angew. Chem. Int. Ed.* **2009**, *48*, 3454-3457.

(117) Sircoglou, M.; Saffon, N.; Miqueu, K.; Bouhadir, G.; Bourissou, D. *Organometallics* **2013**, *32*, 6780-6784.

(118) Derrah, E. J.; Sircoglou, M.; Mercy, M.; Ladeira, S.; Bouhadir, G.; Miqueu, K.; Maron, L.; Bourissou, D. *Organometallics* **2011**, *30*, 657-660.

(119) Gualco, P.; Lin, T.-P.; Sircoglou, M.; Mercy, M.; Ladeira, S.; Bouhadir, G.; Pérez, L. M.; Amgoune, A.; Maron, L.; Gabbaï, F. P.; Bourissou, D. *Angew. Chem. Int. Ed.* **2009**, *48*, 9892-9895.

(120) Cotton, F. A.; Murillo, C. A.; Walton, R. A.: *Multiple Bonds Between Metal Atoms*; Springer Science: New York, 2005.

(121) Cordero, B.; Gomez, V.; Platero-Prats, A. E.; Reves, M.; Echeverria, J.; Cremades, E.; Barragan, F.; Alvarez, S. *Dalton Trans.* **2008**, 2832-2838.

(122) Takaya, J.; Iwasawa, N. *J. Am. Chem. Soc.* **2017**, *139*, 6074-6077.

(123) Timoshkin, A. Y.; Suvorov, A. V.; Bettinger, H. F.; Schaefer, H. F. *J. Am. Chem. Soc.* **1999**, *121*, 5687-5699.

(124) Gualco, P.; Mercy, M.; Ladeira, S.; Coppel, Y.; Maron, L.; Amgoune, A.; Bourissou, D. *Chem. Eur. J.* **2010**, *16*, 10808-10817.

(125) Yang, H.; Gabbaï, F. P. *J. Am. Chem. Soc.* **2015**, *137*, 13425-13432.

(126) Alcarazo, M. *Acc. Chem. Res.* **2016**, *49*, 1797-1805.

(127) Ke, I.-S.; Gabbaï, F. P. *Inorg. Chem.* **2013**, *52*, 7145-7151.

(128) Tschersich, C.; Limberg, C.; Roggan, S.; Herwig, C.; Ernsting, N.; Kovalenko, S.; Mebs, S. *Angew. Chem. Int. Ed.* **2012**, *51*, 4989-4992.

(129) Lin, T.-P.; Ke, I.-S.; Gabbaï, F. P. *Angew. Chem. Int. Ed.* **2012**, *51*, 4985–4988.

(130) Tschersich, C.; Hoof, S.; Frank, N.; Herwig, C.; Limberg, C. *Inorg. Chem.* **2016**, *55*, 1837-1842.

(131) Benz, S.; Poblador-Bahamonde, A. I.; Low-Ders, N.; Matile, S. *Angew. Chem. Int. Ed.* **2018**, *57*, 5408-5412.

(132) Bontemps, S.; Bouhadir, G.; Miqueu, K.; Bourissou, D. *J. Am. Chem. Soc.* **2006**, *128*, 12056-12057.

(133) Chase, P. A.; Piers, W. E.; Patrick, B. O. *J. Am. Chem. Soc.* **2000**, *122*, 12911-12912.

(134) Wade, C. R.; Gabbaï, F. P. *Angew. Chem. Int. Ed.* **2011**, *50*, 7369-7372.

(135) Taylor, J. W.; McSkimming, A.; Moret, M.-E.; Harman, W. H. *Inorg. Chem.* **2018**, *57*, 15406-15413.

(136) Moret, M.-E.; Zhang, L.; Peters, J. C. *J. Am. Chem. Soc.* **2013**, *135*, 3792-3795.

(137) Vollmer, M. V.; Xie, J.; Cammarota, R. C.; Young Jr., V. G.; Bill, E.; Gagliardi, L.; Lu, C. C. *Angew. Chem. Int. Ed.* **2018**, *57*, 7815-7819.

(138) Wade, C. R.; Ke, I.-S.; Gabbaï, F. P. *Angew. Chem. Int. Ed.* **2012**, *51*, 478-481.

(139) Ke, I.-S.; Jones, J. S.; Gabbaï, F. P. *Angew. Chem. Int. Ed.* **2014**, *53*, 2633-2637.

(140) Jones, J. S.; Wade, C. R.; Gabbaï, F. P. *Angew. Chem. Int. Ed.* **2014**, *53*, 8876-8879.

(141) Jones, J. S.; Wade, C. R.; Yang, M.; Gabbaï, F. P. *Dalton Trans.* **2017**, *46*, 5598-5604.

(142) Jones, J. S.; Gabbaï, F. P. *Chem. Eur. J.* **2017**, *23*, 1136-1144.

(143) Benjamin, S. L.; Levason, W.; Light, M. E.; Reid, G.; Rogers, S. M. *Organometallics* **2014**, *33*, 2693-2695.

(144) Jones, J. S.; Wade, C. R.; Gabbaï, F. P. *Organometallics* **2015**, *34*, 2647-2654.

(145) Jolleys, A.; Lake, B. R. M.; Krämer, T.; Benjamin, S. L. *Organometallics* **2018**, *37*, 3854-3862.

(146) Plajer, A. J.; Colebatch, A. L.; Rizzuto, F. J.; Pröhm, P.; Bond, A. D.; García-Rodríguez, R.; Wright, D. S. *Angew. Chem. Int. Ed.* **2018**, *57*, 6648-6652.

(147) Matson, B. D.; Peters, J. C. *ACS Catal.* **2018**, *8*, 1448-1455.

(148) Harman, W. H.; Peters, J. C. *J. Am. Chem. Soc.* **2012**, *134*, 5080-5082.

(149) Cammarota, R. C.; Clouston, L. J.; Lu, C. C. *Dalton Trans* **2017**, *334*, 100-111.

(150) Steinhoff, P.; Paul, M.; Schroers, J. P.; Tauchert, M. E. *Dalton Trans.* **2019**, *48*, 1017-1022.

(151) Steinhoff, P.; Steinbock, R.; Friedrich, A.; Schieweck, B. G.; Cremer, C.; Truong, K.-N.; Tauchert, M. E. *Dalton Trans.* **2018**, *47*, 10439-10442.

(152) Inagaki, F.; Matsumoto, C.; Okada, Y.; Maruyama, N.; Mukai, C. *Angew. Chem. Int. Ed.* **2015**, *54*, 818-822.

(153) Inagaki, F.; Nakazawa, K.; Maeda, K.; Koseki, T.; Mukai, C. *Organometallics* **2017**, *36*, 3005-3008.

(154) Matsumoto, C.; Yamada, M.; Dong, X.; Mukai, C.; Inagaki, F. *Chem. Lett.* **2018**, *47*, 1321-1323.

(155) Aullón, G.; Alvarez, S. *Inorg. Chem.* **1996**, *35*, 3137-3144.

(156) Lin, T.-P.; Wade, C. R.; Pérez, L. M.; Gabbaï, F. P. *Angew. Chem. Int. Ed.* **2010**, *49*, 6357-6360.

(157) Sen, S.; Ke, I.-S.; Gabbaï, F. P. *Organometallics* **2017**, *36*, 4224-4230.

(158) Benjamin, S. L.; Reid, G. *Dalton Trans* **2015**, *297*, 168-180.

(159) Yang, H.; Gabbaï, F. P. *J. Am. Chem. Soc.* **2014**, *136*, 10866–10869.

(160) Braunschweig, H.; Gruss, K.; Radacki, K. *Angew. Chem. Int. Ed.* **2007**, *46*, 7782-7784.

(161) Braunschweig, H.; Gruss, K.; Radacki, K. *Inorg. Chem.* **2008**, *47*, 8595-8597.

(162) Braunschweig, H.; Gruss, K.; Radacki, K. *Angew. Chem. Int. Ed.* **2009**, *48*, 4239-4241.

(163) Braunschweig, H.; Radacki, K.; Schwab, K. *Chem. Commun.* **2010**, *46*, 913-915.

(164) Ma, M.; Sidiropoulos, A.; Ralte, L.; Stasch, A.; Jones, C. *Chem. Commun.* **2013**, *49*, 48-50.

(165) You, D.; Gabbaï, F. P. *J. Am. Chem. Soc.* **2017**, *139*, 6843-6846.

(166) Chatani, N.; Furukawa, N.; Sakurai, H.; Murai, S. *Organometallics* **1996**, *15*, 901-903.

(167) Fürstner, A.; Stelzer, F.; Szillat, H. *J. Am. Chem. Soc.* **2001**, *123*, 11863-11869.

(168) He, F.; Danopoulos, A. A.; Braunstein, P. *Organometallics* **2016**, *35*, 198-206.

(169) De Crisci, A. G.; Lough, A. J.; Multani, K.; Fekl, U. *Organometallics* **2008**, *27*, 1765-1779.

(170) Manson, J.; Webster, C. E.; Pérez, L. M.; Hall, M. B., http://www.chem.tamu.edu/jimp2/index.html.

(171) Yang, H. (**2016**) Antimony and Tellurium Non-Innocent Z-Ligands for Transition Metals and Their Application in Photoredox Chemistry and Electrophilic Catalysis (Doctoral dissertation). Retrieved from https://oaktrust.library.tamu.edu/

(172) Chen, E. Y.-X.; Marks, T. J. *Chem. Rev.* **2000**, *100*, 1391-1434.

(173) Piers, W. E. *Adv. Organomet. Chem.* **2004**, *52*, 1-76.

(174) Figueroa, J. S.; Melnick, J. G.; Parkin, G. *Inorg. Chem.* **2006**, *45*, 7056-7058.

(175) Masuda, Y.; Hasegawa, M.; Yamashita, M.; Nozaki, K.; Ishida, N.; Murakami, M. *J. Am. Chem. Soc.* **2013**, *135*, 7142-7145.

(176) Barnett, B. R.; Moore, C. E.; Rheingold, A. L.; Figueroa, J. S. *J. Am. Chem. Soc.* **2014**, *136*, 10262-10265.

(177) Cowie, B. E.; Emslie, D. J. H. *Chem. Eur. J.* **2014**, *20*, 16899-16912.

(178) Shih, W.-C.; Ozerov, O. V. *Organometallics* **2017**, *36*, 228-233.

(179) Devillard, M.; Nicolas, E.; Appelt, C.; Backs, J.; Mallet-Ladeira, S.; Bouhadir, G.; Slootweg, J. C.; Uhl, W.; Bourissou, D. *Chem. Commun.* **2014**, *50*, 14805-14808.

(180) Levason, W.; Reid, G. *Dalton Trans* **2006**, *250*, 2565-2594.

(181) Malisch, W.; Panster, P. *Angew. Chem. Int. Ed.* **1974**, *13*, 670-672.

(182) Bauer, J.; Braunschweig, H.; Dewhurst, R. D. *Chem. Rev.* **2012**, *112*, 4329-4346.

(183) MacInnis, M. C.; DeMott, J. C.; Zolnhofer, E. M.; Zhou, J.; Meyer, K.; Hughes, R. P.; Ozerov, O. V. *Chem* **2016**, *1*, 902-920.

(184) Campos, J. *J. Am. Chem. Soc.* **2017**, *139*, 2944-2947.

(185) Niyogi, D. G.; Singh, S.; Verma, R. D. *J. Fluor. Chem.* **1995**, *70*, 237-240.

(186) Tinnermann, H.; Wille, C.; Alcarazo, M. *Angew. Chem. Int. Ed.* **2014**, *53*, 8732-8736.

(187) Dube, J. W.; Zheng, Y.; Thiel, W.; Alcarazo, M. *J. Am. Chem. Soc.* **2016**, *138*, 6869-6877.

(188) Aseman, M. D.; Roselli, C. A.; Gagné, M. R. *Organometallics* **2015**, *34*, 2707-2709.

(189) Allegretti, P. A.; Ferreira, E. M. *J. Am. Chem. Soc.* **2013**, *135*, 17266-17269.

(190) Pastine, S. J.; Youn, S. W.; Sames, D. *Org. Lett.* **2003**, *5*, 1055-1058.

(191) Olah, G. A.; Klopman, G.; Schlosberg, R. H. *J. Am. Chem. Soc* **1969**, *91*, 3261-3268.

(192) Ishihara, K. In *Tilte*2000; Wiley-VCH Verlag GmbH.

(193) Koppaka, A.; Park, S. H.; Hashiguchi, B. G.; Gunsalus, N. J.; King, C. R.; Konnick, M. M.; Ess, D. H.; Periana, R. A. *Angew. Chem. 2008, 120, 4122-4126;* **2019**, *58*, 2241-2245.

(194) Chitnis, S. S.; Sparkes, H. A.; Annibale, V. T.; Pridmore, N. E.; Oliver, A. M.; Manners, I. *Angew. Chem. 2008, 120, 4122-4126;* **2017**, *56*, 9536-9540.

(195) Qiu, R.; Chen, Y.; Yin, S.-F.; Xu, X.; Au, C.-T. *RSC Advances* **2012**, *2*, 10774-10793.

(196) Chitnis, S. S.; Burford, N.; McDonald, R.; Ferguson, M. J. *Inorganic Chemistry* **2014**, *53*, 5359-5372.

(197) Singhal, K.; Yadav, R. N. P.; Raj, P.; Agarwal, A. K. *Journal of Fluorine Chemistry* **2003**, *121*, 131-134.

(198) Greb, L. *Chemistry - A European Journal* **2018**, *24*, 17881-17896.

(199) Yang, M.; Tofan, D.; Chen, C.-H.; Jack, K. M.; Gabbaï, F. P. **2018**, *57*, 13868-13872.

(200) Tofan, D.; Gabbaï, F. P. *Chemical Science* **2016**, *7*, 6768-6778.

(201) Park, G.; Brock, D. J.; Pellois, J.-P.; Gabbaï, F. P. *Chem* **2019**, *5*, 2215-2227.

(202) Lo, Y. H.; Gabbai, F. P. *Angewandte Chemie, International Edition* **2019**, *58*, 10194-10197.

(203) You, D.; Gabbaï, F. P. *Trends in Chemistry* **2019**, *1*, 485-496.

(204) Annibale, G.; Bergamini, P.; Bertolasi, V.; Cattabriga, M.; Ferretti, V. *Inorg. Chem. Commun.* **2000**, *3*, 303-306.

(205) Harkins, S. B.; Peters, J. C. *Organometallics* **2002**, *21*, 1753-1755.

(206) Liberman-Martin, A. L.; Levine, D. S.; Liu, W.; Bergman, R. G.; Tilley, T. D. *Organometallics* **2016**, *35*, 1064-1069.

(207) Chianese, A. R.; Lee, S. J.; Gagné, M. R. *Angew. Chem. Int. Ed.* **2007**, *46*, 4042-4059.

(208) Parson, T. G.; Butikofer, J. L.; Houlis, J. F.; Roddick, D. M. *Organometallics* **2017**, *36*, 136-141.

(209) Vigalok, A. *Acc. Chem. Res.* **2015**, *48*, 238-247.

(210) Clement, M. L.; Grice, K. A.; Luedtke, A. T.; Kaminsky, W.; Goldberg, K. I. *Chem. Eur. J.* **2014**, *20*, 17287-17291.

(211) Fürstner, A. *Chem. Soc. Rev.* **2009**, *38*, 3208-3221.

(212) Hashmi, A. S. K.; Yang, W.; Rominger, F. **2012**, *18*, 6576-6580.

(213) Hashmi, A. S. K.; Schäfer, S.; Bats, J. W.; Frey, W.; Rominger, F. **2008**, *2008*, 4891-4899.

(214) Sen, S. (**2017**) Phosphorus/Antimony and Phosphorus/H-bond Donor Ambiphilic Ligands: Incorporation into Late Transition Metal Complexes and the Reactivity Thereof (Doctoral dissertation). Retrieved from https://oaktrust.library.tamu.edu/

(215) Cussó, O.; Ribas, X.; Lloret-Fillol, J.; Costas, M. *Angew. Chem. Int. Ed.* **2015**, *54*, 2729-2733.

(216) Richers, J.; Heilmann, M.; Drees, M.; Tiefenbacher, K. *Organic Letters* **2016**, *18*, 6472-6475.

(217) Blümel, M.; Hack, D.; Ronkartz, L.; Vermeeren, C.; Enders, D. *Chemical Communications* **2017**, *53*, 3956-3959.

(218) Melaïmi, M.; Gabbaï, F. P. *J. Am. Chem. Soc.* **2005**, *127*, 9680-9681.

(219) Zhao, H. Y.; Gabbaï, F. P. *Nat. Chem.* **2010**, *2*, 984-990.

(220) Kim, Y.; Zhao, H.; Gabbaï, F. P. *Angew. Chem. Int. Ed.* **2009**, *48*, 4957-4960.

(221) Kim, Y.; Hudnall, T. W.; Bouhadir, G.; Bourissou, D.; Gabbaï, F. P. *Chem. Commun.* **2009**, 3729-3731.

(222) Williams, V. C.; Piers, W. E.; Clegg, W.; Elsegood, M. R. J.; Collins, S.; Marder, T. B. *J. Am. Chem. Soc.* **1999**, *121*, 3244-3245.

(223) Lewis, S. P.; Taylor, N. J.; Piers, W. E.; Collins, S. *J. Am. Chem. Soc.* **2003**, *125*, 14686-14687.

(224) Chai, J.; Lewis, S. P.; Collins, S.; Sciarone, T. J. J.; Henderson, L. D.; Chase, P. A.; Irvine, G. J.; Piers, W. E.; Elsegood, M. R. J.; Clegg, W. *Organometallics* **2007**, *26*, 5667-5679.

(225) Koomen, J. A.; Lucas, J. E.; Haneline, M. R.; King, J. D. B.; Gabbaï, F. P.; Russell, D. H. *Int. J. Mass Spectrom.* **2003**, *225*, 225-231.

(226) King, J. B.; Gabbaï, F. P. *Organometallics* **2003**, *22*, 1275-1280.

(227) Tschinkl, M.; Gabbaï, F. P. *J. Chem. Crystallogr.* **2003**, *33*, 595-598.

(228) Fild, M.; Glemser, O.; Christoph, G. *Angew. Chem.* **1964**, *76*, 953-953.

(229) Kiplinger, J. L.; Richmond, T. G. *J. Am. Chem. Soc.* **1996**, *118*, 1805-1806.

(230) Nunn, M.; Sowerby, D. B.; Wesolek, D. M. *J. Organomet. Chem.* **1983**, *251*, C45-C46.

(231) Zhao, X.-F.; Zhang, C. *Synthesis* **2007**, 551-557.